Title
Probabilistic Seismic Hazard Analysis for a Dam Site in Calabria (Southern Italy)

Authors
Zimmaro, Paolo
Stewart, Jonathan P.

Publication Date
2015-10-01

UCLA

Structural & Geotechnical Engineering Laboratory

Probabilistic Seismic Hazard Analysis for a Dam Site in Calabria (Southern Italy)

Paolo Zimmaro, Ph.D.
Jonathan P. Stewart, Ph.D., P.E.
Department of Civil and Environmental Engineering
University of California, Los Angeles

University of California, Los Angeles

Department of Civil & Environmental Engineering

UCLA - SGEL

Report 2015/02

Probabilistic Seismic Hazard Analysis for a Dam Site in Calabria (Southern Italy)

Paolo Zimmaro, Ph.D.
Jonathan P. Stewart, Ph.D., P.E.
Department of Civil and Environmental Engineering
University of California, Los Angeles

UCLA – SGEL Report 2015/02
University of California, Los Angeles
Department of Civil & Environmental Engineering
October 2015

ABSTRACT

Probabilistic seismic hazard analysis (PSHA) are performed for routine applications using source models and ground motion prediction equations (GMPEs) recommended by a government agency (e.g., US Geological Survey) or an expert panel (e.g., SHARE project). For important projects, site-specific PSHA involves critical analysis of GMPEs and sources for the application region. We adopt the latter approach for a dam site in Calabria (southern Italy), a high seismic hazard region. Following SHARE convention, we consider faults sources, background zones, and area sources. We identify several problems with assigned maximum magnitudes in the SHARE model for fault and in-slab subduction sources. We add two sources not present in some prior inventories – the crustal Lakes fault and the Calabrian arc subduction interface. Following procedures developed for the Global Earthquake Model, we select GMPEs that are much better constrained in the hazard-controlling range of magnitudes and distances than those typically used in prior Italian applications. Short-period spectral accelerations at the 2475 year return period exceed those from prior SHARE studies by about 10-15%. Despite the site being located in a region with finite faults capable of generating large events, the 2475-year hazard is dominated by source zones that allow for earthquakes directly beneath the site.

ACKNOWLEDGMENTS

The first author was in part co-financed by the European Commission – European Social Fund and the Calabria region. This funding source is gratefully acknowledged. The views and opinions presented in this author are those of the authors and are not the responsibility of the European Commission or the Calabria region. We thank Laurentiu Danciu and Marco Pagani for useful discussion about the OpenQuake implementation of the SHARE model and Damiano Monelli for the information about the disaggregation outputs. Vincenzo Spina is thanked for his useful input about the Lakes fault implementation.

CONTENTS

LIST OF FIGURES

LIST OF TABLES

1 Introduction

Probabilistic estimates of ground shaking from future earthquakes (i.e., Probabilistic Seismic Hazard Analysis, or PSHA) can be undertaken at three general levels of resolution. The first and most common is to look up ground motion values on maps, such as the USGS seismic hazard maps (Petersen et al., 2014) and maps produced for the Italian building code (MPS working group, 2004; Stucchi et al., 2011). Such maps are based on ground motions computed from PSHA on a grid of points for a reference site condition (typically rock with a time-averaged shear wave velocity in the upper 30 m, VS_{30} = 760 m/s). These maps are most commonly prepared for peak ground acceleration (PGA) and pseudo-response spectral ordinates (PSA) at 0.2 and 1.0 sec oscillator periods. Ground motions computed through this sort of PSHA are not site-specific, because (1) hazard is not computed at the specific site location; (2) geotechnical site conditions are not considered in the hazard analysis, with the ground motions instead being modified with deterministic site factors that do not preserve the desired hazard level (e.g., Goulet and Stewart, 2009); and (3) ground motion intensity measures (IMs) other than mapped values are evaluated from various interpolation functions, not formal hazard analyses.

Site-specific PSHA overcomes these problems, but it too can be undertaken with varying levels of care with respect to local considerations in source and ground motion modelling. The second level of resolution consists of site-specific PSHA using computer programs (commercial or otherwise) with pre-established source models and a library of available ground motion prediction equations. Such source models are typically prepared by groups of experts (e.g., Field et al., 2014; Meletti et al., 2008; Basili et al., 2013), but typically do not include all known faults that might affect a site. The third, and highest, level of resolution in PSHA supplements pre-established source models with consideration of sources in the vicinity of the site. Such analyses may also use ground motion prediction equations (GMPEs) customized for site-specific conditions (non-ergodic) if local characterization of site response or path effects is available

(e.g., Lin et al. 2011; Bommer et al., 2015; GeoPentech, 2015). In this paper, we apply the third type of PSHA for a vital dam in Calabria, Italy. We build upon the SHARE source modeling in the OpenQuake hazard computation platform (Pagani et al., 2014a) by critically evaluating current implementations and supplementing the available fault source models. We review available GMPEs to identify suites that allow for consideration of epistemic uncertainty while capturing local conditions. The GMPEs are applied in an ergodic form due to lack of information on site-specific site and path effects. Results are compared to those obtained using the Italian building code and with application of the generic SHARE model.

Some previous site-specific PSHA studies for sites in Italy have been presented by Sabetta et al. (2005), Pace et al. (2006), Akinci et al. (2009), Faccioli and Villani (2009), Rebez et al. (2014), and Faccioli et al. (2015) for sites in the Apennine mountain range, Po plain or Calabria. The Sabetta et al. (2005) study focused on the sensitivity of hazard results to alternate GMPEs. The remaining studies focused on improving source characterization models by moving beyond areal sources, which have traditionally dominated Italian PSHA (e.g. Stucchi et al., 2011), to increasing use of fault sources of various types or smoothed seismicity. Most of these studies have used either European GMPEs that are now out of date or Italy-specific GMPEs that are poorly constrained at large magnitude (among other problems). Exceptions are Sabetta et al. (2005), which was a GMPE sensitivity study, and Faccioli and Villani (2009), which used global GMPEs.

The present work is differentiated from prior published site-specific PSHAs for Italian sites in four principle respects: (1) we take a relatively global view in the GMPE selection process, with the intent of selecting models that are well constrained over the parameter range of engineering interest, while also capturing region-specific path effects and seeking to have a range of models to approximately capture epistemic uncertainties; (2) we include the Calabrian arc subduction interface as a seismic source, which has not been done previously, as well as a smaller crustal fault source; (3) we consider epistemic uncertainties associated with source characterization and ground motion models, evaluating the relative contributions of each type of uncertainty; and (4) we compare results with hazard computed using more approximate methods and evaluate causes of the differences.

2 Probabilistic Seismic Hazard Analysis: State-of-the-Art in Italy and Europe

The state-of-practice for PSHA in Italy, as implemented in the most recent Italian Building Code, (Norme Tecniche per le Costruzioni, NTC, 2008), was developed between 2003 and 2009, in the framework of a national research projects (2004–2006) funded by the Italian Department for Civil Protection (DPC) and carried out by Istituto Nazionale di Geofisica e Vulcanologia (INGV), (MPS working group, 2004; Stucchi et al., 2011) and it is based on the following features:

- Parametric Catalogue of Italian Earthquakes, CPTI04 developed by a working group of experts since 1999 (Working group CPTI, 1999, 2004);
- Seismogenic zonation (zonazione sismogenetica, ZS ver. 9) ZS9 (Meletti and Valensise, 2004, Meletti et al., 2008), based only on areal sources with equal rate of seismicity (Figure 2.1);
- Ground Motion Prediction Equations (GMPEs) used: Sabetta and Pugliese (1996), based only on Italian earthquakes; Ambraseys et al. (1996), based on European earthquakes; two combinations of regionalized GMPEs derived from Malagnini et al. (2000, 2002), Morasca et al. (2002), De Natale et al. (1988), and Patanè et al. (1994; 1997). Montaldo et al. (2005) provides further details on these regional GMPEs.

The logic tree used for the Italian PSHA is shown in Figure 2.2.

The most recent regional PSHA for the Euro-Mediterranean region is represented by the products released by the Seismic Hazard Harmonization in Europe project (SHARE), in particular the model that is described here is the so called “2013 European Seismic Hazard Model” (ESHM13) (Giardini et al., 2013, Woessner et al., 2015). This model was developed

with a community-based approach (see Danciu et al., 2013) and involved working groups from several countries.

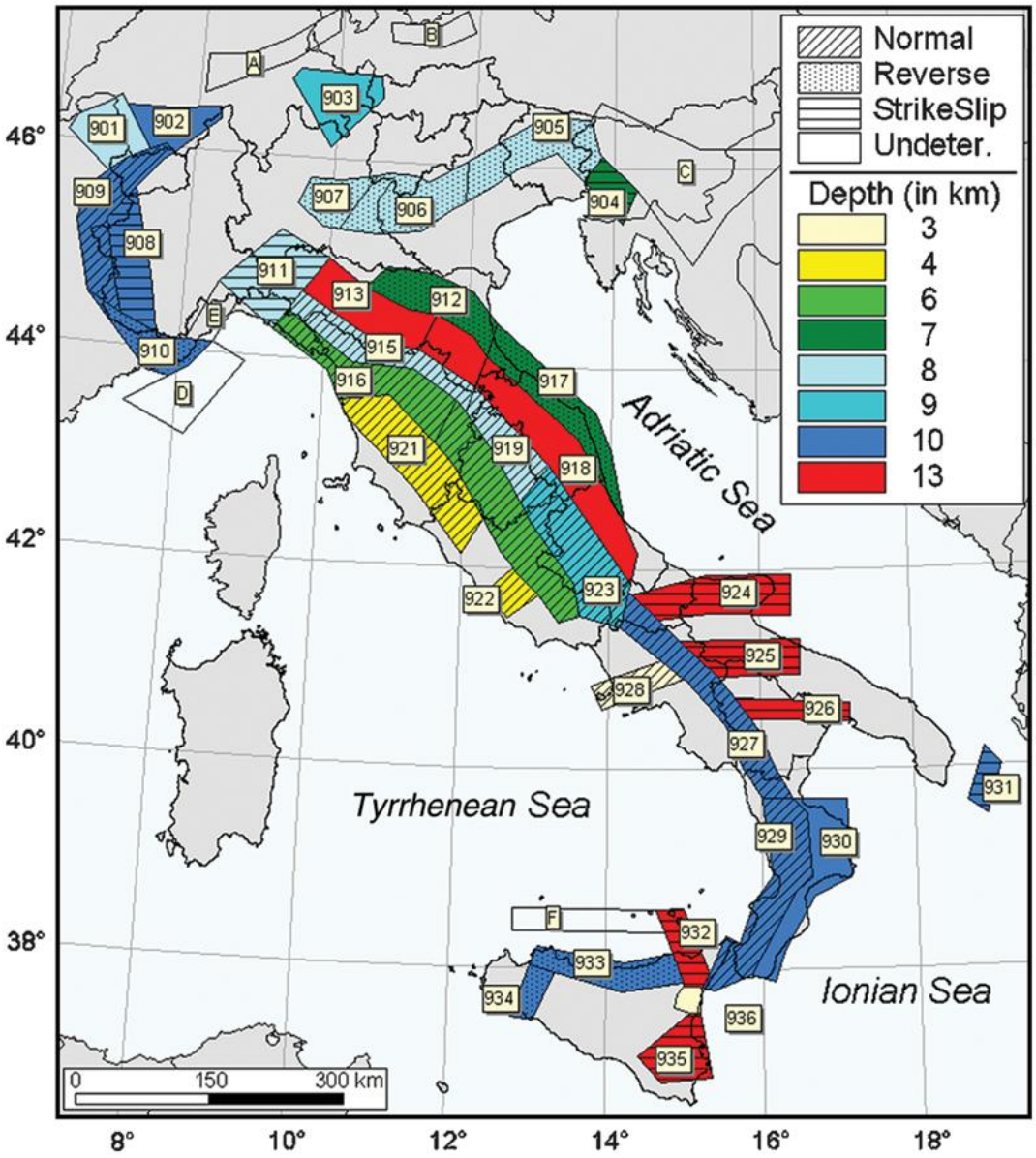

Figure 2.1 **Seismogenic zonation ZS9. The numbers in the boxes identify the earthquake source zones; the colors refer to the mean seismogenic depth (in km); the superimposed shadings refer to the predominant focal mechanism. The source zones with letters were not used in the assessment (from Stucchi et al., 2011).**

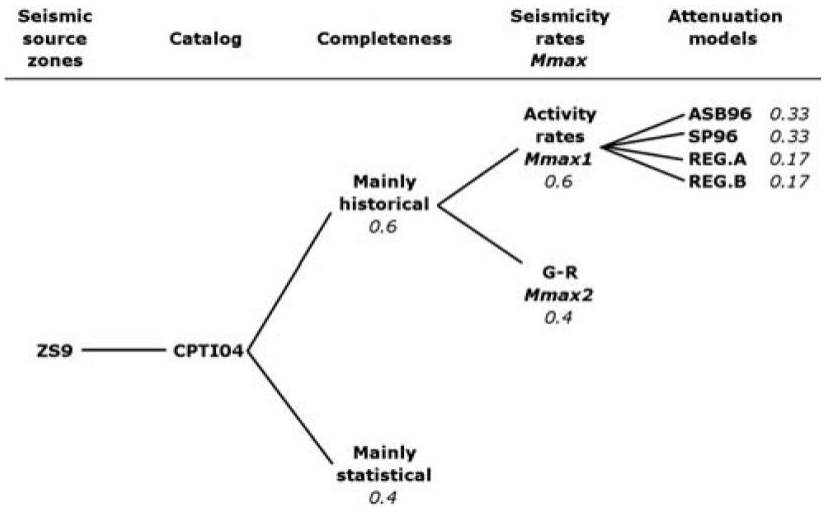

Figure 2.2 Logic tree used in the Italian PSHA (from Stucchi et al., 2011).

The main features of the SHARE model are:

1. Earthquake catalogue SHEEC (1000 – 2006) ver. 3.3 (Stucchi et al., 2012, Grünthal et al., 2013), which is used to define seismic zones (next item);
2. Seismogenic source definition, which is comprised of three branches representing alternate interpretations of the characteristics of future earthquake events so as to capture epistemic uncertainty. The models are listed below:
    a. Area source model (Figure 2.3) for seismic zone 9 - ZS9 (Meletti and Valensise, 2004, Meletti et al., 2008).
    b. Faults Sources + Background model (Figure 2.4): Different distributions of earthquakes are used for different **M** ranges, as shown in Figure 2.5. For **M** > 6.4, earthquakes are assumed to only occur on fault sources (which are defined as identified planar faults, which in some cases represent complex and distributed fault systems; Basili et al., 2008, 2009). The geometric and kinematic parameters that characterize these sources are given in Figure 2.6. For **M** ≤ 6.4, earthquakes are assumed to occur within the background zones shown in Figure 2.4. This fault sources / background model can only be used where fault sources are mapped; where this information is missing this model is not considered .

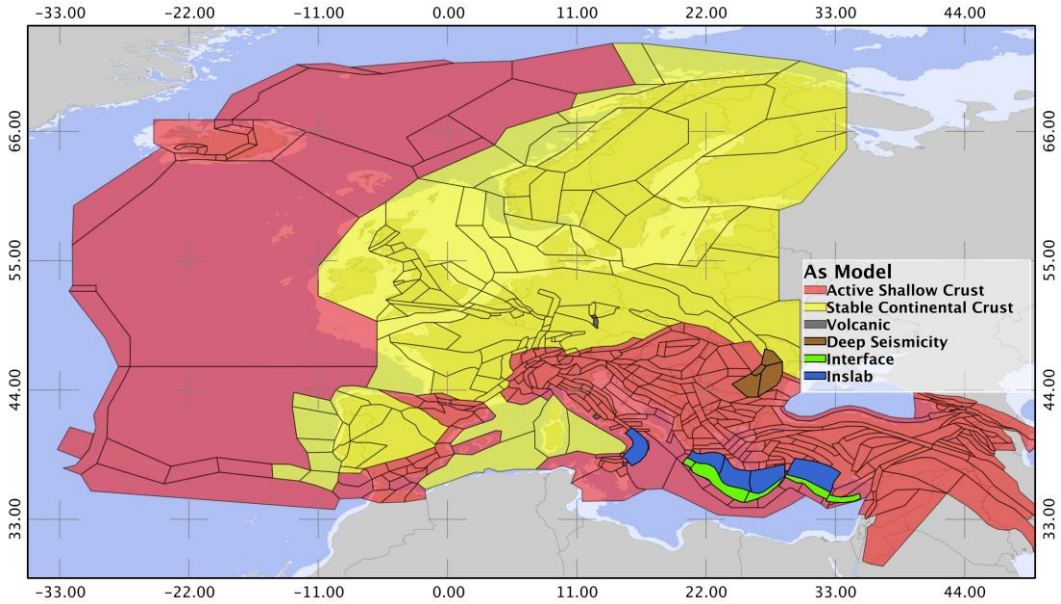

Figure 2.3 **Area sources for the SHARE-Euro-Mediterranean model (from Danciu et al., 2013).**

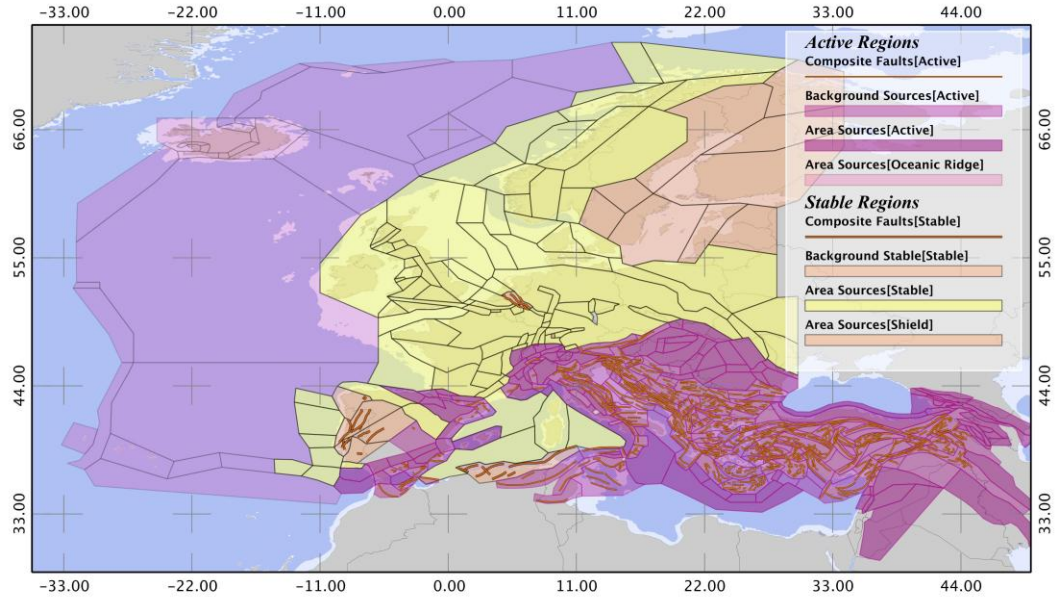

Figure 2.4 **Fault sources + Background zones for the SHARE- Euro-Mediterranean model (from Danciu et al., 2013).**

c. Stochastic earthquake source model (referred to as SEIFA – smoothed SEIsmicity and FAults model): This model is based on the approach of Hiemer et al. (2013, 2014), in which kernel-smoothing methods are applied to smooth earthquake observations in space such that the 'smoothed' catalogue and observed seismicity

have common cumulative distribution functions during the observation period. The approach is applied to estimate future earthquake potential through spatially continuous probability distributions. The SEIFA model applies a kernel-smoothing approach to observed earthquake locations and slip rates on mapped seismic sources (both crustal faults and subduction interfaces). The SEIFA model is based on two probability density maps:

i. One map is obtained by smoothing past seismicity. In this model, there is an estimation of the focal mechanism density obtained by calculating at each point a weighted set of moment tensors, where the weights are proportional to the distances between the observed moment tensors and the point of interest.

ii. A second map is obtained by smoothing fault moment rate contributions. For mapped faults, this map contains the same type of information as the seismicity map. The same smoothing methods are applied by converting the fault sections to point sources having a moment rate and average focal mechanism inferred from the fault section geometry (see also Ward, 2007). The fault sections used in this analysis may be individual segments or combinations of segments. Required information for each section includes its location (latitude and longitude of reference point, length, width, strike, dip), rake, and long-term slip rate. To define the average focal mechanism (moment tensor) for a given source, the strike and dip angle are estimated from the corresponding fault section geometry and the rake angle is taken from the fault database. In this way all faults are simplified to a "catalog" of moment rate point sources that is based purely on fault geometry and slip rates. This catalogue can then be utilized to generate synthetic earthquake catalogues.

The Area source (2a) and Faults Sources + Background (2b) models are referred to as zone-based branches (related to actually mapped sources). The stochastic earthquake source model (2c) is referred to as a Kernel-smoothed branch.

The earthquake source logic tree used in the SHARE model is shown in Figure 2.7.

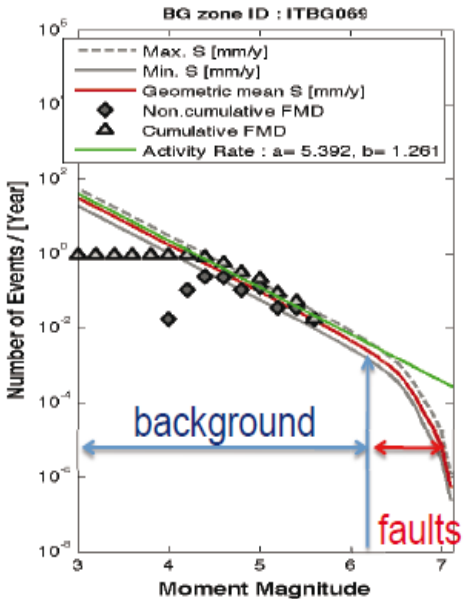

Figure 2.5 Scheme of the different magnitude distributions for the Fault sources + Background model.

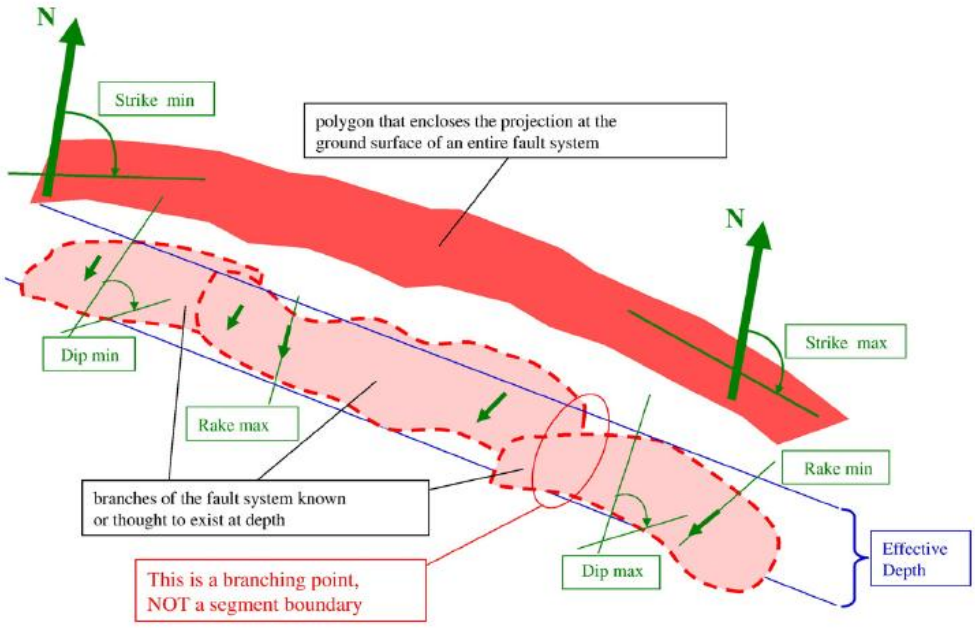

Figure 2.6 Schematic representation of a fault source and its geometric and kinematic characteristics (from Basili et al., 2008).

3. Ground Motion Prediction Equations (GMPEs): Several GMPEs were chosen representing various tectonic regimes in Europe. Figure 2.8 shows the GMPE logic tree with the weight assigned to the different branches (Delavaud et al., 2012). The tectonic

regions present in the European model are: Stable Continental Regions (SCR), Active Shallow Crustal Regions (ASCR), Subduction Zones (SZ), Volcanic zones and Vrancea.

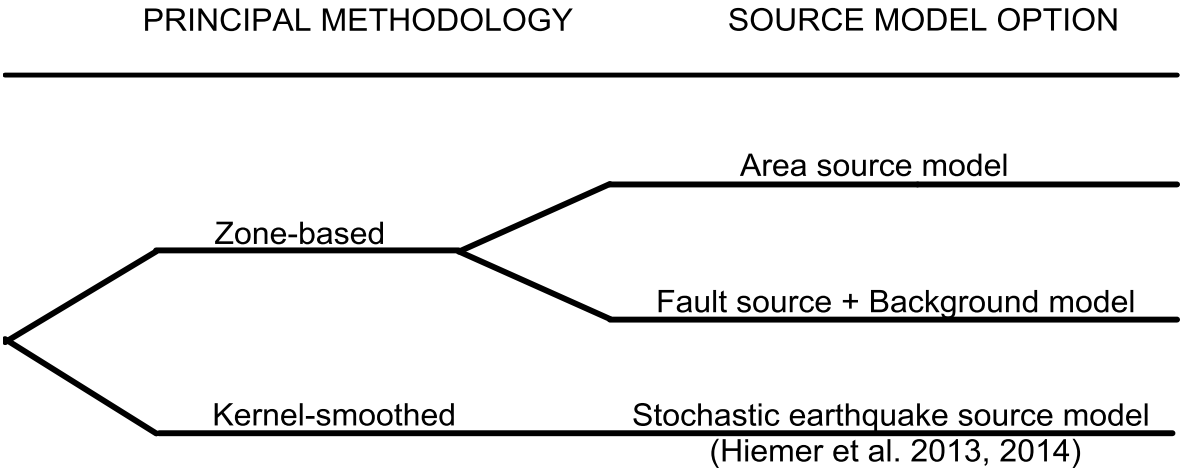

Figure 2.7 Earthquake sources logic tree of the SHARE Euro-Mediterranean model.

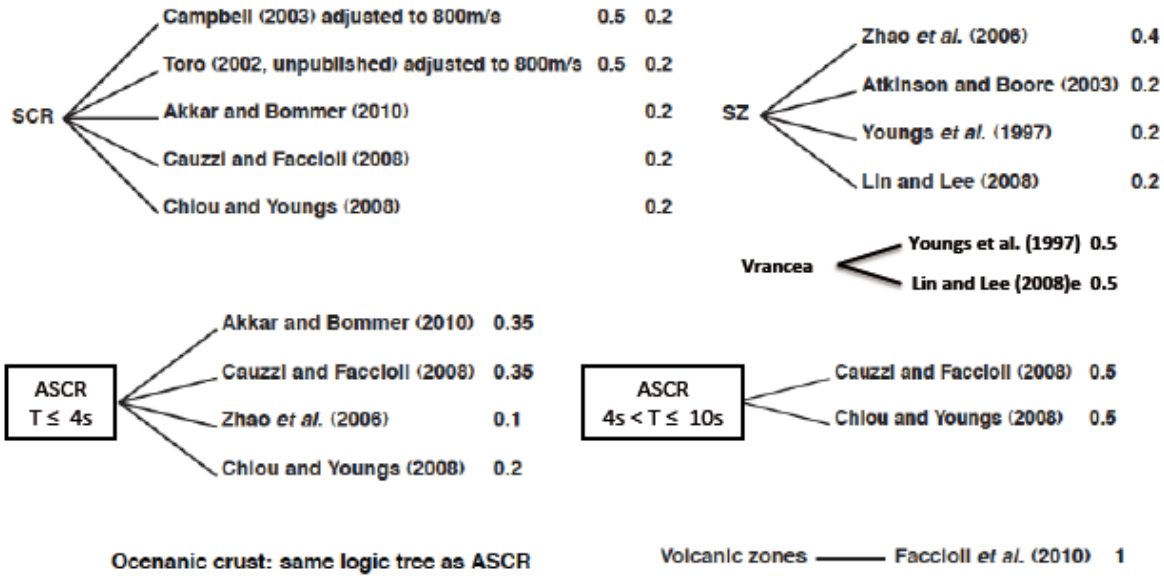

Figure 2.8 GMPE logic tree for the SHARE – Euro-Mediterranean Model (adapted from Woessner, Giardini, and the SHARE consortium, 2012).

3 OpenQuake Engine for Seismic Hazard Analysis

The OpenQuake (OQ) platform (Silva et al., 2014, Pagani et al., 2014a) was selected for performing site-specific PSHA for the dam site. This software was selected because it includes features introduced in the SHARE Euro-Mediterranean project. OQ is an open-source platform that was developed during the Global Earthquake Model (GEM) project. The OQ framework is illustrated in Figure 3.1.

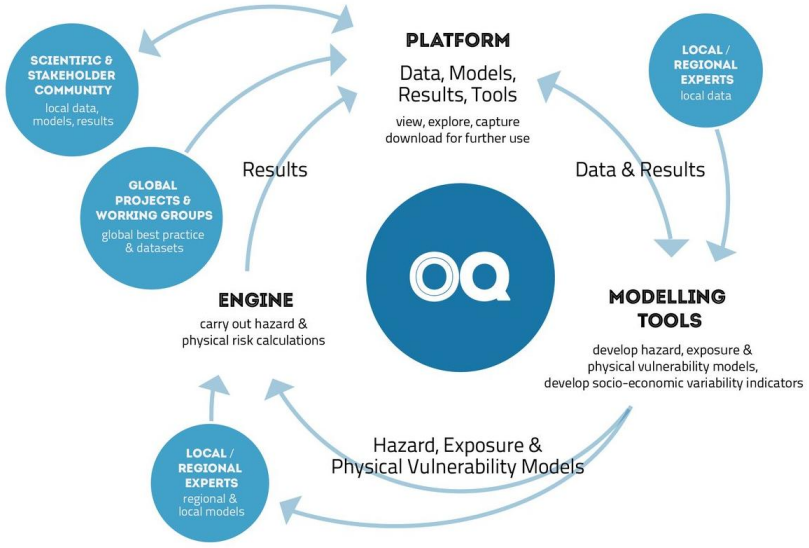

Figure 3.1 The OpenQuake engine project features (from http://www.globalquakemodel.org/openquake, last accessed October 2015).

During its development, the OQ platform was verified for several test cases against computed hazard from other codes included in a Pacific Earthquake Engineering Research (PEER) validation project (Thomas et al., 2010). The satisfactory comparison between the PEER and OQ results for several test cases are presented by Pagani et al. (2014a).

OQ analyses can be executed in the command line of a computer running the software within a Linux operating system, referred to as the 'ubuntu 12.04 LTS distribution'. OQ is comprised of two calculators: the hazard module and the risk module. The two modules are capable of performing several types of analyses. The OQ hazard calculator was used in this study and is described further below. The risk calculator was not used, but is described by Silva et al. (2014).

The hazard module utilizes a python-based library of models for earthquake ruptures, magnitude-frequency distributions, magnitude-area scaling relationships, and GMPEs. This library is accessible through an open web repository.

The library includes the following options for characterizing earthquake sources:

1. Point source: This is the basic source type used to model distributed seismicity. The area sources described below contain point sources. Point sources are not actually points of null dimension. Rather, they represent the centroid of planar ruptures projected onto the ground surface. Hence they can be described solely by a latitude and longitude. Assumptions used to generate rupture planes from a point source are:
    - The shape of the ruptures are rectangular;
    - The hypocenter is located at the centroid of the rupture;
    - The rupture plane is constrained in depth such that it does not extend above the ground surface (which comprises the shallowest possible 'upper seismogenic depth') or below a maximum seismogenic depth (Figure 3.2).

    For a given point source location on the Earth's surface, ruptures can be generated for a range of magnitudes according to the selected magnitude-frequency distribution. The size and shape of the rupture planes are determined using magnitude-area scaling relationships, given a specified aspect ratio (ratio of fault length to width). Ruptures modeled as point sources can have various strike and dip angles for their rupture plane and a range of hypocentral depths between the upper and lower seismogenic depths.
2. Area source: An area source consists of an arbitrary geometric shape at the ground surface having a particular magnitude-recurrence relationship. They are defined based on seismicity patterns and are commonly employed when fault locations are unknown. Earthquakes within area sources are taken as point sources (Item 1 above) distributed

randomly within the area. A depth component is added to area sources by assuming a distribution of hypocentral depths that is derived from the earthquake catalogue (in SHARE model, this is simplified to a single value of hypocentral depth taken as the average from the earthquake catalogue). Area sources are the most frequently adopted source type for European national and regional PSHA. In the SHARE Euro-Mediterranean model, both crustal seismogenic zones and subduction intra-slab zones are modeled using area sources.

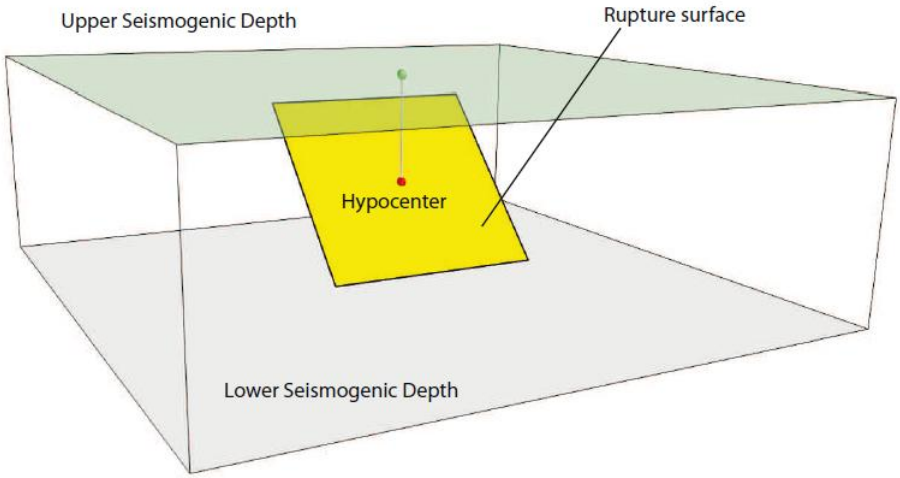

Figure 3.2 Single rupture in a point source (from Butler et al., 2014).

3. Simple fault source: This source type is used for shallow seismogenic faults (referred to in §2 as Type 2b – 'Fault sources + Background zones' in the SHARE Euro-Mediterranean model). Simple fault sources are defined geometrically by means of the fault trace, which is the vertical projection of the shallowest portion of the fault to the ground surface. This fault trace can have multiple linear segments, the locations of which are given by a series of geodetic coordinates (latitudes and longitudes). The 3D fault surface is defined from the fault trace combined with fault dip, upper and lower seismogenic depth, and rake angle (using the convention of Aki and Richards, 2002). Accordingly, the fault surface consists of series of connected rectangles. Earthquake locations are simulated using a floating rupture source approach whereby hypocenters can occur anywhere on any segment. The earthquake magnitude follows a specified

magnitude-frequency distribution. The rupture area follows magnitude-area scaling relations and any user-specified aspect ratio can be used.

4. Complex fault source: This source type is used for subduction interfaces and shallow crustal sources having complex geometry. The geometry of complex faults is defined by two fault edges (at the top and bottom the fault surface). Each edge is defined by a series of points with specified geodetic coordinates (latitude, longitude) and depth; dip is not specified but is constrained by the edges. The fault surface itself can be taken as planar or curved between the edges. The floating rupture process is the same as for simple fault sources.

5. Characteristic fault source: In this source, the rupture always occupies the entire fault area. It is used for faults or fault segments that are believed to produce characteristic earthquakes of comparable size (Schwartz and Coppersmith, 1984). The characteristic earthquake is typically implemented for a fault in a hybrid manner whereby smaller **M** earthquakes are characterized using a truncated exponential model. No faults are modelled using the characteristic model in SHARE nor in the present study.

The occurrence of earthquakes on these source types is assumed to be uniformly distributed in space (within area sources or along faults) and to occur in time according to a Poisson process.

The OQ hazard module performs classical PSHA, Monte-Carlo event-based PSHA (Musson, 2000), disaggregation (Bazzurro and Cornell, 1999), and scenario-based deterministic seismic analysis. The classical PSHA produces hazard curves, Uniform Hazard Spectra (UHS) and hazard maps using the procedure of Field et al. (2003). Calculations of this type were used in this study and for the SHARE Euro-Mediterranean PSHA modeling.

OQ has functionality to allow implementation, debugging, and testing of new GMPEs. This was used in the present work to implement an NGA-West 2 model for application in Italy. OQ also has functionality to allow for user-specified logic trees to address epistemic uncertainties. The main disadvantage of the current release of the software is its non user-friendly interface (command-line driven) and the inconvenience of only being supported by Linux platforms.

4 Source Models for Farneto del Principe Dam Site

The Farneto del Principe dam site is in the Calabria region, southern Italy. As shown in Figure 4.1, the site-specific PSHA for the subject site was performed in OQ using the area sources model (AS model; Type 2a in §2) and the 'fault sources and background zones' model (FSBG model, 2b). These source types comprise two branches in the logic tree having equal weight. The kernel-based SEIFA model (2c) was not used; the rationale for this choice is that the kernel-based smoothing approach is conceptually alike to 2a and 2b when source locations are reasonably well established, as is the case in the region of the subject site. Hence, adding a third branch for model type 2c does not capture additional epistemic uncertainty (sensitivity studies presented in §6.4 show that including a SEIFA branch in the logic tree does not affect hazard ordinates). Accordingly, the additional computational cost for adding kernel-based model in this study was judged to not be worthwhile.

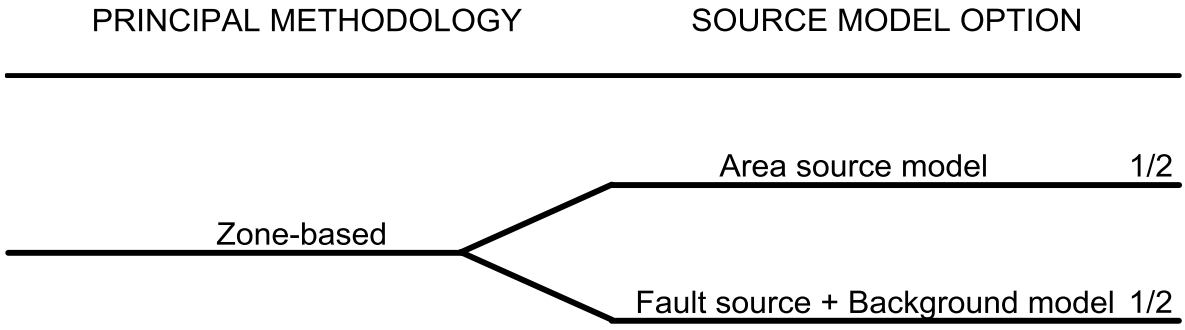

Figure 4.1 Sources logic tree and weights used in this study.

The following sections present details of the two source models types. In this study, only sources with distances ≤ 250 km to the subject site are considered.

4.1 The Area Sources Model (AS Model)

The area source model for the present study is taken from seismogenic zone 9 (ZS9) from Meletti and Valensise (2004) and Meletti et al. (2008); with the parameters adopted in the SHARE Model (Giardini et al., 2013). Earthquakes are assumed to follow a truncated exponential distribution between a minimum magnitude of $\mathbf{M}_{min}$=4.6 (minimum possible magnitude of the distribution) and a maximum magnitude ($\mathbf{M}_{max}$) that is varied as described further below. The *b* value sets the likelihood of earthquakes of different **M** whereas the cumulative *a* value (where 10^a = annual number of earthquake with **M** > 0) sets the earthquake rate in time.

Maximum magnitude ($\mathbf{M}_{max}$) defines the largest earthquake in a given zone and is unknown. $\mathbf{M}_{max}$ is estimated from the largest observed earthquake, with some arbitrary judgement-based adjustment, or from the largest event that could be anticipated given the dimensions of known fault sources in the zone ($\mathbf{M}_{obs}$). If the historic earthquake catalogues extend back substantially longer in time than the return period of $\mathbf{M}_{max}$, then $\mathbf{M}_{obs}$ is a good estimate of $\mathbf{M}_{max}$. Even though the Italian catalogue goes back in time to A.D. 1000 (CPTI04 catalogue by Working Group CPTI, 2004), and is considered sufficiently well sampled so as to be 'complete' since 1450 (Woessner et al., 2012), this observation period is too short to be confident that $\mathbf{M}_{obs}$ is a safe estimate of $\mathbf{M}_{max}$. Accordingly, following SHARE convention, our approach considers four estimates of $\mathbf{M}_{max}$, with decreasing weights, as follows:

- $\mathbf{M}_{obs}$ (weight = 0.5);
- $\mathbf{M}_{obs}$ + 0.2 (weight = 0.2);
- $\mathbf{M}_{obs}$ + 0.4 (weight = 0.2);
- $\mathbf{M}_{obs}$ + 0.6 (weight = 0.1).

The resulting magnitude-frequency distribution of each area source, is characterized by a rapidly descending earthquake rate occurs between ($\mathbf{M}_{obs}$) and ($\mathbf{M}_{obs}$+0.6). Values of parameters *a* and *b* for each area source are estimated from the historical and recorded seismicity using the SHEEC catalogue (ver. 3.3). In that catalogue, attempts are made to decluster aftershocks from mainshocks and the parameters are based on mainshock data. The same *b* value is used for all

source types, whereas *a* values are selected in consideration of the relative number of normal, reverse and strike-slip earthquakes located within the source zone.

As shown in Figure 4.2, eleven area sources are located within 250 km of the site and are included in this analysis. Each area source has three identification numbers (IDs) corresponding to normal, reverse, and strike-slip mechanisms. Hence, 33 areas source IDs are tracked in the analysis. Source parameters $\mathbf{M}_{obs}$, *a*, and *b* are given for each source zone in Table 4.1. The subject site is located in area source 319, which has $\mathbf{M}_{obs}$ = 7.8 (Giardini et al., 2013).

Given the source parameters of Table 4.1, the moment rate release ($\dot{M}_0$) within each area source can be calculated as:

$$\dot{M}_0 = \lambda_m \int_{m_{min}}^{m_{max}} f(m) \cdot M_0(m) dm \tag{4.1}$$

where λ_m is the Poisson rate of occurrence of earthquakes with $m > m_{min}$, m_{min} and m_{max} are the minimum and maximum magnitude, respectively, *f(m)* is the probability density function of the magnitude distribution, and M_0 is the seismic moment. M_0 can be related to the moment magnitude by using the well-known relation of Hanks and Kanamori (1979), given as:

$$M_0 = 10^{1.5\mathbf{M}+16.05} \tag{4.2}$$

As previously discussed, area sources are modeled following a truncated G-R distribution with $\mathbf{M}_{min}$=4.6. Using alternative values of maximum magnitude: (1) $\mathbf{M}_{obs}$, and (2) $\mathbf{M}_{obs}$+0.6, we calculate two rates of moment release ($\dot{M}_0^1$, and $\dot{M}_0^2$ respectively) for the whole study area of southern Italy. The resulting values, are practically identical. As a result of the $\mathbf{M}_{max}$ modeling approach used in this study, the rate of moment release is dominated by earthquakes with $\mathbf{M} \leq \mathbf{M}_{obs}$.

4.2 The Fault Sources and Background Zones Model (FSBG Model)

As shown in Figure 4.3, the fault sources and background zones model (FSBG model) for the subject region is a hybrid of fault sources as well as background zones and area sources. The fault sources are either individual or composite seismogenic sources from Basili et al. (2008, 2009). Fault sources are represented by known ‘simple’ or ‘complex’ faults (defined in §3, list

items 3 and 4). Figure 4.4 shows the shallow crustal fault sources considered in the present analysis, including the Crati Valley fault (source 015) that is the closest fault source to the site (details in §4.3) and the Lakes fault that is newly implemented here as a simple fault in OQ (§4.4). Not shown in Figure 4.4 is the fault at the subduction interface, which is introduced in the present work and discussed in §4.5.

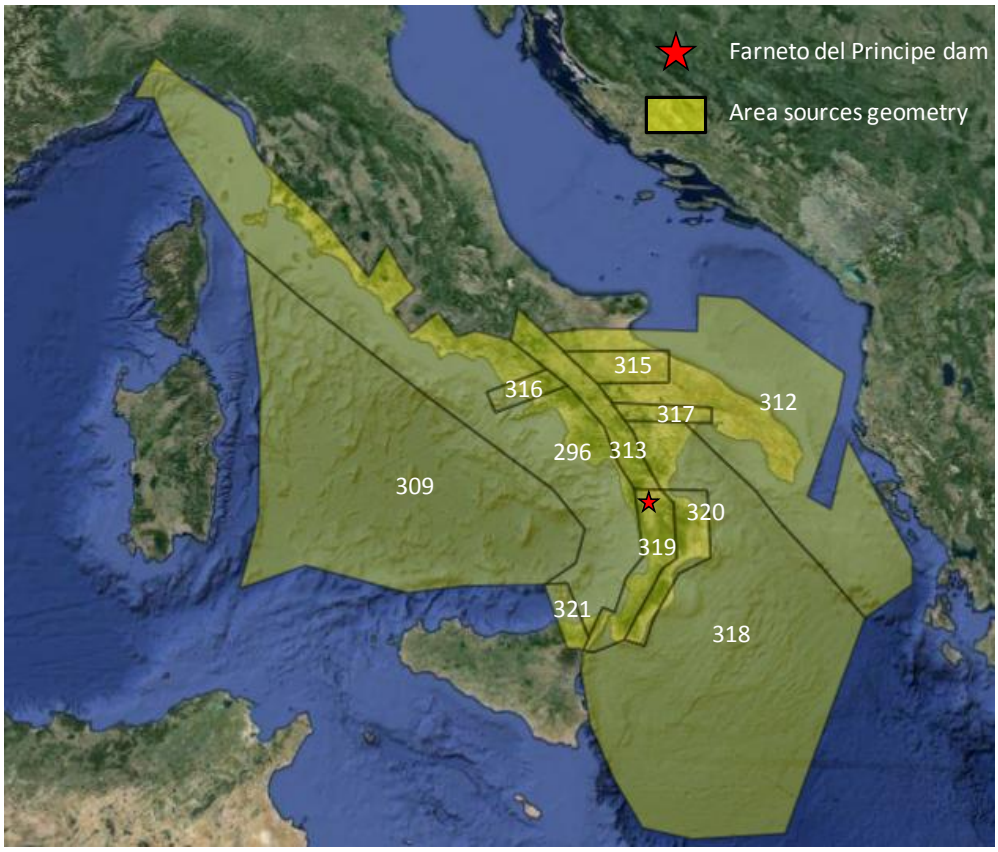

Figure 4.2 **The Area sources used in the PSHA with the correspondent source identification numbers.**

Table 4.1 **Summary of the parameters used for the implementation of the AS model. The first ID # for each source applies to normal fault mechanisms, the second to reverse, and the third to strike-slip.**

Source	ID	a_{inc}^{*}	*b value*	M_{obs}
296	291	3.0688	-1	6.6
	292	3.2449		
	293	3.4667		
309	264	2.8443	-1	6.6
	265	2.6682		
	266	3.0661		

(continued on next page)

Table 4.1 (cont.) **Summary of the parameters used for the implementation of the AS model. The first ID # for each source applies to normal fault mechanisms, the second to reverse, and the third to strike-slip.**

Source	ID	a_{inc}^{*}	*b value*	$\mathbf{M_{obs}}$
312	330	3.2118	-1	6.6
	331	2.8438		
	332	3.3667		
313	333	3.0877	-0.9	7.8
	334	3.4235		
	335	2.3096		
315	339	3.0442	-1	7.8
	340	3.38		
	341	2.2661		
316	342	2.4677	-1	6.6
	343	3.3128		
	344	2.7688		
317	345	2.8442	-1	7.8
	346	3.18		
	347	2.0661		
318	348	3.2112	-1	8.0
	349	2.8432		
	350	3.3661		
319	351	3.0877	-0.9	7.8
	352	3.4235		
	353	2.3096		
320	354	3.2442	-1	7.8
	355	3.58		
	356	2.4661		
321	357	3.5964	-1.1	7.8
	358	3.9322		
	359	2.8182		

*Incremental *a* values, defined such that the annual rate of earthquakes within the magnitude range of $\mathbf{M}\pm\Delta\mathbf{M}/2$ is $10\text{^}(a_{inc}\text{-}b\mathbf{M})$. $\Delta\mathbf{M} = 0.2$ is the magnitude bin width.

Area sources are included in the FSBG model for regions without mapped faults. For these regions, the source characterization in the FSBG branch is identical to that in the AS model as defined in §4.1. They are included here so that the FSBG branch is complete with respect to the

geographic distribution of sources (i.e., if area sources were not included, large portions of Italy, especially off-shore areas, would appear as aseismic in this branch).

Figure 4.5 shows area sources and background zones. Background zones are a special type of area source containing faults. Area sources do not align perfectly with background zones at the edges; thus, the edges of area sources were adjusted to fit the background zones as needed in accordance with SHARE documentation (http://www.efehr.org:8080/jetspeed/portal/hazard.psml last accessed October, 2015).

As described in §2, $\mathbf{M} \geq 6.4$ earthquakes are assumed to occur on finite faults and smaller events in background zones. SHARE recommendations were followed (Woessner et al., 2012) in which the maximum magnitude ($\mathbf{M}_{max}$) is assigned to finite faults as follows:

1. Aspect Ratio (AR) is calculated from fault length and width (L and W, respectively):

$$AR = {}^{L}/_{W} \tag{4.3}$$

2. The applied Aspect Ratio (AR^*) is constrained below a limit of 3:

$$AR^* = \begin{Bmatrix} AR & if\ AR < 3 \\ 3 & if\ AR \geq 3 \end{Bmatrix} \tag{4.4}$$

3. An effective length (L_{eff}) is derived from AR^*:

$$L_{eff} = W \cdot AR^* \tag{4.5}$$

4. The effective area (A_{eff}) is calculated as:

$$A_{eff} = W \cdot L_{eff} \tag{4.6}$$

   It should be noted here that the use of A_{eff} as derived from Eq. (4.6) will be smaller than the actual fault area whenever the actual fault aspect ratio $AR > 3$. This represents a flaw in the SHARE recommendations for extended faults.

5. Using L_{eff}, W and A_{eff}, $\mathbf{M}_{max}$ was evaluated as the mean of four magnitude-area scaling equations recommended by the SHARE Euro-Mediterranean model (Wells and Coppersmith, 1994, Kagan, 2002, Leonard, 2010, Hanks and Bakun, 2002, 2008). These estimates of $\mathbf{M}_{max}$ will be under-predicted for sources with $AR > 3$ due to the use of an artificially low fault area A_{eff} in Step (4). The impact of this problem with the SHARE recommendations will be investigated in future research.

Uncertainty in $\mathbf{M}_{max}$ for fault sources is not considered in the main logic tree for this study.. Instead, $\mathbf{M}_{max}$ uncertainty is considered separately in sensitivity analyses presented in §6.4.

Earthquake rates for faults and background zones in the FSBG model are set in consideration of balancing moment build-up and release. Moment build-up ($\dot{M}_0$) for a fault is computed as:

$$\dot{M}_0 = \mu \cdot s \cdot A_{eff} \tag{4.7}$$

where μ is fault friction, A_{eff} is effective fault area, and s is slip rate. Moment release is the product of earthquake rate and the weighted average moment for earthquakes on the fault, which is sensitive to the probability density function on **M** (and hence to b and $\mathbf{M}_{max}$). By balancing moment building up and release, the rate of earthquakes can be computed, which is directly related to the a value (Anderson and Luco, 1983). This approach was implemented by Bungum (2007) and used in the SHARE model (as documented at: http://www.efehr.org:8080/jetspeed/portal/hazard.psml, last accessed October, 2015). Moment build-up computed using Eq. (4.7) is subject to under-prediction error for extended faults as discussed previously due to the use of A_{eff}.

The parameters used for the implementation of the fault sources and background zones are summarized in Tables 4.2 and 4.3, respectively. The area sources used in this model have the same characteristic and parameters as the sources used in the AS-model.

4.3 Characterization of the Crati Valley Fault

Fault source 015 in Table 4.2 and Figure 4.4, which is the Crati Valley fault, is the most proximate finite fault source for the dam site. Accordingly, a special attention was directed to the characterization of this source to verify the accuracy of its parameterization for hazard analysis.

As shown in Figure 4.6(a) the Crati Basin is located on the Tyrrhenian side of northern Calabria. It is a tectonic depression (graben) developed between the coastal range and the Sila Massif. The Crati Basin is oriented north-south (N-S) and is bounded by two approximately N-S striking normal fault systems. The western normal fault dips to the east and the eastern normal fault dips to the west. This graben-fault system has been the subject of recent research and the tectonic evolution and activity of the system is still debated (Van Dijk et al., 2000; Monaco and Tortorici, 2000; Tansi et al., 2005, 2007; Spina et al., 2009, 2011; Brozzetti et al., 2012).

Spina et al. (2009) show that the west side of the Crati fault system is comprised of three east-dipping en-echelon faults (Montalto Uffugo–Rende Fault, MRF; S. Marco Argentano–S. Fili

Fault ,MMF; Fagnano Fault, FF). They also show that the eastern border is considerably more complex, with a series of west-dipping normal faults as shown in Figure 4.6(b). The Crati Basin extension is related to fault slip rates and dip angles, which have been evaluated in prior work as described further below. As shown in Figure 4.7(a), the northern and southern limits of the Crati fault system is well constrained by the roughly east-west striking Pollino fault (PFZ) on the north side and the Falconara-Cosenza fault zone (FCFZ) to the south. Spina et al. (2011), reconstruct the tectonic evolution of the Crati Basin, showing that the geometry and the extension of the system are consistent with the fault model implemented in the SHARE Euro-Mediterranean PSHA in which the more active side of the graben is to the east.

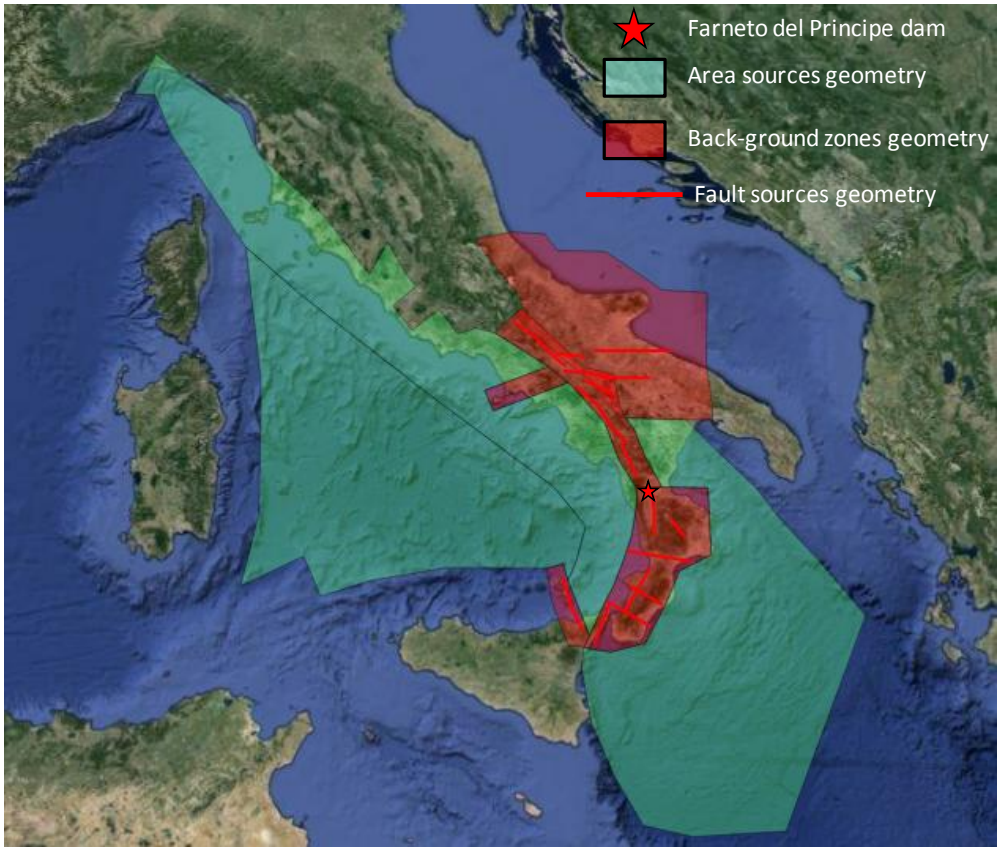

Figure 4.3 Overview of the complete FSBG model.

The relatively high activity on the eastern margin of Crati Valley is further supported by geological and geomorphological observations of drainage pattern, deformation of the top of the metamorphic substratum (along with the overlying Pleistocene units) and radon anomalies (e.g: Carobene and Damiani, 1985; Molin et al., 2004; Tansi et al., 2005) as synthesized in DISS 3.1.1 web commentary (http://diss.rm.ingv.it/dissHTML/ITCS015TXT.html, last accessed October

2015). While the fault on the western edge of the graben is well expressed geologically and morphologically, there is no evidence of Holocene activity. As shown in Figure 4.6 and 4.7(b), historic and instrumental seismic activity is present along both lineaments, but is more pervasive on the east side (Tansi et al., 2005; Spina et al., 2009, 2011).

Figure 4.4 Fault sources (finite faults) used in this study.

Based on this evidence, we model only the eastern side of The Crati Valley as having a seismogenic source that is defined between upper and lower seismogenic depths of 1 and 10 km, respectively. The faults on the western border are considered inactive in the FSBG model. The eastern side of the Crati valley is modeled as a simple fault in this study. Its geometry and the parameters characterizing magnitude distribution and earthquake rate match those used in the SHARE model (given in Table 4.2).

4.4 Implementation of the Lakes Fault

The Lakes fault is shown in Figure 4.4 and its fault parameters are listed in Table 4.2. This fault is not included among the seismogenic sources included in the SHARE model (Giardini et al.,

2013). We identified this fault through review of recent literature presenting the results of paleoseismic analysis (Galli and Bosi, 2003; Galli et al., 2004, 2007; Spina et al., 2004; 2006, 2007). As shown in Figure 4.4, the Lakes fault is located on the north-eastern side of the Calabria region approximately 60 km from the dam site. Due to its close proximity, we implemented the Lakes fault as a finite fault source.

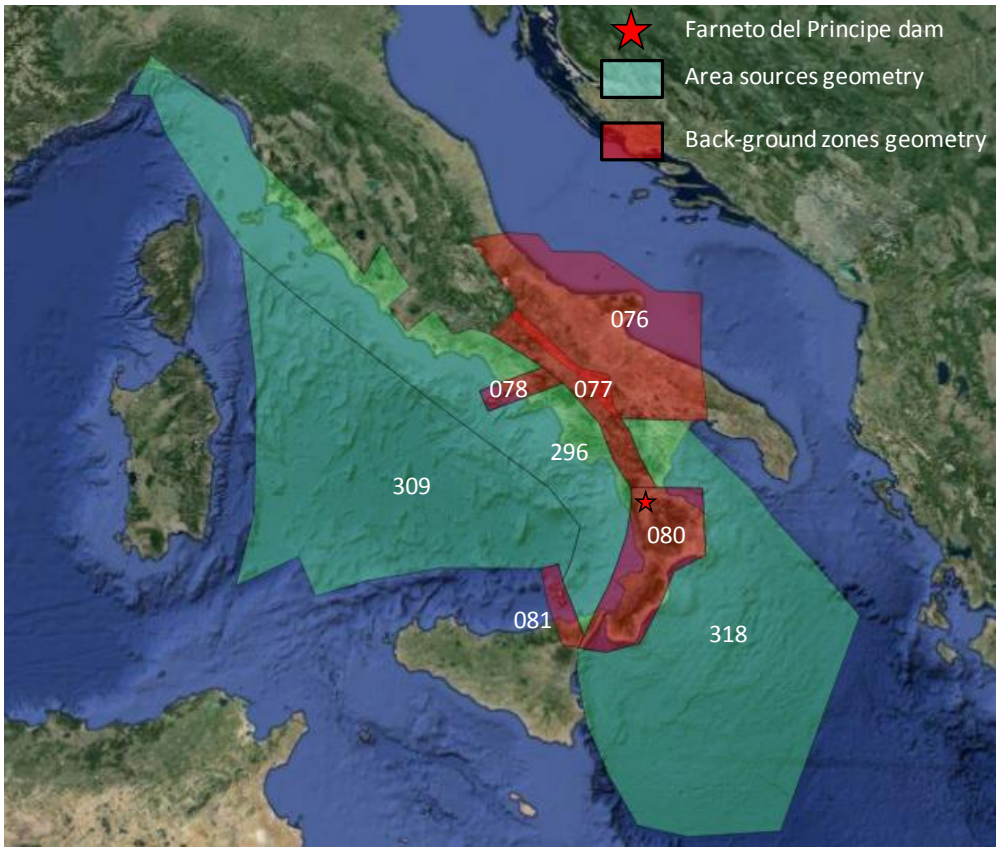

Figure 4.5 **Background zones and area sources used in the FSBG model for this study.**

Table 4.2 **Summary of the parameters used for the implementation of the FSBG model**

Source ID	*a value*	*b value*	M_{max}
042	4.26205	1.218	7.6
016	2.20777	0.793	7.2
055	0.97664	0.793	6.8
082	1.60513	0.793	6.8
080	1.04329	0.793	6.8
053	1.62688	0.793	7

(continued on next page)

Table 4.2 (cont.) **Summary of the parameters used for the implementation of the FSBG model**

Source ID	*a value*	*b value*	M_{max}
068	1.14016	0.793	7
015	1.3673	0.793	6.8
038	1.21588	0.739	7
034	1.18182	0.739	7.2
063	2.02179	0.844	7.2
089	1.47429	0.844	7
084	2.00385	0.844	7.2
004	1.40067	0.844	7
024	1.23063	0.739	7.2
Lakes*	1.815	0.793	6.7

*For more information about the parameters used for the implementation of the Lakes fault, see §4.4

Table 4.3 **Summary of the parameters used for the implementation of the background zones in the FSBG model**

Source	ID	a_{inc}*	*b value*	M_{max}
076	961	2.4849	0.844	6.4
	962	1.7067	0.844	
	963	2.8207	0.844	
077	964	1.7909	0.739	6.4
	965	1.0128	0.739	
	966	2.1267	0.739	
078	967	1.9532	0.977	6.4
	968	2.7983	0.977	
	969	2.2543	0.977	
080	970	1.5865	0.793	6.4
	971	1.7226	0.793	
	972	1.9844	0.793	
081	973	3.4582	1.218	6.4
	974	3.6343	1.218	
	975	3.8561	1.218	

* Incremental *a* values, defined such that the annual rate of earthquakes within the magnitude range of $\mathbf{M}\pm\Delta\mathbf{M}/2$ is $10^{(a_{inc}-b\mathbf{M})}$. $\Delta\mathbf{M} = 0.2$ is the magnitude bin width.

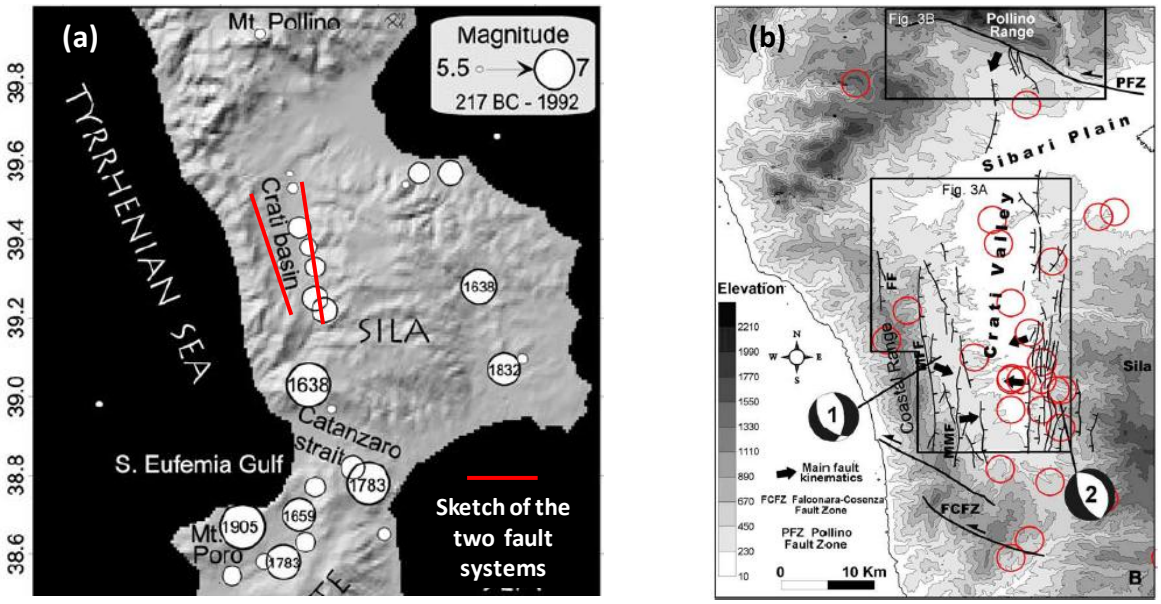

Figure 4.6 **(a) Shaded relief view of the area of interest with the sketches of the two fault systems (Crati Basin) and the historical events with magnitude 5.5 from 217 B.C. to 1992. The first known event occurred in 91 B.C., the last reported is 1978 (Working Group CPTI [1999] source, adapted from Galli and Bosi, 2002); (b) Seismicity distribution in the Crati Basin. Black arrows show mean kinematic vectors along faults (from Spina et al., 2009).**

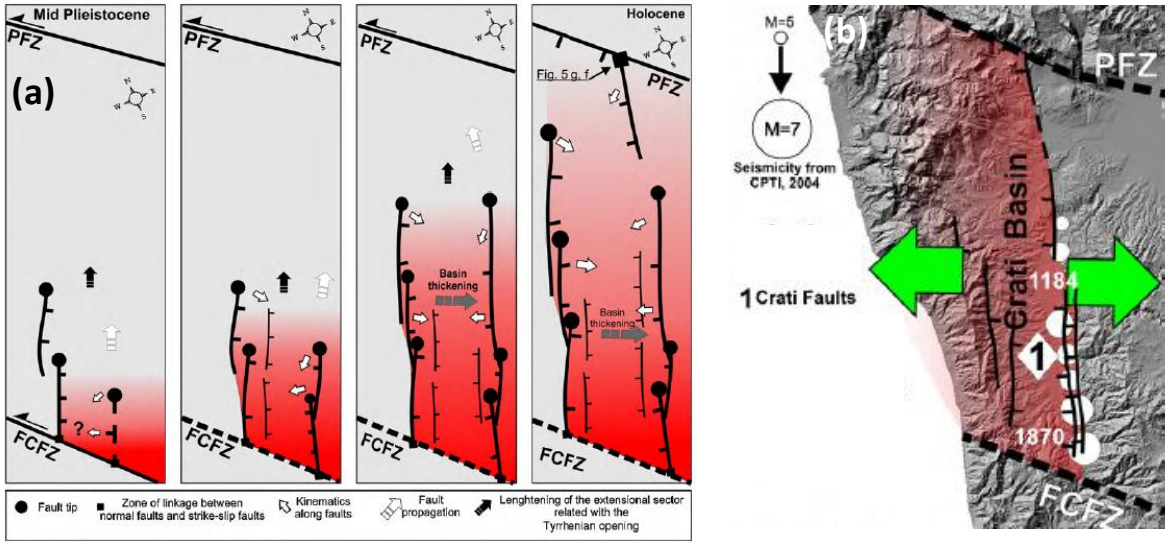

Figure 4.7 **(a) Time-space propagation of extension within the Crati Basin from Middle Pleistocene to Holocene times (from Spina et al., 2010). (b) View of northern Calabria showing rough distribution of macroseismic areas for M> 5earthquakes (from Basili et al., 2009), Spina et al. (2011)**

Galli and Bosi (2003) analyzed primary historical sources of the catastrophic March–June 1638 Calabrian earthquakes and conducted paleoseismic analyses along the Lakes fault

alignment (the fault was unknown prior to their work). They opened four trenches and found five late-Holocene surface faulting events, the last one being compatible with the June 9 1638 earthquake. These analyses motivated a shift of the June 1638 epicenter as shown in Figure 4.8. They interpret the mechanism as an oblique normal fault. Galli et al. (2007) opened a fifth trench to correlate fine alluvial units across the fault, in particular organic and/or charred material suitable for absolute dating. The surface faulting events identified by Galli and Bosi (2003) and Galli et al. (2007) are dated: 21st century BC, 12th century BC, 3rd century BC, between the 6th and 7th century AD (after 645–691 A.D. and before 798–893 A.D.), and June 1638 (average time between events of 900 years). Spina et al. (2007) performed structural analyses using a geo-statistical approach to characterize the geometric, dimensional and kinematic characteristics of the Lakes Fault. They found that the Lakes fault is comprised of two main right stepping segments arranged *en-echelon* that behave as a unique structure, because are linked through relay zones made up of minor faults (hard linkage). They also showed that the rake is mainly strike-slip for most of the fault length.

We model the Lakes Fault as a 33 km long, left lateral (strike-slip), SW dipping feature. The maximum magnitude assigned to the fault is $\mathbf{M}_{max}$=6.7 based on the average obtained from three magnitude-area scaling relationships: Leonard (2010), Hanks and Bakun (2002, 2008) and Wells and Coppersmith (1994). The width and the area used are W=15 km and A_{eff}=495 km respectively (note that the fault aspect ratio of ~2 is less than three, so the fault area bias noted in §4.2 it not present in this case). The $\mathbf{M}_{max}$ assigned to the Lakes fault, calculated using these magnitude area scaling relationships, is consistent with the maximum magnitude historically observed on the fault. We take the dip and rake as 60° and 150°, respectively. The Gutenberg-Richter b value is taken as 0.793 based on historical seismicity data for the background zone in which the Lakes fault is located. The a value was computed as 2.4 via moment balance using a slip rate, estimated by Galli and Bosi (2003), of s = 1.2 mm/yr, the aforementioned fault dimensions, and a truncated exponential PDF for magnitude.

4.5 The Calabrian Arc Subduction Zone

The Calabrian arc subduction zone accommodates subduction of the Ionian oceanic segment of the African plate beneath the Tyrrhenian continental segment of the Eurasian plate. Figure 4.9

shows the extent of the seismogenic portion of the subduction interface and in-slab region. The dam site falls within the surface projection of these source regions, indicating that subduction sources may be a significant cause of activity affecting the hazard.

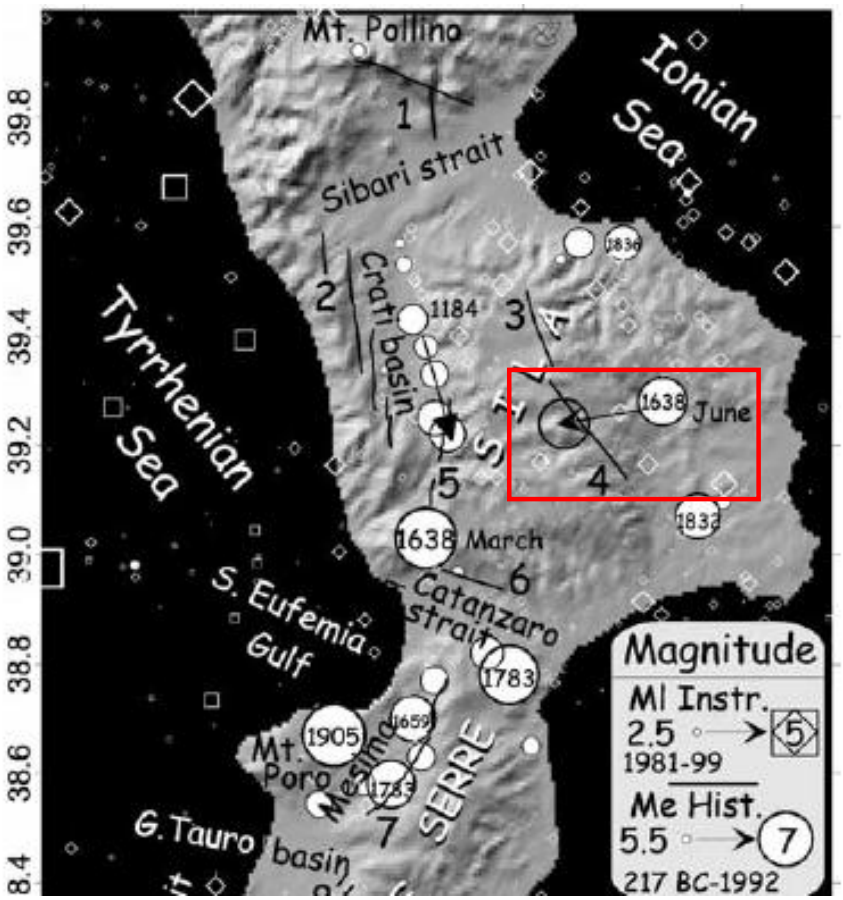

Figure 4.8 **The Lakes fault (in the red rectangle), #4 in figure and the shift of the June 1638 earthquake epicenter after paleoseismic analyses (adapted from Galli and Bosi, 2003).**

Three types of earthquakes occur in this region:

1. In-slab earthquakes, which occur in the region marked in Figure 4.9. These are considered in the SHARE Euro-Mediterranean model using one area source polygon (shown in Figure 4.9) with five associated depths and three focal mechanisms (33% for normal, 33% for strike-slip, and 34% for thrust/reverse). The incremental *a* values used across the 15 sources are 2.33 for 10 normal and strike-slip sources and 2.34 for five thrust/reverse sources, based on seismicity from deep earthquakes. A constant *b* = 0.9 was used for all sources.

2. Interface earthquakes, which occur between the lines marking the upper and lower seismogenic depths in Figure 4.9. This source of earthquakes is not considered in the SHARE model.

3. Shallow crustal earthquakes, which are modelled using a combination of area and fault/background sources as described earlier.

We adopt the SHARE model for in-slab and shallow crustal activity (with addition of Lakes fault as described in §4.4). We add an interface model using a complex fault source (this source type is defined in §3). We consider geodetic observations to constrain interface activity and derive a maximum magnitude of 8.2 from a recent magnitude-area scaling relation proposed for subduction zones (Strasser et al., 2010). Uncertainty in $\mathbf{M}_{max}$ is taken into account such that the largest considered value is about 8.6 (about 1.7 standard deviations above the mean; details in §6.4.3). The complex fault interface source, as modelled in OQ, is shown in Figure 4.9. Depths to the interface top and bottom are 10 km and 60 km, respectively.

In the remainder of this section, we describe further the geology of the subduction zone, geodetic and seismic constraints used in support of the fault model, and the process used to parameterize the fault model.

Figure 4.10 shows plan and profile views of the geologic structure of the Calabrian arc subduction zone (Van Dijk et al., 2000), which is the last remaining oceanic crust subduction in the region (de Voogd et al., 1992; Faccenna et al., 2001, 2004; D'Agostino et al., 2008). The tectonic structure constitutes the forearc belt of the active subduction of the Ionian basin. Figure 4.11 indicates that the subducting slab consists of a narrow Wadati-Benioff zone (Anderson and Jackson, 1987; Giardini and Velonà, 1991; Selvaggi and Chiarabba, 1995; Chiarabba et al., 2005) dipping toward the northwest at about 70° (Pepe et al., 2010). An active volcanic arc is present at the location of the Aeolian Islands as shown in Figure 4.11. The Calabrian arc accretionary wedge developed due to the SE-NW Africa/Eurasia convergence, presently occurring at a very slow rate, as reported by recent GPS studies (Calais et al., 2003; Reilinger et al., 2006; Serpelloni et al., 2007; D'Agostino et al., 2008; Devoti et al., 2008). Laterally, the seismically active portion of the slab is not longer than 250 km, less than its down-dip width, resulting in one of the smallest seismically active in-slab sources in the world (Chiarabba et al., 2005).

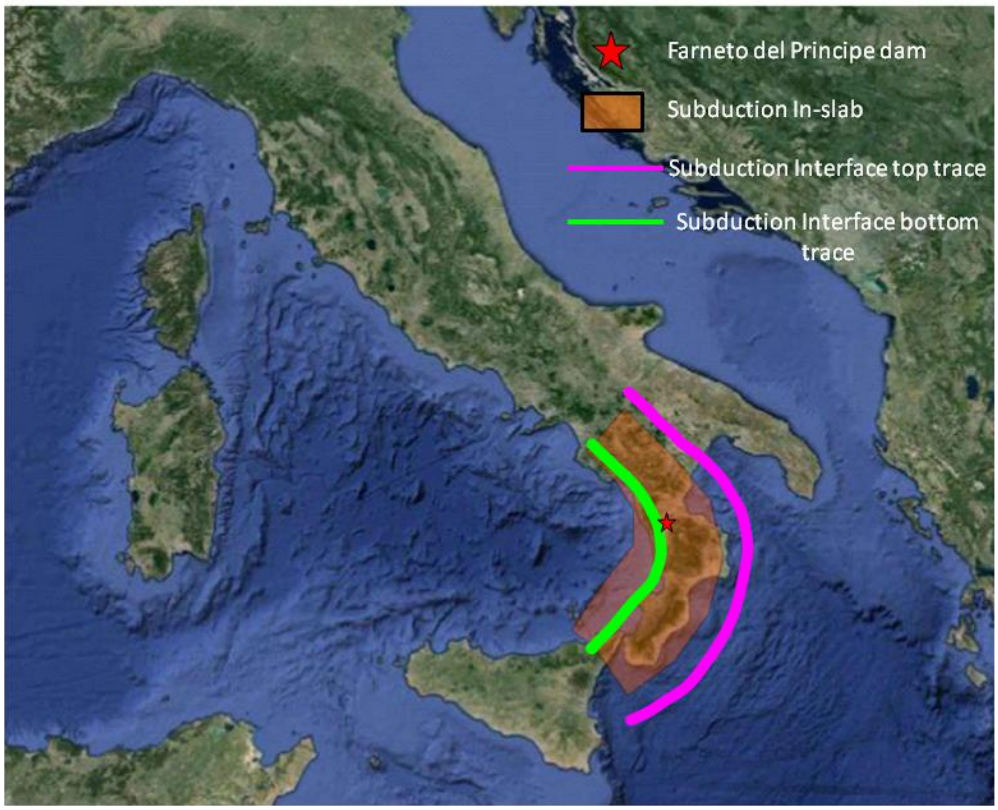

Figure 4.9 Geometry of the subduction in-slab and interface as implemented in this study.

Geodetic observations using GPS data have been interpreted to gain insight into the subduction mechanism including the rate of convergence between the Ionian oceanic crust and the Calabrian continental curst. The GPS data are widely spaced and as such are most suitable for macro-scale analyses. As a result, there is a large uncertainty associated with the subduction zone convergence rate and the spatial distribution of relative displacements. In this regard, Slejko et al. (2010) state:

> *"(1) the knowledge of the seismogenic faults in Italy is incomplete in terms of the number of faults and their geometric and seismic characteristics and (2) constraints from geodetic data are problematic because the number of permanent global positioning satellite (GPS) stations in Italy is small, the fact that they have only been in operation a short time interval (about 5 years), and the campaign measurements provide velocities with a large associated uncertainty.".*

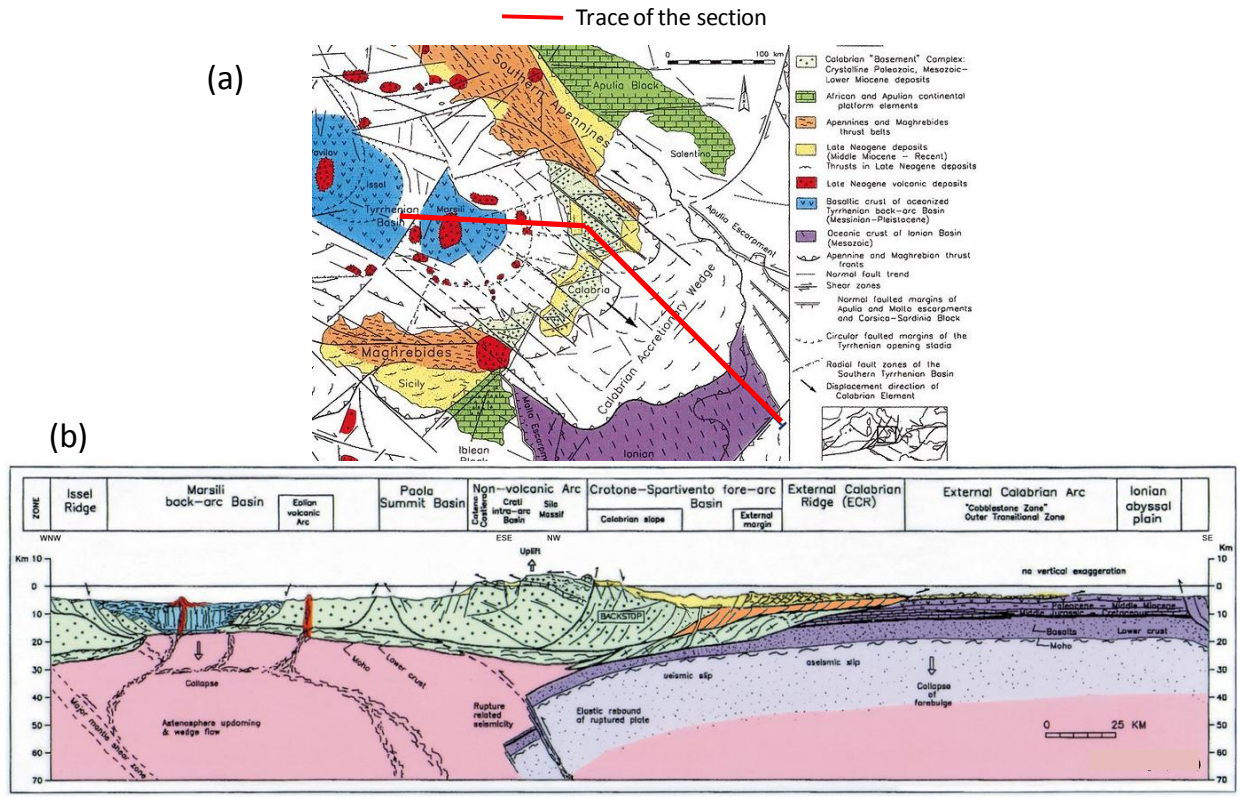

Figure 4.10 **(a) Geological framework of the Central Mediterranean region; (b) Crustal section of the Central Mediterranean region (from Van Dijk et al., 2000).**

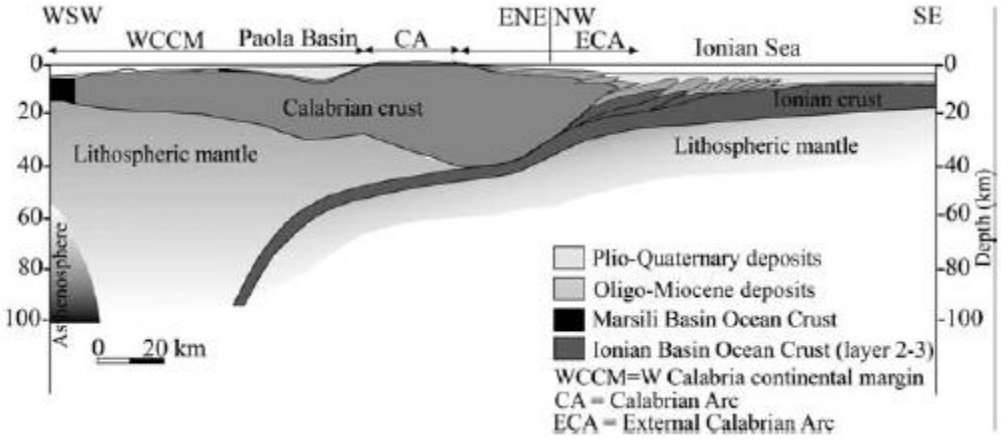

Figure 4.11 **Cross section from the Marsili ocean crust (southern Tyrrhenian) to the Ionian foreland displaying the lithospheric setting of the "Ionian Subduction zone" (from Pepe et al., 2010).**

Slejko et al. (2010) interpreted geodetic strain rate across the Italian territory from GPS-based horizontal velocities discretized into four large circular domains defined by radii of 100 to 300 km (Figure 4.12). This approach was adapted from similar work in California (Ward, 2007). The geodetic strain rate was then converted to seismic moment rate ($\dot{M}_0$). This conversion is sensitive

to crustal thickness, which was taken as 10 km by Slejko et al. (2010) due to a relative paucity of hypocenters below that depth. Due to the shallow depth, this approach does not allow for the possibility of subduction-related seismicity (in-slab and interface).

Slejko et al. (2010) also present a finite element model of the Italian crust to estimate the rate of moment release (considering only characteristic earthquakes) on sources very similar to those in the SHARE model. The two sets of moment rates (build-up from GPS observations and release from FEM analysis) have a large misfit, with the release being an order of magnitude smaller. Slejko et al. (2010) explain this result as follows:

> *"This discrepancy is motivated by the fact that the (moment rate) in each domain from GPS observations is given by the sum of the (moment rates) released as characteristic earthquakes plus that released as distributed seismicity and as aseismic creep, while the (moment rate) from geophysical modelling refers only to the contribution of the characteristic earthquakes."*

We speculate that another reason for the discrepancy could be the omission of a large source, which in the Calabria region could be the subduction zone.

Mattei et al. (2007) used GPS data to investigate the evolution of the Calabrian arc. They find that the GPS data do not facilitate the analysis of a reliable strain field. They also suggest that the convergence rates required to explain crustal movements in the early Pleistocene are not present today, indicating that a slow-down may be occurring. Figure 4.13 shows that Calabria together with the southern Apennines and Apulia, has an independent motion with respect to both Nubia (5 mm/yr to ESE) and Eurasia (3 mm/yr to NNE), as well as a distinct motion relative to Sicily, with a tectonic boundary between Sicily and Calabria presently located in the Messina Straits area. The possible role of subduction in the accommodation of these differential motions is not discussed.

Angelica et al. (2013) describe the presence of deep seismicity due to the Calabrian arc subduction zone as follows:

> *"Italian seismicity (http://csi.rm.ingv.it/) can be considered as superficial, since the hypocenters are concentrated at depths of less than 50 km except*

in the area beneath the Calabrian arc, and is affected also by a deeper seismicity that reveals the presence of a subduction zone along a NW-dipping Benioff plane (Chiarabba et al., 2005).”

As shown in Figure 4.14(a), Angelica et al. (2013) compile GPS velocities for the Italian territory, which are combined with seismicity to estimate strain rates as shown in Figure 4.14(b). However, they do not describe how the subduction zone accommodates observed strain rates.

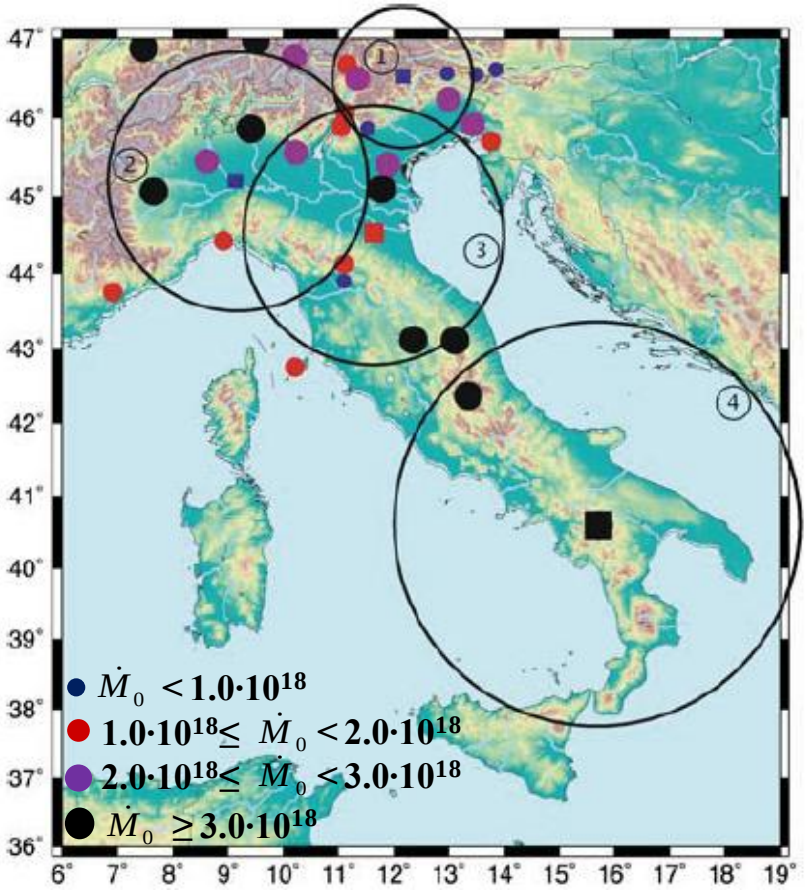

Figure 4.12 **$\dot{M}_0$ (in N·m/year) computed from GPS observations. The central GPS station of each domain is marked by a square with size and color according to its $\dot{M}_0$. The numbered large circles identify the four domains: 1 eastern Alps, 2 western Alps, 3 central Apennines, 4 southern Apennines (adapted from Slejko et al., 2010).**

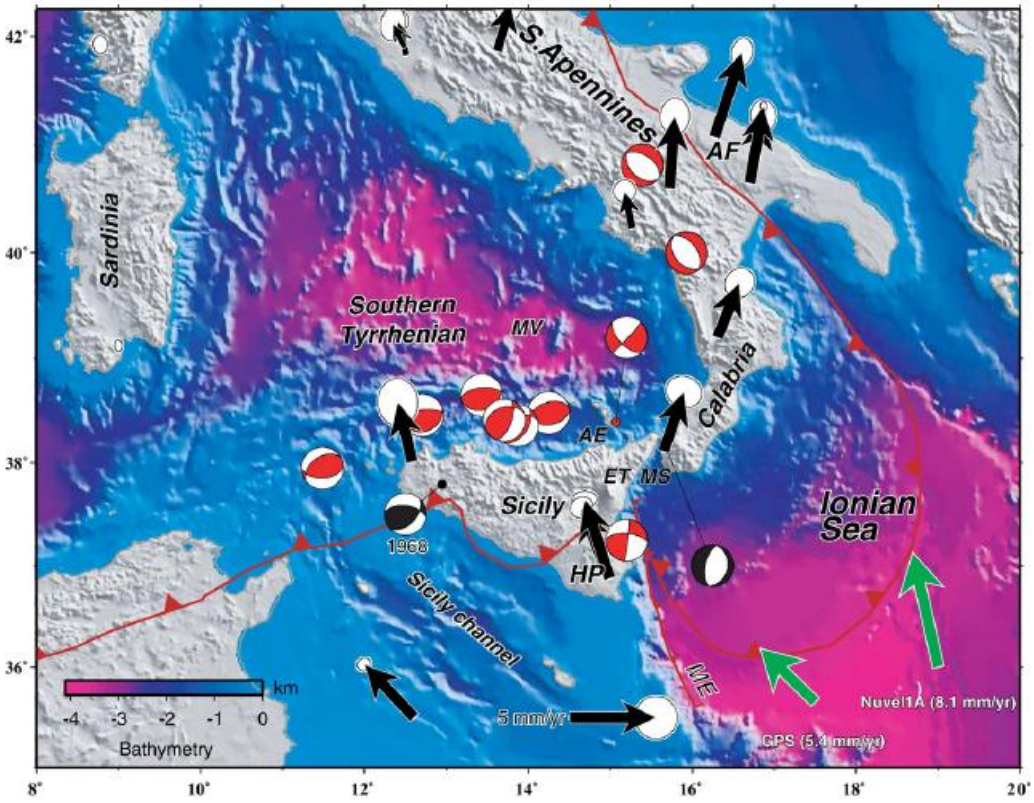

Figure 4.13 **Regional map of southern Italy including present-day Eurasia-fixed velocity field and seismicity of the Calabrian Arc (modified from D'Agostino and Selvaggi, 2004). Crustal focal mechanisms are selected from the CMT Catalog (M>5, in red) and from Anderson and Jackson (1987) in black. Green arrows show the predicted convergence between Nubia and Eurasia according to the Nuvel-1A model and the GPS-derived pole of rotation (from Mattei et al., 2007).**

While the aforementioned geodetic studies provide tantalizing evidence for the significance of the subduction boundary, none interpret the GPS data so as to estimate the convergence rate at the plate boundary. Such an inference is provided by D'Agostino et al. (2011), who state:

> "*we propose that the reference frame appropriate to evaluate the motion of the CA relative to the lower plate should be attached to those parts of the foreland most probably attached to the Ionian lithosphere, i.e. the Apulian block. The Apulia-fix GPS velocity field (Figure 4.15) shows a southeastward migration of the CA in agreement with the shortening directions observed in the most recently deformed part of the Ionian wedge [Gutscher et al., 2006; Minelli and Faccenna, 2010]. These findings strongly suggest that the CA is migrating relative to Ionian*

lithosphere and approximately 2 mm/yr of convergence is absorbed in the Ionian wedge."

The manner by which this convergence is accommodated within the crust is uncertain:

"More obscure is the style of deformation and seismogenic potential in the Ionian wedge. The limited extent of the GPS network limits the resolution capability to detect locking of the subduction interface, especially if the coupled zone extends principally offshore."

Mastrolembo Ventura (2012) also evaluated the convergence rate from GPS data and sought to understand how it is accommodated by deforming tectonic structures in the region using an elastic block model. She provides two hypotheses for convergence rates – 2-3 mm/yr and 5-6 mm/yr, which are somewhat higher than those of D'Agostino et al. (2011). Those alternate rates are coupled with alternate crustal deformation hypotheses. Figure 4.16 shows the scheme of the tectonic blocks in the area that were considered. Figures 4.17 and 4.18 illustrate two mechanisms associated with the two convergence rates. In summarizing these results, Mastrolembo Ventura (2012) states:

"Importantly, the convergence rates across the Ionian-Calabrian subduction interface differ by a factor of two depending on which plate the Ionian oceanic lithosphere belongs to. The SE-ward displacements of the Calabrian stations with respect to the Ionian block occur at rates of 5 mm/yr and 2.5 mm/yr with respect to Nubia or to the Ionian-Apulian plate, respectively (see figs. 4.17 and 4.18). Therefore, it is of fundamental importance for the evaluation of the seismic potential of the Calabrian region to understand how this convergence is eventually accommodated along the subduction interface, and if its deformation signal may be overprinted on the measured velocity gradient across the Messina Straits. An Ionian-fixed velocity field is the appropriate reference frame realization for our objective, allowing us to implement a relatively simple block geometry while accounting for the two end-member kinematic boundary conditions along the Ionian-Calabria plate contact. This is realized by implementing two different experiments (figs. 4.17 and 4.18),

the first one considering the Ionian block as part of Nubia (i.e., using Nubia-fixed velocities), and the second one considering the Ionian block as part of the Apulian microplate (i.e., using Apulia-fixed velocities).”

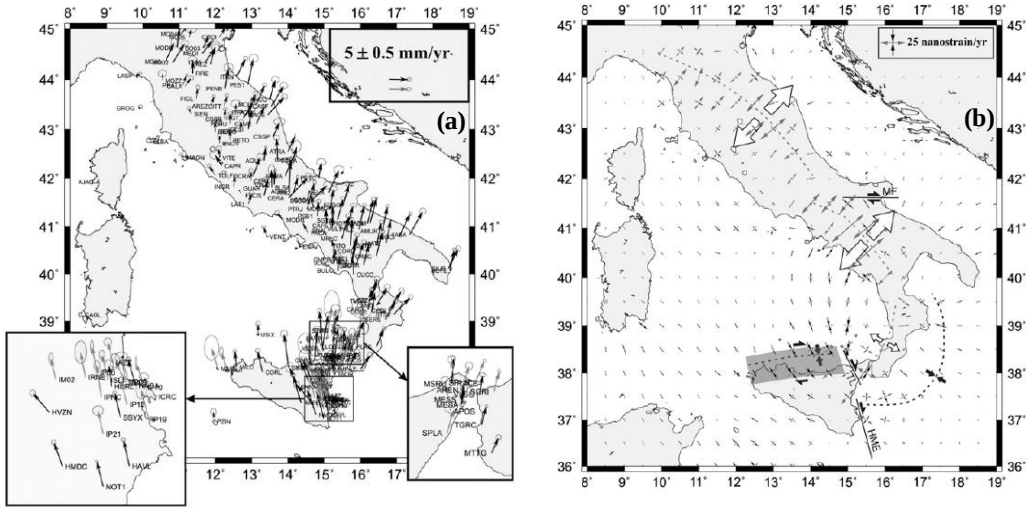

Figure 4.14 **(a) GPS velocities and associated error ellipses for the entire Italy. Black arrows for permanent stations; gray arrows for surveys; (b) Combined final strain rates resulting from joint inversion of GPS and seismic data. White arrows across dashed gray lines indicate the main extension areas; solid lines stand for strike-slip faults in the significant shear strain zones; dashed black line with converging black arrows indicates the compression front of the chain in the Ionian sea; the gray shadowed area indicates a transpressive regime affecting the northern off-shore of Sicily. (adapted from Angelica et al., 2013).**

In summary, we have three estimates of convergence rate across the Calabrian subduction zones: 2.5 mm/yr (D’Agostino et al., 2011), 2-3 mm/yr and 5-6 mm/yr (Mastrolembo Ventura, 2012). We consider the defensible range of convergence rates to be 2 to 6 mm/yr. This convergence should be accommodated within the subduction zone by in-slab and interface earthquakes. As mentioned previously, we adopt the SHARE model characterization of in-slab earthquakes. We characterize interface moment release using alternate slip rates of 2-6 mm/year. The moment release rate ($\dot{M}_0$) associated with the 2-6 mm/yr slip rate range is 0.76 to 2.2 $\times$ 10^{25} dyne-cm/yr, using an assumed *b* value of 0.9 (inferred from regional deep seismicity). Corresponding *a* values are 3.8 to 4.3. These rates are considerably higher than the moment release rate for the in-slab earthquakes of 0.39 dyne-cm/yr, which corresponds to an *a* value of 3.7. The sensitivity of the hazard results to the range of interface slip rates is presented in §6.4.3.

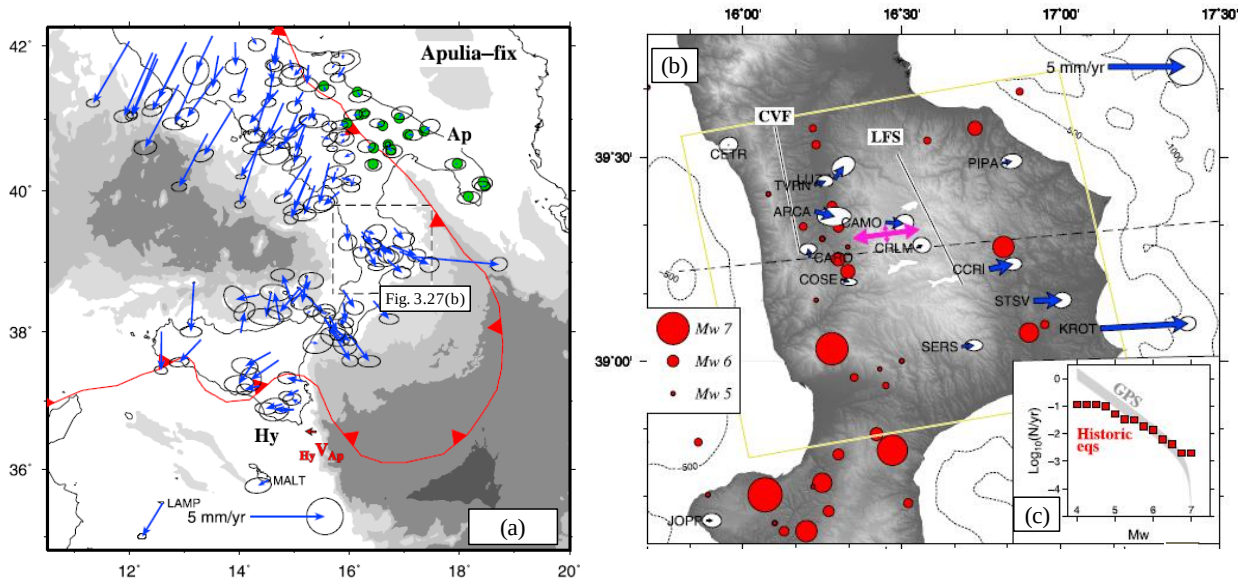

Figure 4.15 **(a) GPS velocity fields in the Apulian reference frame. The sites used to determine the relative Eulerian vector are marked with green circles. The red arrow shows the motion of the Hyblean region relative to Apulia; (b) Zoom of the GPS velocities in Northern Calabria, red circles are M > 5 earthquakes from the CPTI04 catalogue in the interval 1500 A.D. to the present. CVF, Crati Valley Fault System; LFS, Lakes Fault System. (c) Cumulative magnitude-frequencies of CPTI04 seismicity from 1500 A.D. to the present (adapted from D'Agostino et al., 2011).**

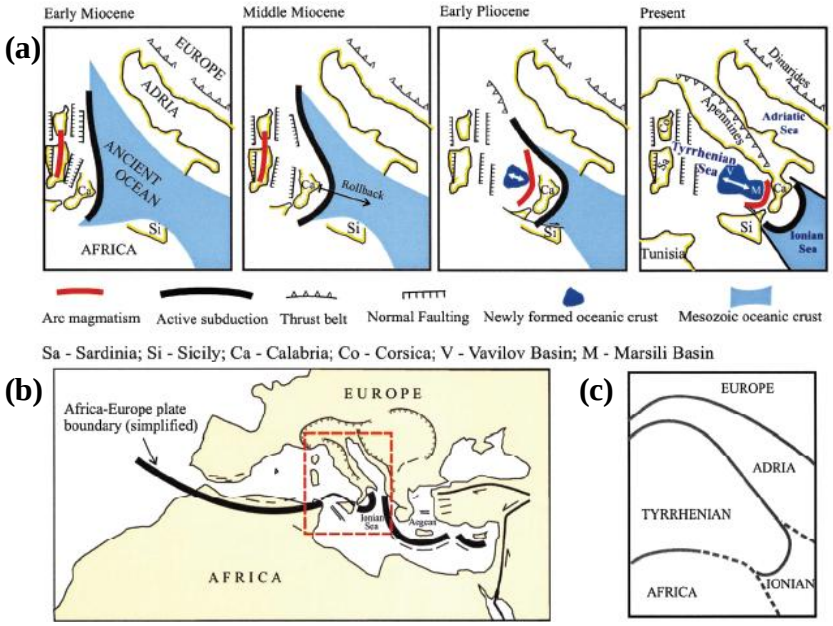

Figure 4.16 **(a) Schematic reconstruction of the central Mediterranean since the Miocene. The eastward retreat of the Tyrrhenian-Apennines subduction system was associated with the closure of a Mesozoic basin and opening of the Tyrrhenian Sea. (b) Regional map showing the studied area (in red frame) within the Europe-Africa convergence zone. (c) Five plates and microplates in the studied area (adapted from Gvirtzman and Nur, 2001).**

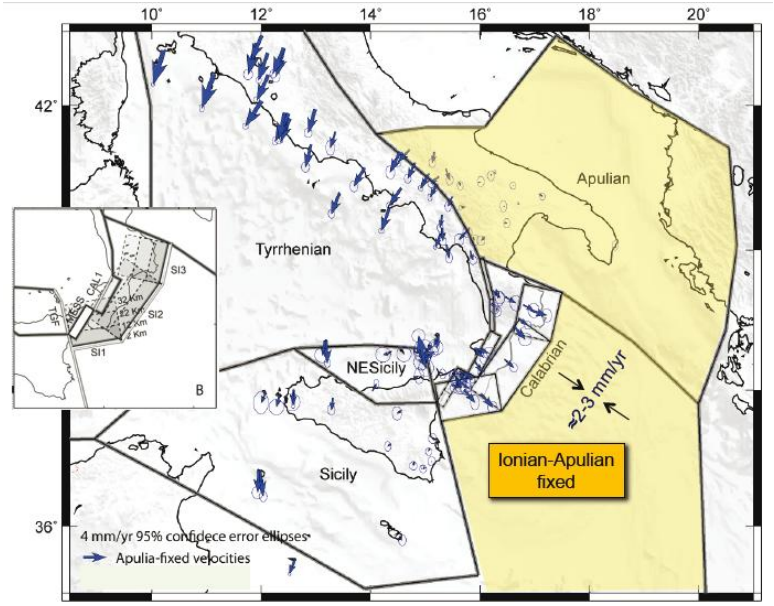

Figure 4.17 **Block model geometry and horizontal GPS velocities (with 95% confidence ellipses) rotated into the Apulia fixed reference frame. Convergence rate across the Ionian-Calabrian subduction interface assuming the Ionian litosphere belonging to the Apulian plate is also shown. (B) Zoom of the Calabrian fault system. For the western Calabrian normal Fault system (CAL1) and the Tindari-Giardini Fault system (TGF) the locking depth varies from 0 to 20 km, whereas for the Calabrian subduction interface (SI1, SI2, and SI3) the locking depth varies from 0 to 40 km (from Mastrolembo Ventura, 2012).**

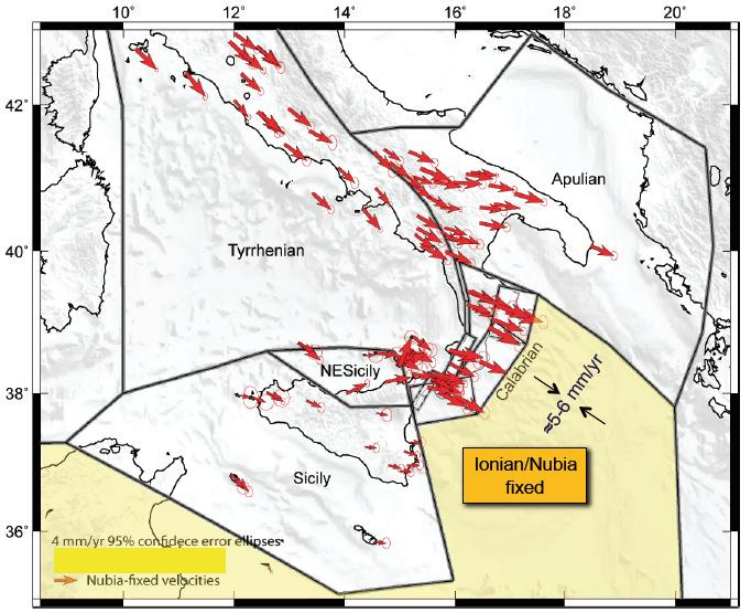

Figure 4.18 **Block model geometry and horizontal GPS velocities (with 95% confidence ellipses) rotated into the Nubia-fixed reference frame. The Ionian plate is assumed moving with Nubia. Ionian-Calabrian convergence rate is shown (from Mastrolembo Ventura, 2012).**

5 GMPE Logic Tree

A ground motion prediction equation (GMPE) relates the log mean and standard deviation of a ground motion intensity measure (such as pseudo-spectral acceleration (PSA) at a given oscillator period) to explanatory variables related to earthquake source, path and site effects. These variables typically include moment magnitude, various metrics of source-to-site distance, style of faulting (faulting mechanism), and site condition.

GMPEs are used with source models in PSHA (e.g. Cornell, 1968, McGuire, 2004). In the sections that follow, we describe the pre-selection of a series of GMPEs considered for application in the hazard analyses for the subject site; we compare the median predictions from pre-selected GMPEs over a parameter space, which is used for final GMPE selection; and we describe the implementation of a recent GMPE that was selected for use in the present application but which had not been previously coded in OQ.

5.1 Pre-Selection of GMPEs

GMPEs are usually derived at least in part from regression of empirical data. Those data and the resulting GMPEs are typically compiled separately for three distinct different tectonic encountered globally: active crustal regions (ACRs) that produce shallow crustal earthquakes, subduction zones (SZs) that produce deep earthquakes on the subducting slab (in-slab activity) and interface events, and stable continental regions (SCRs), among others.

Douglas (2015) summarized 381 GMPEs for the prediction of PGA and 232 for the prediction of PSA ordinates. Hence, the selection of a tractable number of GMPEs for a given application is a significant consideration in PSHA. One fundamental decision faced by the analyst is whether to use GMPEs specific to a country or geographic region versus models derived using global data for the tectonic regime. Local GMPEs have the potential advantage of

reflecting local geologic and tectonic conditions, which may differ from those produced by global models. However, the size of databases used for local models are often very limited and may be inadequate to constrain the model over the parameter space required in PSHA. This is especially problematic for large magnitudes, which are unlikely to have been observed in significant numbers for local regions. Global GMPEs draw from much larger databases and hence are better constrained over the useful parameter range, but may have some bias with respect to local conditions (e.g., rates of distance attenuation and/or site effects).

The PSHA for the Italian building code (MPS working group, 2004; Stucchi et al., 2011) emphasizes local GMPEs at various geographic scales. An Italy-specific GMPE from Sabetta and Pugliese (1996) was used, which is based on an Italian earthquake database (Sabetta and Pugliese, 1987). Also considered was a European model by Ambraseys et al. (1996). Finally, a series of GMPEs specific to sub-regions in Italy by Malagnini et al. (2000, 2002), Morasca et al. (2002), De Natale et al. (1988), and Patanè et al. (1994; 1997) were used.

GMPEs used in the SHARE Euro-Mediterranean model were selected by an expert panel (Delavaud et al., 2012) and are as follows for ACRs:

- Akkar and Bommer (2010) – regional model for Mediterranean and middle east;
- Cauzzi and Faccioli (2008) – global model, but principally comprised of Japanese data;
- Zhao et al. (2006) – model for both ACRs and SZs using data mainly from Japan (almost 90% of the total) plus events from California and Iran;
- Chiou and Youngs (2008a) – part of NGA-West1 project, uses global database by Chiou et al., 2008).

Recently in the framework of the Global Earthquake Model (GEM) Global GMPEs project, coordinated by the Pacific Earthquake Engineering Research Center (PEER), an international expert panel recommended GMPEs for application in PSHA for ACRs, SZs, and SCRs (Stewart et al., 2015). For ACRs, the selected GMPEs were: Akkar and Bommer (2010), Zhao et al. (2006) and Chiou and Youngs (2008a). These GMPEs were selected in consideration of various desirable scaling characteristics described further in the next section and to have the source databases be somewhat distinct in the selected models (Europe, Japan, global, respectively).

In the pre-selection of GMPEs for this study, we considered precedent from prior work in Italy and Europe, various levels of regionalization (from Italy-based to global), and relative levels of model sophistication. The pre-selected models are:

- Italian models: Sabetta and Pugliese (1996) and Bindi et al. (2011).
- European models: Ambraseys et al. (1996) and Akkar and Bommer (2010).
- Global models: Cauzzi and Faccioli (2008), as modified by Faccioli et al. (2010); Zhao et al. (2006); and Boore et al. (2014) (hereafter BSSA14). BSSA14 was developed in the NGA-West2 project (Bozorgnia et al., 2014). The NGA-West2 models supersede those from the original NGA project, including Chiou and Youngs (2008a), which had been selected by SHARE and GEM. BSSA14 contains a regional adjustment specific to Italy to account for a faster rate of anelastic attenuation (Scasserra et al., 2009).

Table 5.1 summarizes key attributes of the pre-selected GMPEs, including the database, magnitude scale and range, source-to-site distance type and range, and the predicted intensity measures (PSA, PGA and/or PGV).

Table 5.1 Characteristics of pre-selected GMPEs for PSHA of Farneto del Principe site

GMPE	Database	Magnitude range and type*	Distance range and type†	Response variables‡
Sabetta and Pugliese (1996)	Italian (1976 – 1984)	4.6 – 6.8 M_S (>5.5) M_L (≤5.5)	1.5 – 100 km R_{epi}, R_{jb}	PGV, PGA PSA (0.04 – 4.0 sec)
Ambraseys et al. (1996)	European (1969 – 1994)	4.0 – 7.9 M_S	0 – 260 km R_{jb} (M_S>6) R_{epi} (M_S≤6)	PGA PSA (0.1 – 2.0 sec)
Akkar and Bommer (2010)	Mediterranean and Middle Eastern (1973 – 2003)	5.0 – 7.6 **M**	0 – 99 km R_{jb}	PGV, PGA PSA (0.01 – 3.0 sec)

(continued on next page)

Table 5.1 (cont.) Summary of the characteristics of the pre-selected GMPEs

GMPE	Database	Magnitude range and type*	Distance range and type†	Response variables‡
Faccioli et al. (2010)	Worldwide Mainly Japanese (1995 – 2005)	4.5 – 7.6 **M**	0.2 – 200 km R_{rup}	PGA PSA (0.05 – 20.0 sec)
Zhao et al. (2006)	Mainly Japanese plus Western USA and Iran (1968 – 2003)	5.0 – 8.3 **M**	0 – 300 km R_{rup}	PGA PSA (0.05 – 5.0 sec)
Bindi et al. (2011)	Italian (1972 – 2009)	4.1 – 6.9 **M**	0 – 200 km R_{jb}	PGV, PGA PSA (0.04 – 2.0 sec)
BSSA14	Worldwide (NGA2 – West) (1935 – 2011)	3.0 – 7.9 **M**	0 – 400 km R_{jb}	PGV, PGA PSA (0.01 – 10.0 sec)

*Ms = surface wave magnitude; M_L = local magnitude; **M** = moment magnitude.

†R_{jb} = closest distance to surface projection of rupture surface, referred to as Joyner and Boore (1981) distance; R_{epi} = Epicentral distance; R_{rup} = rupture distance.

‡PGA = Peak ground acceleration; PGV = peak ground velocity PSA = Pseudo-spectral acceleration (periods in seconds).

5.2 GMPE Comparisons and Selection

We seek to select GMPEs from the pre-selected models listed in Table 5.1 for application in PSHA. Factors considered in the selection include those used for the GEM project (Stewart et al., 2015) in combination with the need to capture features specific to the application region in southern Italy. One of the key considerations in the GEM selections was comparative interpretation of GMPE scaling with respect to magnitude, distance, and period. Site scaling is not of interest in the present work because the hazard analysis is being performed for firm site conditions.

Comparisons of the pre-selected GMPEs are complicated by non-uniform magnitude scales, distance metrics, and the lack of focal mechanism terms in the older GMPEs by Sabetta and Pugliese (1996) and Ambraseys et al. (1996). We seek to compare GMPE median scaling with

respect to moment magnitude (**M**), distance to surface projection of fault (R_{jb}), and oscillator period. We emphasize comparisons for normal faulting conditions, since this is the dominant focal mechanism near the Farneto del Principe site.

With regard to focal mechanism, for the older GMPEs of by Sabetta and Pugliese (1996) and Ambraseys et al. (1996), we apply multiplicative correction factors to the GMPE median (in arithmetic units) for different styles of faulting, following the approach of Bommer et al. (2003). The specific factors that were applied were derived by Stucchi et al. (2011) and are given in Table 5.2. These correction factors were previously used in the PSHA for the Italian building code.

Table 5.2 Style of faulting correction factors

Model	Normal	Reverse	Strike-slip
Sabetta and Pugliese (1996)	0.89	1.15	0.94
Ambraseys et al. (1996)	0.88	1.13	0.93

Magnitude scale conversions are required for Sabetta and Pugliese (1996) and Ambraseys et al. (1996) to convert from surface wave and local magnitude (M_S and M_L) to moment magnitude (**M**). All other pre-selected GMPEs use moment magnitude. The Sabetta and Pugliese (1996) GMPE has different magnitude definitions for two ranges of earthquake size: M_L for $M_L \leq 5.5$ and M_S for $M_S > 5.5$. We first convert local to surface wave magnitude following the recommendations of Gasperini et al. (2004):

$$M_S = \begin{cases} \dfrac{(M_L + 0.584)}{1.079}, & M_L \leq 5.5 \\ M_S, & M_S > 5.5 \end{cases} \tag{5.1}$$

Surface wave magnitude is then converted to moment magnitude using the approach of Lolli et al. (2014), which is considered valid for Italian earthquakes:

$$\mathbf{M} = \exp(1.421 + 0.108 \cdot M_S) - 1.863 \tag{5.2}$$

The Ambraseys et al. (1996) GMPE is defined for M_S and the conversion in Eq. (5.2) was applied.

We adopt R_{jb} as the reference distance metric (Joyner and Boore, 1981), because it captures finite source effects, approximately captures hanging wall effects, and has practical utility given the common usage of area and background sources in the source modeling. The adoption of R_{jb} requires distance metrics used in other GMPEs (epicentral distance, $R_{epi,}$ and rupture distance R_{rup}) to be converted to R_{jb} for the comparative GMPE scaling plots. The conversion is based on the Kaklamanos et al. (2011) approach in which dip angle is estimated from focal mechanism and hypocentral depth and fault dimensions are estimated from **M**. This information, combined with an assumption regarding hypocenter location along the fault width, allows the fault geometry to be fully defined, which in turn enables the relative values of R_{jb} and R_{rup} to be evaluated.

Figure 5.1 shows the various parameters describing fault geometry, assuming a planar source (the only missing parameter in the figure is the along-strike fault length, L). The parameters shown in the figure that have not been introduced previously are top of rupture depth (Z_{tor}), horizontal distance from site to a line drawn along the fault strike above the shallowest portion of the fault (R_x) and fault width (W). The average dip angles (δ) for a given style of faulting (normal, reverse or strike-slip) are as shown in Table 5.3. The dip angles in the table are modified from the guidelines of Chiou and Youngs (2008b).

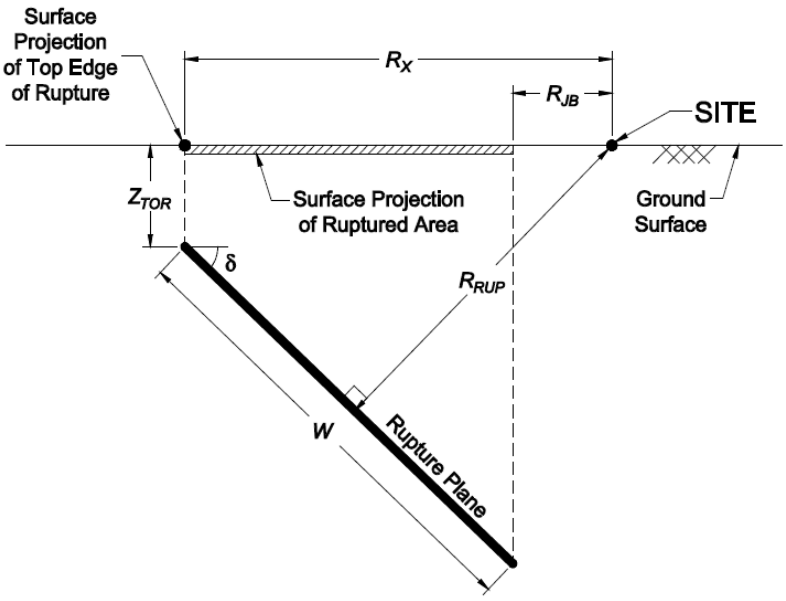

Figure 5.1 **Scheme of an earthquake source and distance measures using a vertical cross-section through a fault rupture plane (from Kaklamanos et al., 2011).**

Table 5.3 Dip angle estimation for a given style of faulting (Kaklamanos et al, 2011).

Style of faulting	Dip angle, δ (deg)
Normal	50
Reverse	40
Strike-slip	90

Hypocentral depth (Z_{HYP}) is estimated from **M** using the linear relationships from Scherbaum et al. (2004):

$$Z_{HYP} = \begin{cases} 5.63 + 0.68 \cdot \boldsymbol{M}, & strike-slip\ faults \\ 11.24 - 0.2 \cdot \boldsymbol{M}, & non-strike-slip\ faults \end{cases} \quad (5.3)$$

Down-dip rupture width (W) and along-strike length (L) are estimated from **M** and style of faulting by using the logarithmic relationships by Wells and Coppersmith (1994):

$$W = \begin{cases} 10^{-0.76+0.27 \cdot \boldsymbol{M}} & strike-slip\ faults \\ 10^{-1.61+0.41 \cdot \boldsymbol{M}} & reverse\ faults \\ 10^{-1.14+0.35 \cdot \boldsymbol{M}} & normal\ faults \end{cases} \quad (5.4)$$

$$L = \begin{cases} 10^{-2.57+0.62 \cdot \boldsymbol{M}} & strike-slip\ faults \\ 10^{-2.42+0.58 \cdot \boldsymbol{M}} & reverse\ faults \\ 10^{-1.88+0.50 \cdot \boldsymbol{M}} & normal\ faults \end{cases} \quad (5.5)$$

Assuming that the hypocenter is located 60 percent down the fault width, as suggested by Mai et al. (2005), it is possible to define the depth to top of rupture (Z_{TOR}) as:

$$Z_{TOR} = Z_{HYP} - (0.6 \cdot W \cdot \sin\delta) \quad (5.6)$$

We take the hypocenter location along the fault length as uniformly distributed and assume the hypocenter to be centered within the rupture length. With these parameters defined, the fault location is full specified, allowing R_{rup} to be computed from R_{jb} and vice-versa.

For the Ambraseys et al. (1996) model, a conversion between R_{epi} and R_{jb} was used. The epicenter is defined as the point on the surface directly above the hypocenter. For R_{jb} = 0, the Kaklamanos et al. (2011) methodology is applied, assuming that the site is located in the middle of the surface projection of the rupture area.

$$R_{epi} = \begin{cases} R_{jb} + 0.4 \cdot W \cdot \cos\delta\,, & R_{jb} > 0 \\ 0.1 \cdot W \cdot \cos\delta\,, & R_{jb} = 0 \end{cases} \quad (5.7)$$

Based on the above conversions, all the pre-selected GMPEs can be compared on common sets of axes in terms of their spectral shapes, magnitude-scaling, and distance-scaling. The comparisons are shown in trellis charts similar in format to those used in the GEM project (Stewart et al., 2015). All trellis plots are prepared for a normal style of faulting mechanism and rock site conditions (V_{S30} = 800 m/s).

Figure 5.2 shows PSA trellis chart for **M** = 5, 6, and 7 and R_{jb} = 10, 30, 100 km using the pre-selected GMPEs. The spread between models is much greater at 100 km than for shorter distances in each **M** bin. This is unexpected because the available data at large distance is generally much greater than at close distance, hence model variability should be minimized.

However, the variability in this case is driven in part by functional form – the BSSA14, Zhao et al. (2006), Akkar and Bommer (2010), and Bindi et al. (2011) models include an anelastic attenuation term (and have lower PSA at large distance) whereas the Faccioli et al. (2010), Sabetta and Pugliese (1996) and Ambraseys et al. (1996) models do not. The spectra for the Faccioli et al. (2010) model often have unusual shapes, which could be due to a limited number of records having rock-like site conditions (discussed also in Stewart et al. 2015). For the largest magnitude and largest distances the Sabetta and Pugliese (1996) and the Ambraseys et al. (1996) models are high relative to other models. The Bindi et al. (2011) and BSSA14 models, which include local effects and relatively large databases, predict the lowest values.

Figure 5.3 shows distance-scaling for the pre-selected GMPEs for PSA at three oscillator periods: T = 0 (PGA), 0.3s, and 1.0 sec. The effect of the anelastic attenuation term is evident by curvature in the attenuation plots for distances larger than about 70-100 km; these effects are evident for PGA and 0.3 sec PSA but not for 1.0 sec PSA. The BSSA14, Zhao et al. (2006), Akkar and Bommer (2010), and Bindi et al. (2011) models exhibit effective anelastic attenuation. The models of Faccioli et al. (2010), Sabetta and Pugliese (1996) and Ambraseys et al. (1996) do not have anelastic attenution terms. As noted previously, the Sabetta and Pugliese (1996) and Ambraseys et al. (1996) models often predict larger ground motions than the other models.

Figure 5.4 shows the magnitude-scaling of the pre-selected GMPEs for R_{jb} = 10, 30, 100 km and oscillator periods 0, 0.3, and 1.0 sec. The models of Faccioli et al. (2010), Bindi et al. (2011), Sabetta and Pugliese (1996) and Ambraseys et al. (1996) do not exhibit magnitude saturation effects, because the ordinates scale linearly with **M** over the range considered.

Magnitude saturation effects are well established from GMPEs that utilize data sets that include large **M** events. Hence, GMPEs lacking this effect are deficient for hazard applications, which typically are very sensitive to predictions for large-**M** conditions.

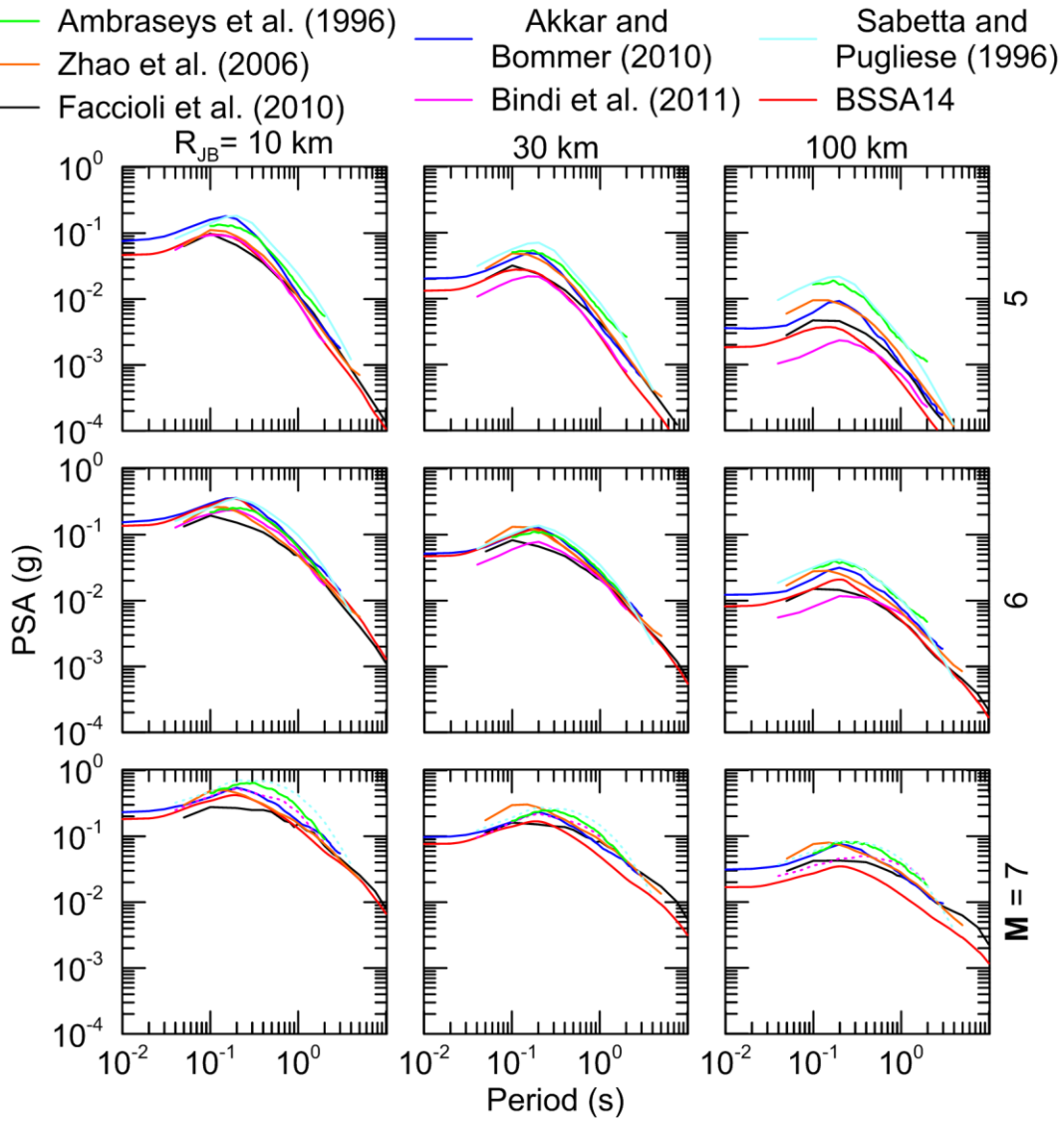

Figure 5.2 **Trellis chart showing predicted PSAs for pre-selected GMPEs for M= 5, 6, 7, R_{jb} = 10, 30, 100 km and rock site conditions (V_{S30} = 800 m/s). Dotted lines indicate where the scenario falls outside the published distance range for the model.**

In consideration of these observations from trellis plots, we select three models that we consider technically defensible and to capture epistemic uncertainties. The selected models are: Akkar and Bommer (2010), Zhao et al. (2006), and BSSA14. These are the same models recommended for ACRs for the GEM project (Stewart et al., 2015), except that BSSA14 has

replaced Chiou and Youngs (2008a). The models exhibit desirable scaling characteristics, including anelastic attenuation and the magnitude saturation effects. The BSSA14 model has the desirable attribute of having a regional adjustment for anelastic attenuation effects, to capture faster attenuation in Italy as compared to ACRs generally.

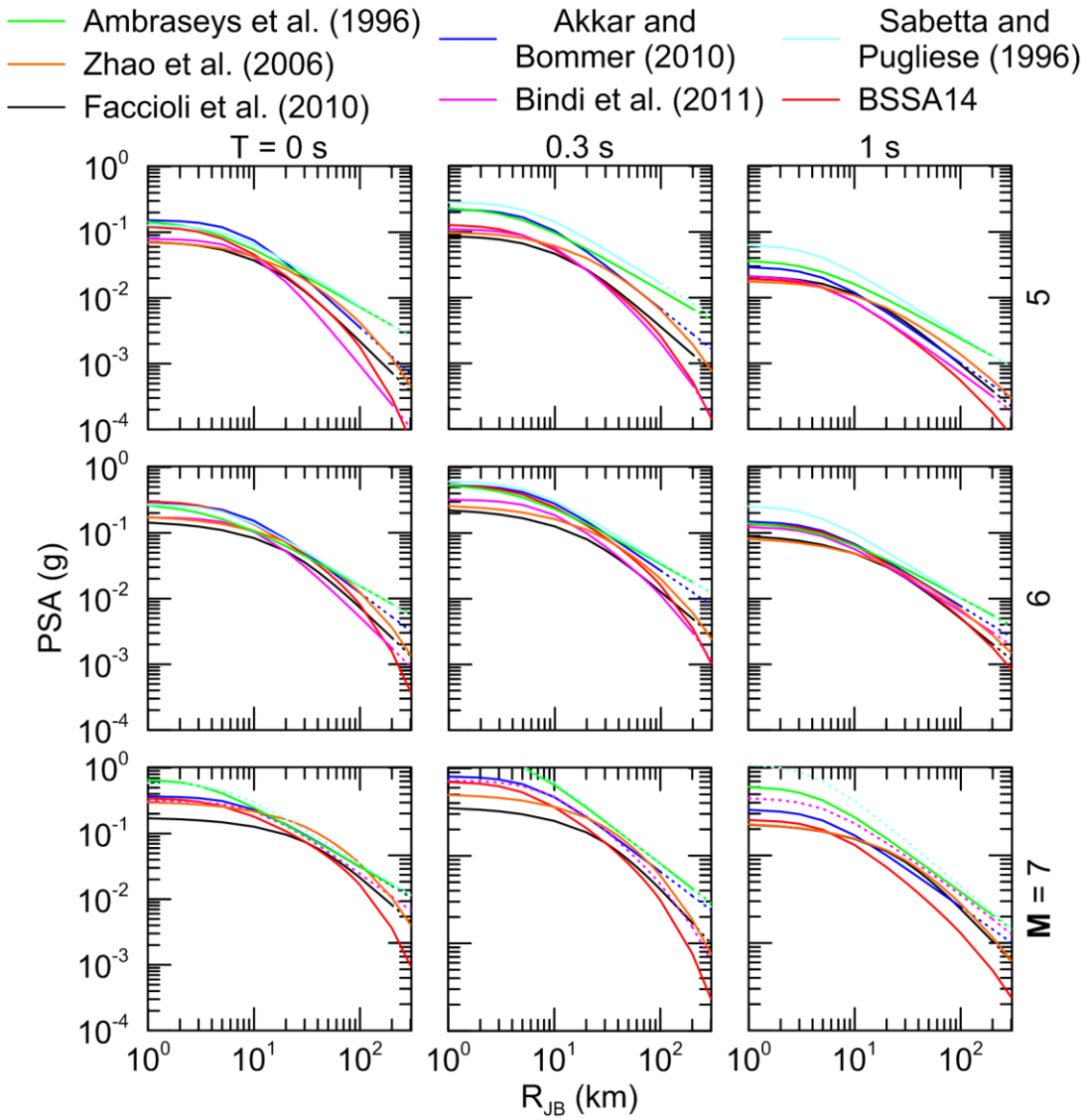

Figure 5.3 **Trellis chart showing distance-scaling for pre-selected GMPEs for M = 5, 6, 7, T = 0s, 0.3s and 1s and rock site conditions (V_{S30} = 800 m/s). Dotted lines indicate where the scenario falls outside the published distance range for the model.**

GMPEs for subduction zone ground motions have been selected previously by the SHARE project (Delavaud et al., 2012) and GEM project (Stewart et al., 2015). GMPEs selected for use in both projects are Zhao et al. (2006) and Atkinson and Boore (2003), which capture variable

rates of distance attenuation that capture epistemic uncertainty. We select these same models. While the GEM project also selected Abrahamson et al. (2015), this model was not selected for the present application because it is not currently implemented in OQ.

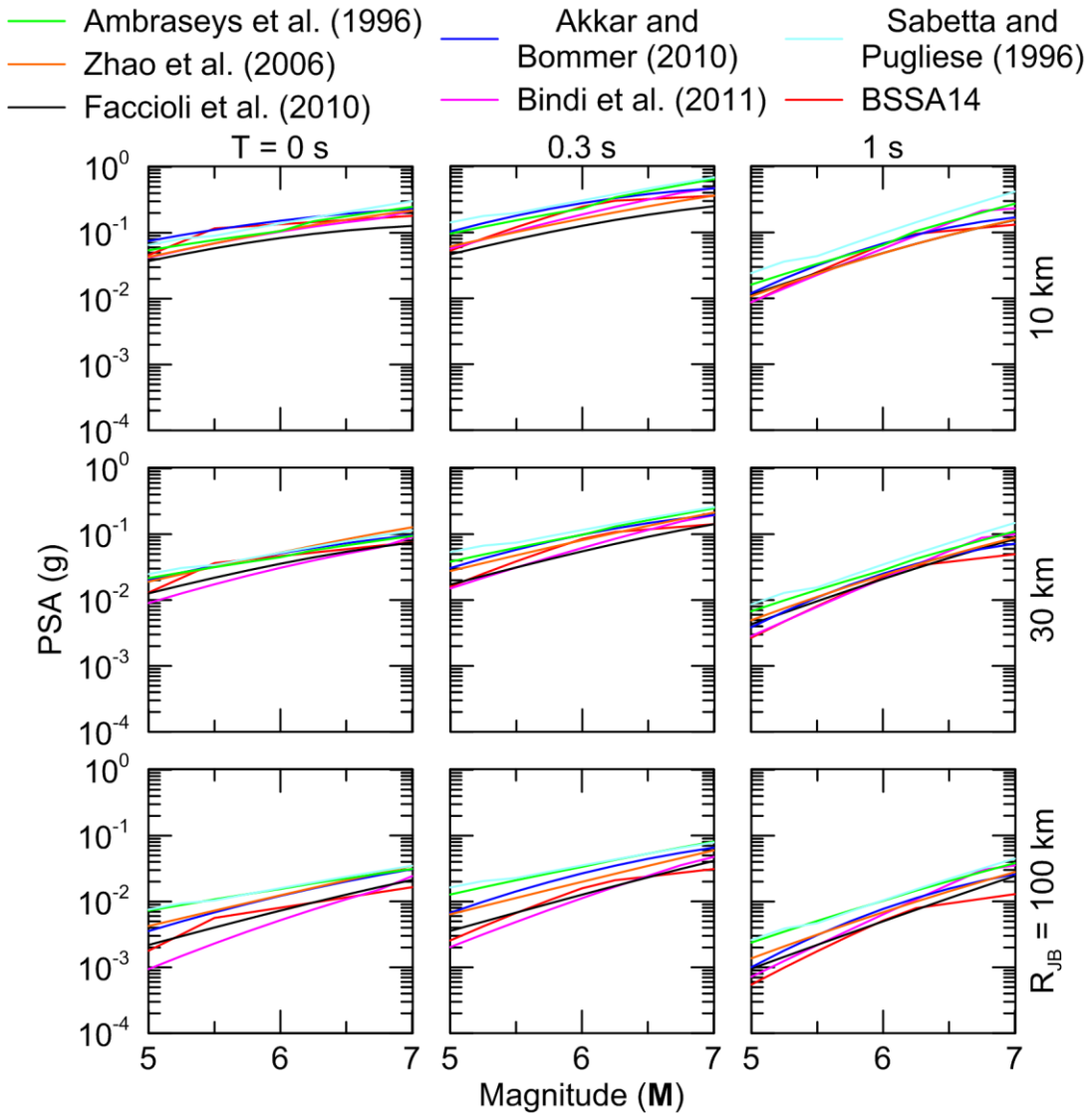

Figure 5.4 **Trellis chart showing magnitude-scaling for pre-selected GMPEs for M = 5, 6, 7, R_{jb} = 10, 30, 100 km and rock site conditions (V_{S30} = 800 m/s).**

Figure 5.5 shows the GMPE logic tree used in this study for ACRs and SZs. We give equal weight to the models in each branch.

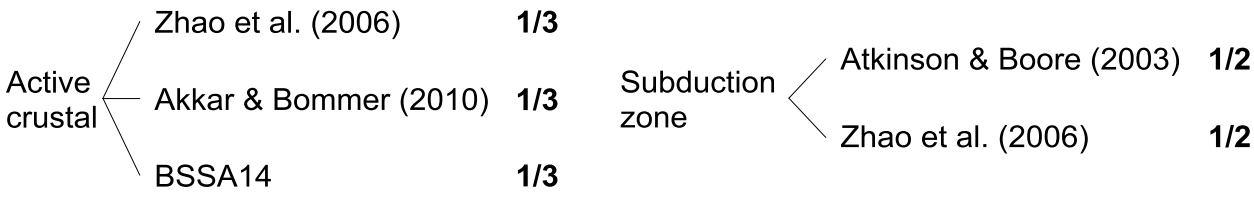

Figure 5.5 GMPE logic tree for active crustal regions and subduction zones (in-slab and interface) used in this study

5.3 BSSA14 Implementation in OQ Engine

We implemented the BSSA14 model in OQ as part of this project. According to Pagani et al. (2014a), the incorporation of new GMPEs is among the most important challenges for maintaining PSHA software in the long-term. The OQ developers facilitate the implementation of new GMPEs by extending or creating base classes (or templates), which ensure that new GMPEs output the information required by the software. Following GMPE coding and implementation, test tables are defined to check the correct implementation/coding of a new GMPE. A test table provides medians and standard deviations for all possible combinations of the predictor variables in the GMPE functional form Once test tables are defined, typically from codes provided by GMPE authors, OQ implements a testing protocol (discussed in §3) for comparing medians and standard deviations for many combinations of predictor variables.

Ground motions are predicted from the BSSA14 GMPE as follows:

$$lnY = F_E(\mathbf{M}, mech) + F_P\left(R_{jb}, \mathbf{M}, region\right) + F_S\left(V_{S30}, R_{jb}, \mathbf{M}, z_1\right) + \varepsilon_n \sigma(\mathbf{M}, V_{S30}, R_{jb}) \quad (5.8)$$

were lnY represents the natural logarithm of a ground motion intensity measure (PGA, PGV or PSA); F_E, F_P and F_S represent functions for source ("E" for "event"), path ("P") and site ("S") effects, respectively, while ε_n is the fractional number of standard deviations of a single predicted value of lnY away from the mean, and, σ is the total standard deviation of the model. The predictor variables are magnitude (**M**), source-to-site distance (R_{jb}), average shear wave velocity in the upper 30m (V_{S30}), basin depth parameter (z_1) and the parameter *mech*, used to distinguish among style of faulting (*mech*=1, for strike-slip (SS), 2 for normal (NS), 3 for reverse (RS) and 0 for unspecified).

The source (event) function (F_E) is given as:

$$F_E(M, mech) = \begin{cases} e_0 U + e_1 SS + e_2 NS + e_3 RS + e_4(\mathbf{M} - \mathbf{M}_h) + e_5(\mathbf{M} - \mathbf{M}_h)^2 & \mathbf{M} \leq \mathbf{M}_h \\ e_0 U + e_1 SS + e_2 NS + e_3 RS + e_6(\mathbf{M} - \mathbf{M}_h) & \mathbf{M} > \mathbf{M}_h \end{cases} \quad (5.9)$$

where *U*, *SS*, *NS*, and *RS* are dummy variables, with a value of 1 to specify strike-slip, normal-slip, and reverse-slip fault types, respectively, and 0 if the fault type is unspecified; the hinge magnitude $\mathbf{M}_h$ is period-dependent, and e_0 to e_6 are model coefficients.

The path function (F_p) is given as:

$$F_P(R_{jb}, \mathbf{M}, region) = [c_1 + c_1(\mathbf{M} - \mathbf{M}_{ref})] ln\left(\frac{R}{R_{ref}}\right) + (c_3 + \Delta c_3)(R - R_{ref}) \quad (5.10)$$

where

$$R = \sqrt{R_{jb}^2 + h^2} \quad (5.11)$$

c_1, c_2, c_3, M_{ref}, R_{ref} and h are model coefficient. Parameter c_3 is the apparent anelastic attenuation coefficient and Δc_3 is the regional correction to this coefficient that depends on the geographic region. The authors of this model provide tables containing a regional correction derived specifically for Italy and Japan (which show similarly fast distance attenuation trends). This regional correction for Italy was used in the OQ implementation of this model.

The site function is given by:

$$F_S(V_{S30}, R_{jb}, \boldsymbol{M}, z_1) = \ln(F_{lin}) + \ln(F_{nl}) + F_{\delta z_1}(\delta z_1) \quad (5.12)$$

where F_{lin} represents the linear component, F_{nl} the nonlinear component of site amplification, and $F_{\delta z1}$ the effects of basin depth. When z_1 is unknown, the recommended default value of δ_{z1} is 0, which turns off the adjustment factor. This is a reasonable condition because the remaining elements of the model are "centered" on a condition of no F_{dz1} adjustment (Boore et al., 2014). In the OQ implementation used in this study, δ_{z1} was set to 0.

The linear component of the site amplification model (F_{lin}) is given by:

$$\ln(F_{lin}) = \begin{cases} cln\left(\frac{V_{S30}}{V_{ref}}\right) & V_{S30} \leq V_c \\ cln\left(\frac{V_c}{V_{ref}}\right) & V_{S30} > V_c \end{cases} \quad (5.13)$$

where c describes the V_{S30} scaling, V_c is the limiting velocity beyond which ground motions no longer scale with V_{S30} and V_{ref} is the site condition for which the amplification is equal to one (taken as 760 m/s).

The non-linear component of the site amplification model (F_{nl}) is given by:

$$\ln(F_{nl}) = f_1 + f_2 ln\left(\frac{PGA_r}{f_3}\right) \tag{5.14}$$

where f_1, f_2 and f_3 are model coefficients and PGA_r is the median peak horizontal acceleration for reference rock condition (V_{S30} = 760 m/s). Parameter f_2 represents the degree of nonlinearity and is given as:

$$f_2 = f_4\{exp[f_5(\min(V_{s30}, 760) - 360]\} - exp[f_5(760 - 360)] \tag{5.15}$$

where f_4 and f_5 are model coefficients.

The total standard deviation σ is partitioned into components that represent between-event variability (τ) and within-event variability (ϕ) as.

$$\sigma(\boldsymbol{M}, R_{jb}, V_{S30}) = \sqrt{\phi^2(\boldsymbol{M}, R_{jb}, V_{S30}) + \tau^2(\boldsymbol{M})} \tag{5.16}$$

The between-event variability is given as:

$$\tau(\boldsymbol{M}) = \begin{cases} \tau_1 & \boldsymbol{M} \leq 4.5 \\ \tau_1 + (\tau_2 - \tau_1)(\boldsymbol{M} - 4.5) & 4.5 < \boldsymbol{M} < 5.5 \\ \tau_2 & \boldsymbol{M} \geq 5.5 \end{cases} \tag{5.17}$$

The within-event standard deviation is given as:

$$\phi(\boldsymbol{M}, R_{jb}, V_{S30}) = \begin{cases} \phi(\boldsymbol{M}, R_{jb}) & V_{S30} \geq V_2 \\ \phi(\boldsymbol{M}, R_{jb}) - \Delta\phi_V \left(\dfrac{\ln\left(V_2/V_{S30}\right)}{\ln\left(V_2/V_1\right)} \right) & V_1 \leq V_{S30} \leq V_2 \\ \phi(\boldsymbol{M}, R_{jb}) - \Delta\phi_V & V_{S30} \leq V_1 \end{cases} \tag{5.18}$$

where

$$\phi(\boldsymbol{M}, R_{jb}) = \begin{cases} \phi(\boldsymbol{M}) & R_{jb} \leq R_1 \\ \phi(\boldsymbol{M}) + \Delta\phi_R \left(\dfrac{\ln\left(R_{jb}/R_1\right)}{\ln\left(R_2/R_1\right)} \right) & R_1 < R_{jb} \leq R_2 \\ \phi(\boldsymbol{M}) + \Delta\phi_R & R_{jb} > R_2 \end{cases} \quad (5.19)$$

The implementation of the BSSA14 model in OQ was performed creating a new python class**.** The OQ verification tools were used to compare BSSA14 medians and standard deviations as implemented in OQ and in test tables built using a Matlab™ script. More than 10000 checks were performed, a summary of which is given in Table 5.4. If a maximum tolerable discrepancy is set as 0.5%, the success rate of the tests is 100%.

Table 5.4 Summary of the tests performed in the newly implemented GMPE (BSSA14)

Value	Average discrepancy (%)	Maximum discrepancy (%)	Standard deviation
Median	0.1186	0.4749	0.0866
Total standard deviation	0.0347	0.0881	0.0209

6 Hazard Results for Farneto del Principe Dam Site

6.1 Hazard Curves

A fundamental outcome of PSHA is the relationship between probability of exceedance within a specified time interval and the intensity measure amplitude, which is known as a seismic hazard curve.

Seismic hazard curves for the Farneto del Principe dam site were computed for the intensity measures (IMs) of PGA as well as PSAs at the elastic first-mode natural period of the system (dam plus deformable foundation) T_1 = 0.25 sec, second elastic natural period T_2 = 0.125 sec, 0.5 sec (twice T_1), 1.0 sec (four times T_1) and 0.15 sec (period having the maximum PSA). Hazard curves are computed for all combinations of source models and GMPEs to account for epistemic uncertainties. OQ internally assembles a cumulative distribution function (CDF) of computed probabilities for a given IM that takes into account their relative weights. Based on that weighted CDF, percentiles of probability are evaluated by OQ for a given value of IM. In Figure 6.1, the median (50^{th}), 5^{th}, 25^{th}, 75^{th} and 95^{th} percentile hazard curves are shown for the six selected intensity measures.

Figure 6.2 shows a representative plot of computed probabilities of exceedance vs. quantile for the IM of 0.25 sec PSA at a ground motion amplitude of 0.1g. The median probability (0.5 quantile) for this amplitude is 0.086. As shown in Figure 6.2, the distribution of probabilities about the median is better approximated as normal than log normal. The coefficient of variation of the fit distribution is approximately 0.5. This is a large scatter that reflects a strong impact of epistemic uncertainty in the hazard estimates at the site. Inspection of Figure 6.1 indicates that the general features of the distribution in Figure 6.2 do not always hold, but are relatively common, especially at high hazard levels (low probabilities). We recognize that confidence

intervals on the mean hazard curve are generally of greatest practical interest – these will be added in subsequent refinements of the ground motion computations.

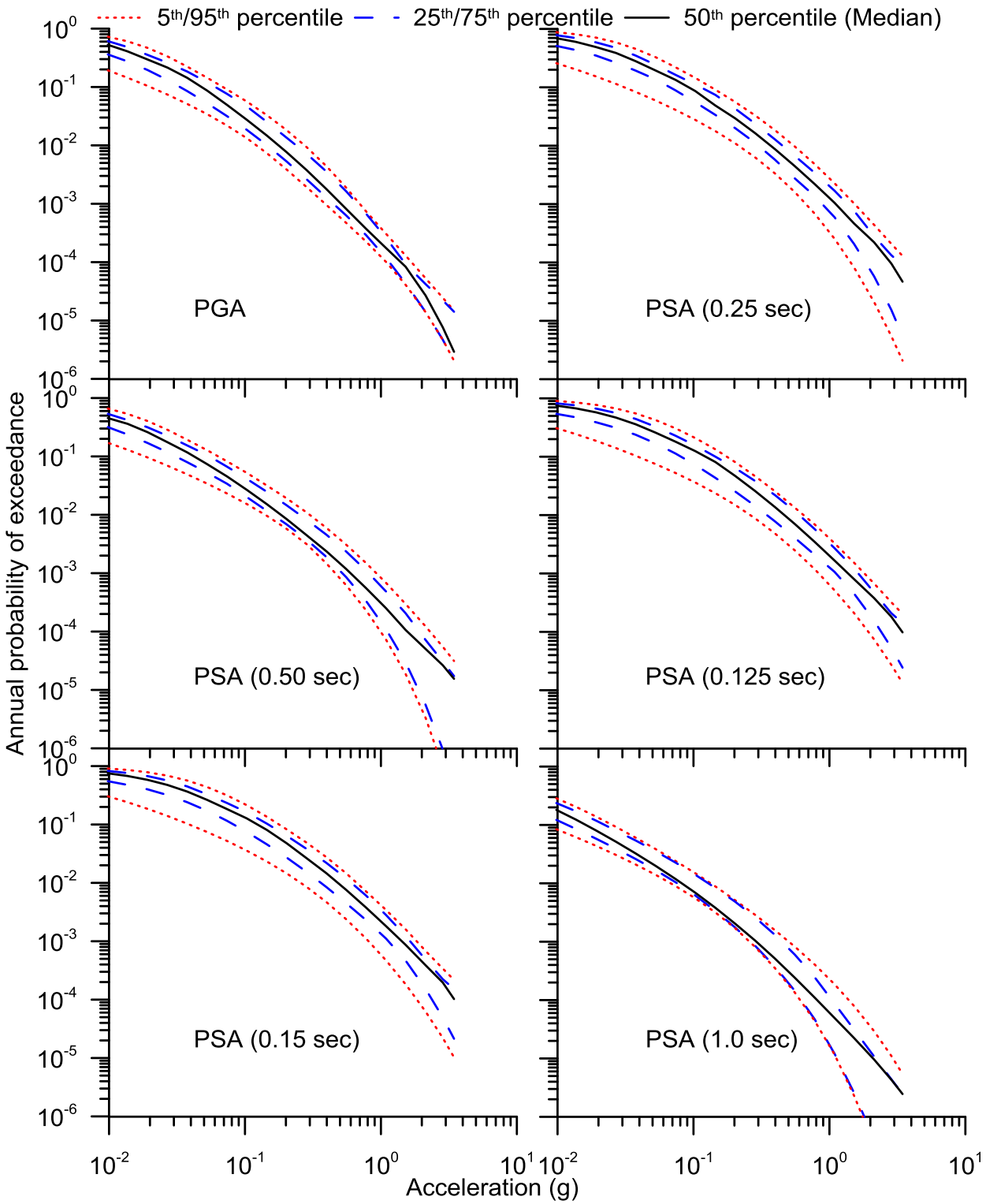

Figure 6.1 **Percentile seismic hazard curves for Farneto del Principe dam site for several intensity measure levels.**

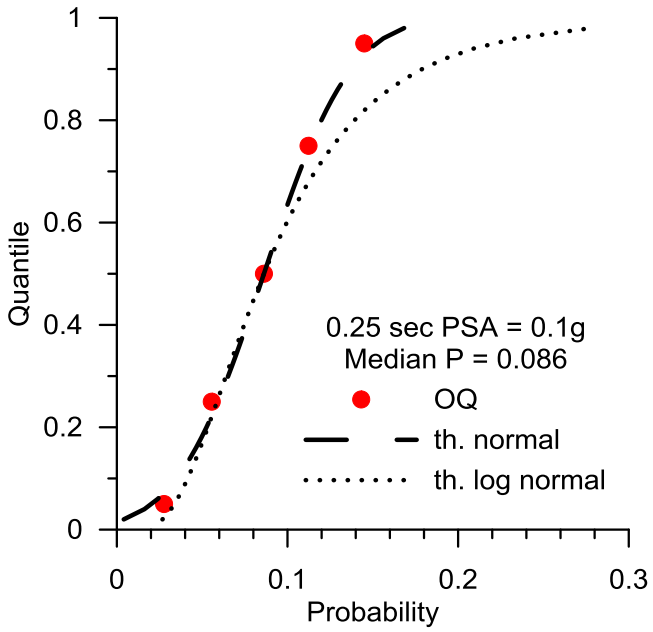

Figure 6.2 **Computed probabilities of exceedance vs. quantile for the IM of 0.25 sec PSA at a ground motion amplitude of 0.1g.**

To provide context on the level of hazard at the Farneto del Principe dam site, we compare the median hazard for PGA and 1.0 sec PSA to results for two other locations in the western and central United States. The western US (WUS) location is in Los Angeles, CA (Lat. 34.05372 deg, Lon. -118.24273 deg) and is known to be among the most active seismic region in the world. The central US located is Clinton, IL (Lat. 40.1536 deg, Lon. -88.9645 deg), which is a stable continental region. Hazard results for the WUS and central US sites are provided by the Hazard Curve Application of the United States Geological Survey (USGS), which provides mean values of acceleration for selected hazard levels; http://geohazards.usgs.gov/hazardtool/application.php (last accessed October 2015).

Figure 6.3 compares mean hazard curves for the subject site in Calabria, and the Los Angeles, CA and Clinton, IL comparison sites. As expected, the CEUS site has much lower hazard. The PGA hazard for the Italian and Los Angeles sites are comparable for PGA, while the 1.0 sec PSA hazard is higher in Los Angeles, due to the presence of faults producing larger **M** events (the discrepancy increases with oscillator period).

Probabilistic analysis of the response of systems to earthquakes involves the convolution of hazard curves with system fragility. The convolution uses the absolute value of the slope of the hazard curve, which we compute as:

$$f_X(x) = \frac{\partial v(IM)}{\partial IM} \tag{6.1}$$

where $f_X(x)$ represents the probability density for ground motion level x and $\delta v(IM)$ is the differential on the exceedance rate of IM (practically equal to the differential of the annual exceedance probability). Numerically differentiating the rock-hazard curve of Figure 6.3, we obtain corresponding slopes $f_X(x)$ in Figure 6.4. The patterns in slope mirror those for hazard.

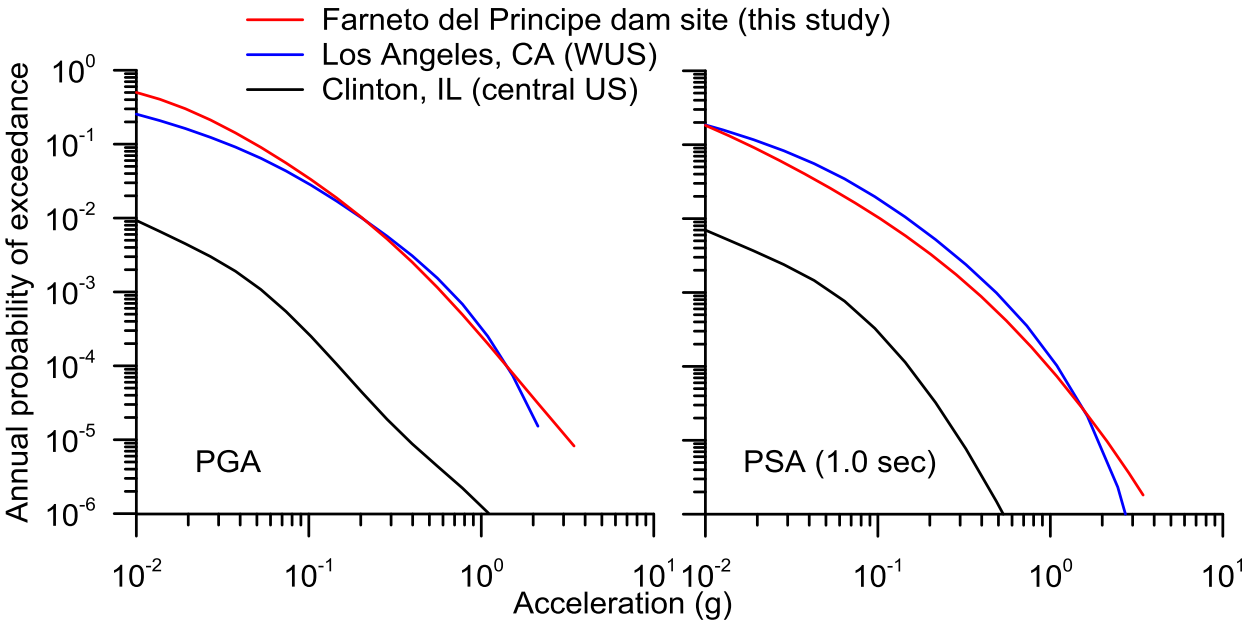

Figure 6.3 **Mean seismic hazard curves for Farneto del Principe dam site (This study), Los Angeles, CA (WUS) and Clinton, IL (central US).**

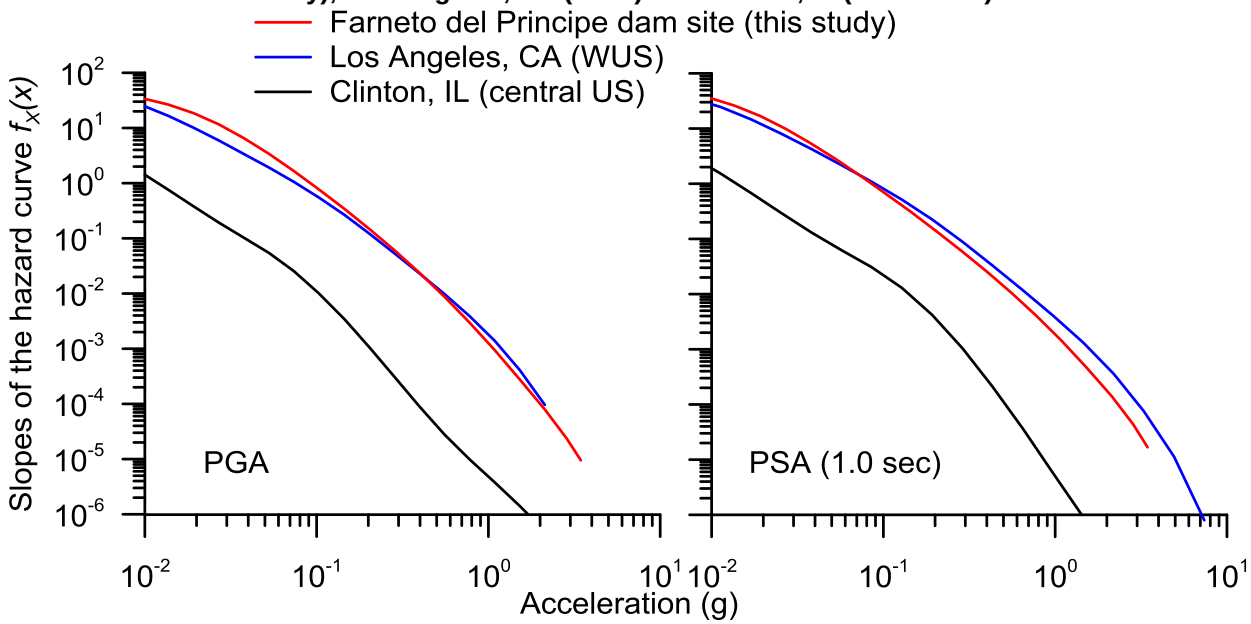

Figure 6.4 **Slopes of the mean hazard curves for Farneto del Principe dam site (This study), Los Angeles, CA (WUS) and Clinton, IL (central US).**

6.2 Uniform Hazard Spectra (UHS)

Uniform hazard spectra (UHS) are PSA ordinates sharing a common probability of exceedance for a specified time span. The UHS is a common product of PSHA, often being used for response spectrum methods of analysis for structures or as the target spectrum for acceleration time series scaling/modification.

For application to the Farneto del Principe dam site, we select return periods associated with a 10% and 2% probabilities of exceedance in 50 years (T_R = 475 and 2475 years, respectively). The T_R = 475-year hazard level is considered representative of moderate events that are reasonably likely to affect the structure in its design life. The T_R = 2475-year hazard level represents for large relevant dams, such as the Farneto del Principe dam, "*the collapse limit state performance level*" according to the Italian code for dam design and safety (Decreto Ministeriale, D.M. June 14, 2014).

Figure 6.5 shows median UHS for the two hazard levels at the subject site. We use median ordinates in this case for compatibility with previous Italian sources; in general we prefer mean ordinates per McGuire et al. (2005). Also shown for reference are median UHS for this site derived using the SHARE Euro-Mediterranean model (Giardini et al., 2013, Woessner et al., 2015) and from two Italian national sources:

1. PSHA performed for the Italian Department for Civil Protection (DPC) by Istituto Nazionale di Geofisica e Vulcanologia (INGV) as part of national research projects from 2004–2006 (MPS working group, 2004; Stucchi et al., 2011). Labelled as 'INGV-DPC' in Figure 6.5, these spectral ordinates were obtained from the web-site http://esse1-gis.mi.ingv.it/ (last accessed October 2015). The hazard results provided from this source are median values.

2. A simplified shape representing approximately the UHS from (1) for application in the Italian Building Code by the Consiglio Superiore dei Lavori Pubblici (Norme Tecniche per le Costruzioni, NTC, 2008). This UHS is labelled 'Italian Building Code (2008)'.

3. The UHS from the present analysis peaks at about 0.15 sec, which is consistent with the shape from the SHARE model but distinct from that in the Italian code and

national PSHA, which peaks at around 0.2-0.4 sec. The different spectral shape is likely caused by the use of older GMPEs (Sabetta and Pugliese, 1996 and Ambraseys et al., 1996) in the analyses for the Italian national PSHA. Those GMPEs have some significant differences from contemporary models including a limited number of events in the catalogues, a lack of rock-like records and certain deficiencies in their functional form (details in §5.2). The SHARE Euro-Mediterranean model produces a similar spectral shape to the results of the present analysis, presumably due to the use of relatively modern GMPEs in the logic tree.

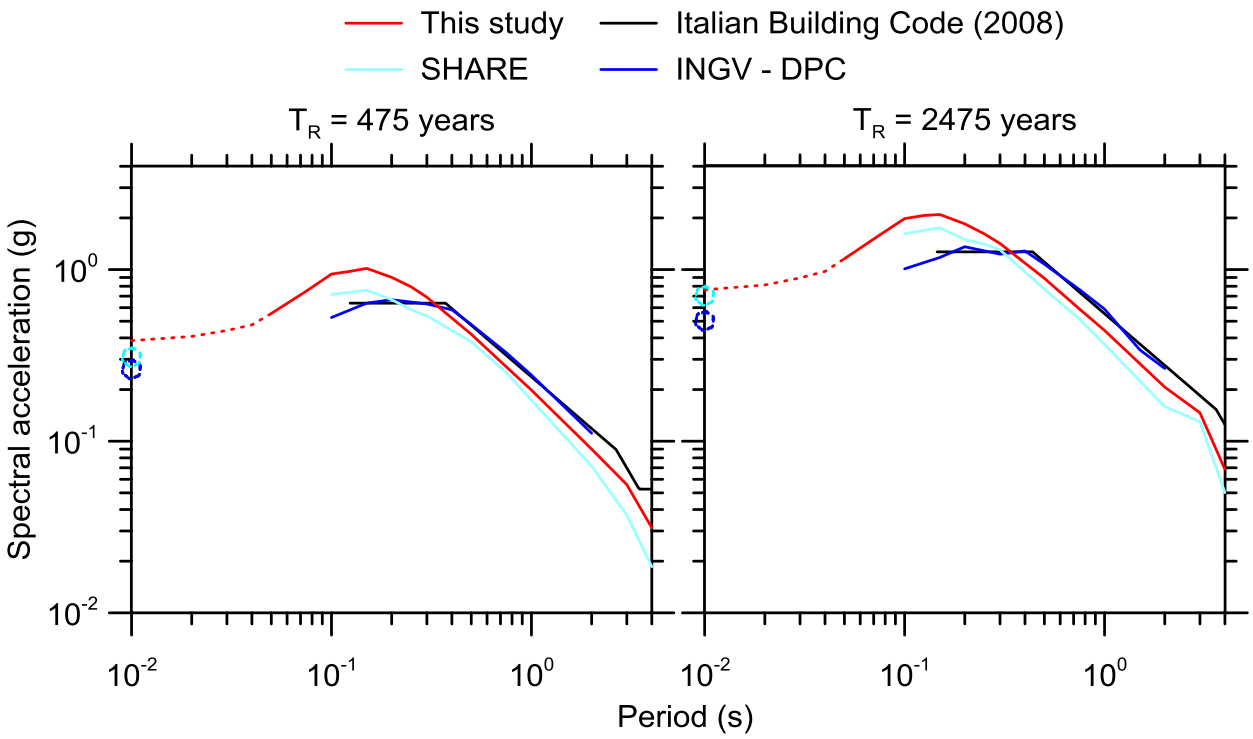

Figure 6.5 **Comparison of the median UHS from this study, the SHARE Euro-Mediterranean model (Giardini et al., 2013, Woessner et al., 2015), the Italian INGV-DPC model (MPS working group, 2004; Stucchi et al., 2011) and the Italian Building Code (NTC, 2008). The dotted lines represent the intervals in which the shape was corrected in a deterministic sense (using the GMPEs defined in those intervals) to fill in the missing parts of the spectra. The open circles represent PGA for those GMPEs that don't have the intermediate spectral ordinates.**

An important characteristic in Figure 6.5 is that the present UHS has larger PSA ordinates that those from SHARE or the Italian national PSHA, especially for oscillator periods < 0.4 sec. As shown subsequently through sensitivity analyses, we believe this to be caused by our inclusion of the Lakes fault and subduction interface of the Calabrian arc, which were neglected

in the prior PSHA, as well as differences in the GMPEs. For larger oscillator periods, our UHS ordinates are between those from SHARE (which are lower) and the Italian national PSHA (higher). The uniformly higher results from Italian national PSHA are influenced by the older GMPEs that were used, which as shown in §5.2, predict higher median PSAs than newer models.

The UHS developed in this study can strictly only be defined over the most restrictive range of oscillator periods in the selected GMPEs. This range excludes PSA for $T < 0.05$ sec due to PSA being undefined in this range by the Zhao et al. (2006) GMPE. We approximately define the UHS shape for these periods as follows:

1. We compute the UHS using the complete logic tree (using all the selected GMPEs) for PGA and PSA for $T > 0.05$ sec;
2. We evaluate the controlling scenario for the selected hazard levels using disaggregation (§6.3);
3. We compute deterministic PSA shapes relative to T using the GMPEs that include short-T PSAs (BSSA14, Akkar and Bommer, 2010). This range is $T < 0.05$ sec;
4. The shape from (3) is used to interpolate the UHS between 0.05 sec and 0.01 sec (used to represent PGA). The results of this interpolation are shown with dotted lines in Figure 6.5.

6.3 Disaggregation of the Seismic Hazard

For each seismic source, PSHA accounts for all magnitudes and their relative likelihood of occurring within the defined range of $\mathbf{M}_{min}$ to $\mathbf{M}_{max}$. Moreover, for each source and **M** combination, all possible site-source distances are considered, along with their relative likelihoods, by randomizing the rupture location on the fault. Finally, for each **M** and distance combination, the full distribution of ground motion IMs is considered in accordance with the log mean and standard deviation from the GMPE.

Disaggregation identifies the source, distance, and ground motion percentiles that contribute most strongly to the computed hazard (Bazzurro and Cornell, 1999). Disaggregation results are not unique – they depend on the IM and hazard level considered. For example, UHS ordinates at different periods will in general produce different disaggregation results. OQ disaggregation

classifies relative contributions of different parameter combinations as follows (Pagani et al. 2014b):

1. Magnitude (**M**);
2. Distance to rupture surface-projection (Joyner-Boore distance; R_{jb});
3. Longitude and latitude of rupture surface-projection closest point (longitude, latitude);
4. Tectonic region type (TRT);
5. The percentile of ground motion intensity conditional on **M** and R_{jb}, represented in terms of epsilon (ε) as:

$$\varepsilon = \frac{\ln im - \mu_{\ln}(\mathbf{M}, R_{jb}, V_{S30})}{\sigma_{\ln}(\mathbf{M}, R_{jb}, V_{S30})} \tag{6.2}$$

where *im* is the ground motion intensity at the hazard level for which the disaggregation is computed, and $\mu_{\ln}$ and $\sigma_{\ln}$ are the statistical moments of a GMPE in natural log units, which in general can depend on magnitude, distance, and site condition.

The parameters listed above create a five-dimensional model space (*ms*) that is discretized into a finite number of bins. Each combination of parameters (but with ε omitted) defines a model space bin *ms* = (**M**, R_{jb}, long/lat, TRT) for which the probability of *IM* exceeding level *im* at least once in a time span Δt is computed as (Pagani et al., 2014b):

$$P(IM > im|\Delta t, ms) = 1 - \prod_{i=1}^{I}\prod_{j=1}^{J}\begin{cases} P_{rup_{ij}}(IM < im|\Delta t) & if rup_{ij} \in ms \\ 1 & otherwise \end{cases} \tag{6.3}$$

where *i* is an index for source (associated with a location and **M**) and *j* is an index for rupture location within the source, which sets the distance. The quantity P_{rupij} is the probability of *IM* < *im* in time Δt given that rupture *j* within source *i* has occurred. In other words, it is the probability that this rupture does not produce ground motions that exceed *im*. If the rupture *j* within source *i* has not occurred (the rupture doesn't belong to the *im* bin), then the probability that this rupture does not produce a 'special event' (ground motion that exceed *im*) is equal to 1. As such, Eq. (6.3) considers all possible ε, hence this equation is not used for the ε part of disaggregation. The disaggregated probability from Eq. (6.3) is based on the assumption that earthquake ruptures in different bins are independent, therefore the union of exceedance

probabilities for all ruptures and sources contained within *ms* (left side of Eq. 6.3) can be computed from one minus the product of non-exceedance probabilities.

Although this expression (Eq. 6.3) is not immediately intuitive, consider two overlapping events *A* and *B*. The probability of the union of these events is $P(A \cup B) = P(A) + P(B) - P(A \cap B)$, where $\cap$ indicates the intersection of these events. If *A* and *B* are independent, the intersection probability $P(A \cap B) = P(A) \times P(B)$. This union probability is akin to the left side of Eq. (6.3) in that we want the union of all ruptures and sources that meet the ground motion exceedance requirement. The right side of Eq. (6.3) asserts that $P(A \cup B) = 1 - P\left(\bar{A}\right)P\left(\bar{B}\right)$, where the overbar indicates 'not'. Recognizing that $P\left(\bar{A}\right) = 1 - P\left(A\right)$ and substituting, the original expression for $P(A \cup B)$ is recovered. Hence, Eq. (6.3) correctly represents the union of exceedance probabilities across ruptures and sources.

The OQ disaggregation calculator allows is configured to create several types of disaggregation histograms. We use the following:

- Magnitude disaggregation;
- Distance disaggregation;
- Magnitude-Distance disaggregation;
- Latitude-Longitude disaggregation;
- Magnitude-Distance-Epsilon disaggregation;
- Latitude-Longitude-Magnitude disaggregation.

The disaggregation performed by OQ (Eq. 6.3) is different from classical disaggregation (e.g., Bazzurro and Cornell, 1999). The OQ disaggregation provides, for a given bin *ms*, the conditional probability of (at least one) ground motion exceedance in time span Δt. Classical disaggregation could in principal provide this quantity as well. However, by convention the results are expressed differently. The rates of 'special events' that produce $IM > im$ within model space bins (ms) = ν_{ms} are computed, from which exceedance probabilities are computed. Those exceedance probabilities are then normalized by the corresponding probabilities for the full

parameter space (all *ms*) (rate = ν), which provides a relative contribution (RC) for each *ms* as follows:

$$RC(ms) = \frac{1 - \exp(-\nu_{ms}\Delta t)}{1 - \exp(-\nu\Delta t)} \tag{6.4}$$

The sum of RCs across all *ms* is unity.

The OQ disagreggation results can be readily converted to normalized disaggregation results. Recognize that the numerator in Eq. (6.4) can be re-written as follows based on the properties of a Poisson process:

$$P(IM \geq im|\,\Delta\, t, ms) = 1 - e^{-\nu_{ms}\,\Delta\, t} \tag{6.5}$$

The left side of Eq 6.5 is known from Eq. (6.3), so the numerator in Eq. (6.4) is known.

The denominator in Eq. (6.4) can be similarly written as:

$$P(IM \geq im|\Delta t) = 1 - e^{-\nu\Delta t} \tag{6.6}$$

The left side of Eq. (6.6), $P(IM > im|\Delta t)$, is obtained as one minus the product of non-exceedence probabilities for the different *ms* as:

$$P(IM > im|\Delta t) = 1 - \prod_{ms}\prod\big(1 - P(IM > im|\Delta t, ms)\big) \tag{6.7}$$

By these calculations, the relative contributions in Eq. (6.4) can be obtained.

Using the above approach, classical disaggregation of the complete model for the Farneto del Principe dam site was performed using OQ, for a return period of 2475 years and 0.25 sec PSA. The period T = 0.25 represents the first elastic natural period of the dam plus the deformable foundation.

Figure 6.6 shows the distance disaggregation, which indicates that the hazard is controlled by close sources (R_{jb} less than 35 km). These likely include the Crati valley fault (§4.3) in combination with area and background sources. Since we are using the R_{jb} distance metric for two of the three GMPEs used for the shallow crustal tectonic regime, faults underlying the site, including the nearest area source (ITAS 319) can contribute at zero distance. The subduction zone GMPEs, use the R_{rup} distance metric, for this reason, the subduction sources will not

contribute at distances less than the closest distance to the interface, which is 50 km. The mean and mode distances are 25.5 and 2.5 km (center of first bin), respectively. We recognize that disaggregations associated with specific sources are standard practice in the US, but this capability is not available in OQ.

Figure 6.7 presents the magnitude disaggregation, which shows that there is an important contribution to the hazard from large magnitude events (>7.5). Although OQ does not allow the relative contributions of specific sources to be identified, there are a limited number of options for these large **M** contributions. One contributor is area sources, specifically 318 and 319, which are north of the site and encompassing the site, respectively. Those area sources have largest observed earthquakes of $\mathbf{M}_{obs}$ = 8.0 and 7.8, respectively. Per §4.1, we consider maximum magnitudes as high as $\mathbf{M}_{max}$ = 8.6 and 8.4 for these sources within the logic tree. The second contributor is the subduction interface associated with the Calabrian arc, which has a mean value of $\mathbf{M}_{max}$ = 8.2 (§4.5) (the largest considered magnitude is 8.6 in §6.4, but only the mean value of $\mathbf{M}_{max}$ is considered in the main logic tree). The third contributor is the subduction in-slab area source that is adapted from area source 318 with $\mathbf{M}_{obs}$ = 8.0 and a largest considered $\mathbf{M}_{max}$ in the logic tree of 8.6. Hence, the roughly 5% relative contribution that is shown for the **M** 8.5-9.0 bin is produced by area source 318 (including its use for the subduction in-slab area source). The mean and mode magnitudes are 7.3 and 7.75, respectively. We recognize that the large in-slab earthquakes being treated as area sources with magnitudes above ~ 7.5 is unrealistic; refinements of this element of the fault modeling will be considered in subsequent work.

Figures 6.8 and 6.9 show respectively the latitude-longitude (Lat-Long) and the latitude-longitude-magnitude disaggregation (Lat-Long-**M**). These confirm the essential findings from the distance and **M** disaggregation plots, namely the controlling influence of close distance and large **M** events at this return period.

Figures 6.10 and 6.11 show the magnitude-distance (**M**-R_{jb}) and the magnitude-distance-epsilon (**M**-R_{jb}-ε) disaggregation, respectively. These plots show that events with R_{jb} less than 5 km and **M** = 6-8 control the T_R = 2475 yr hazard 0.25 sec PSA. We expect these are a combination of area source 319 (the area source encompassing the dam site) and the Crati Valley fault (which is the most proximate finite fault source to the dam site). The mean magnitude and distance of $\bar{\mathbf{M}} = 7.4$ and $\overline{R_{jb}} = 26km$ do not correspond to a scenario with a high relative

contribution. Figure 6.11 shows that the epsilon values controlling the hazard are in the range of 2 to 3. These are relatively extreme values of ground motion, higher than is typical in the western US (where controlling epsilons at this return period are typically in the range of 1 to 2).

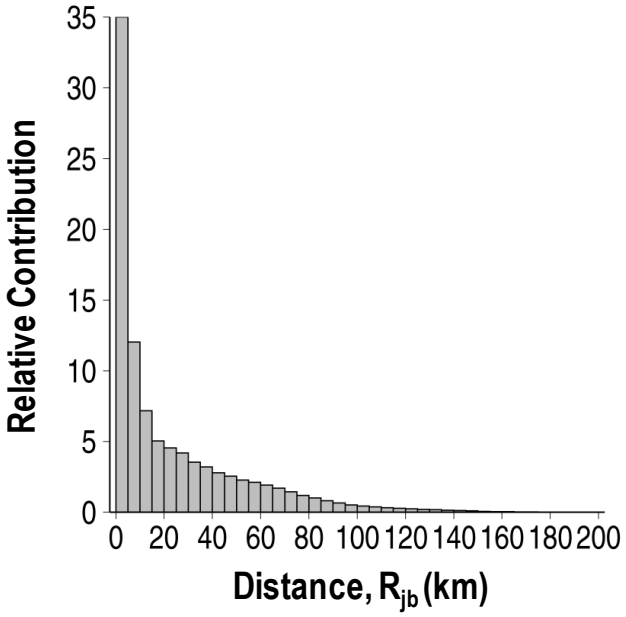

Figure 6.6 **Distance disaggregation for PSA (0.25s) at dam site.**

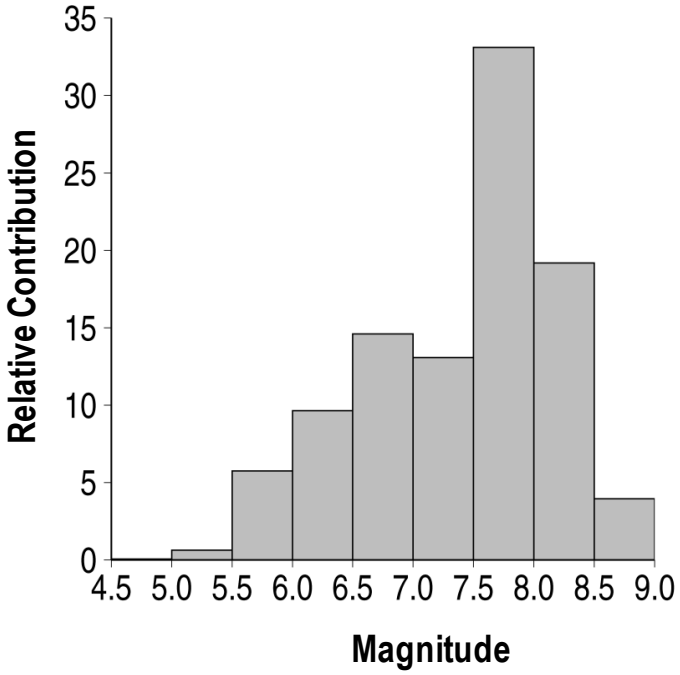

Figure 6.7 **Magnitude disaggregation for PSA (0.25s) at dam site.**

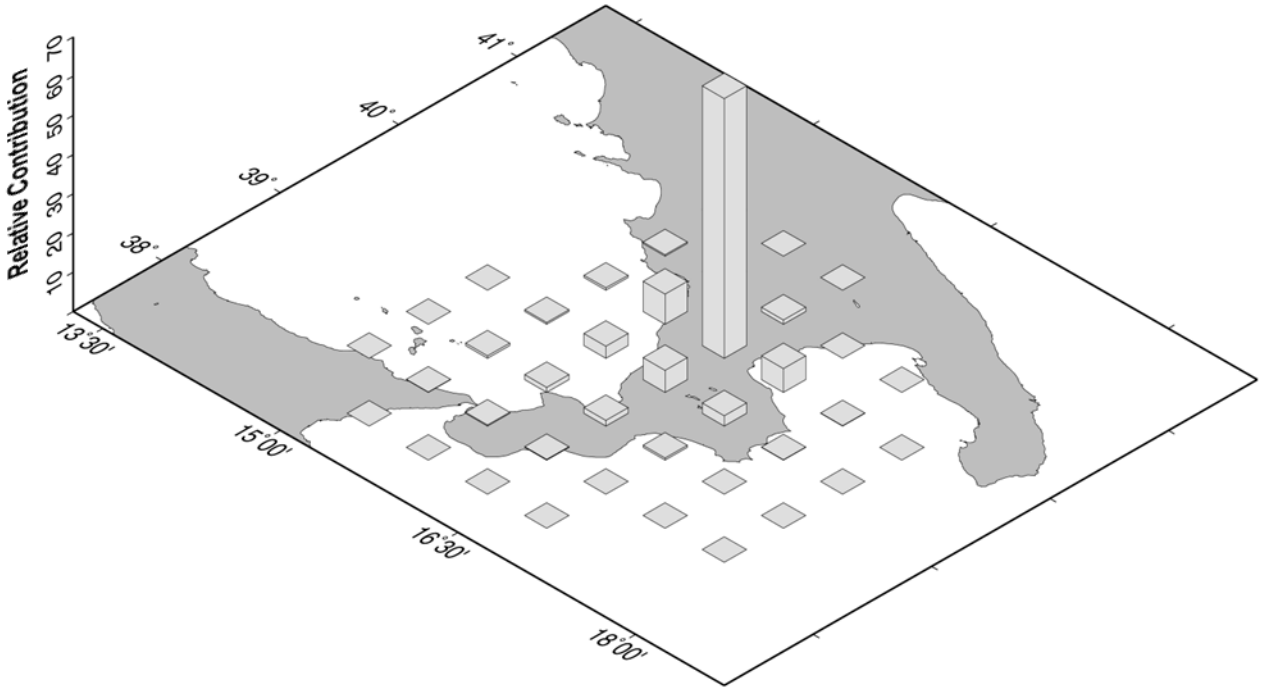

Figure 6.8 **Lat-Long disaggregation for PSA (0.25s) at dam site.**

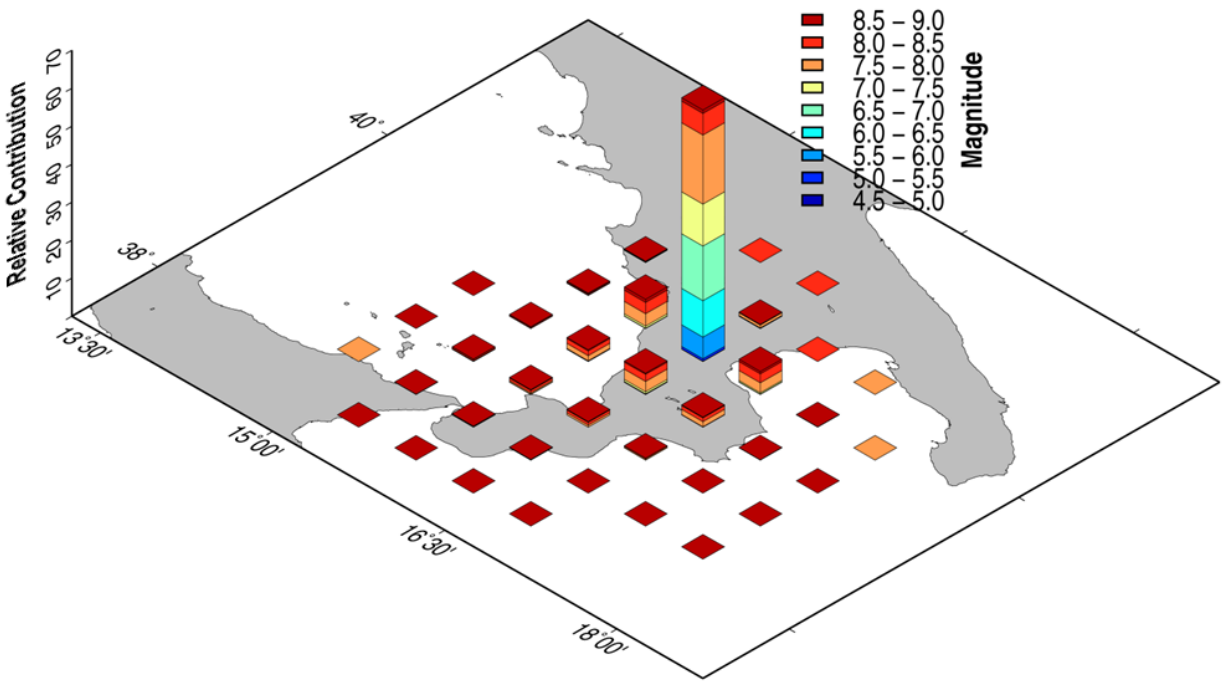

Figure 6.9 **Lat-Long-M disaggregation for PSA (0.25s) at dam site.**

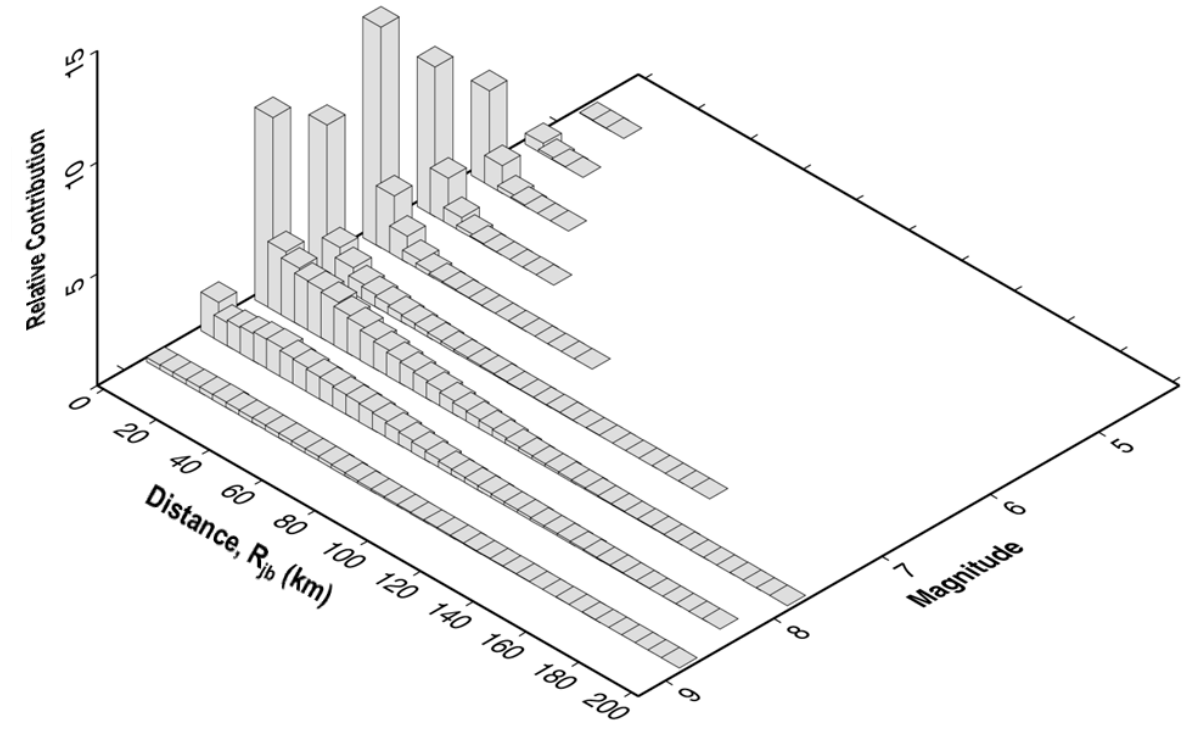

Figure 6.10 M-R_{jb} disaggregation for PSA (0.25s) at dam site.

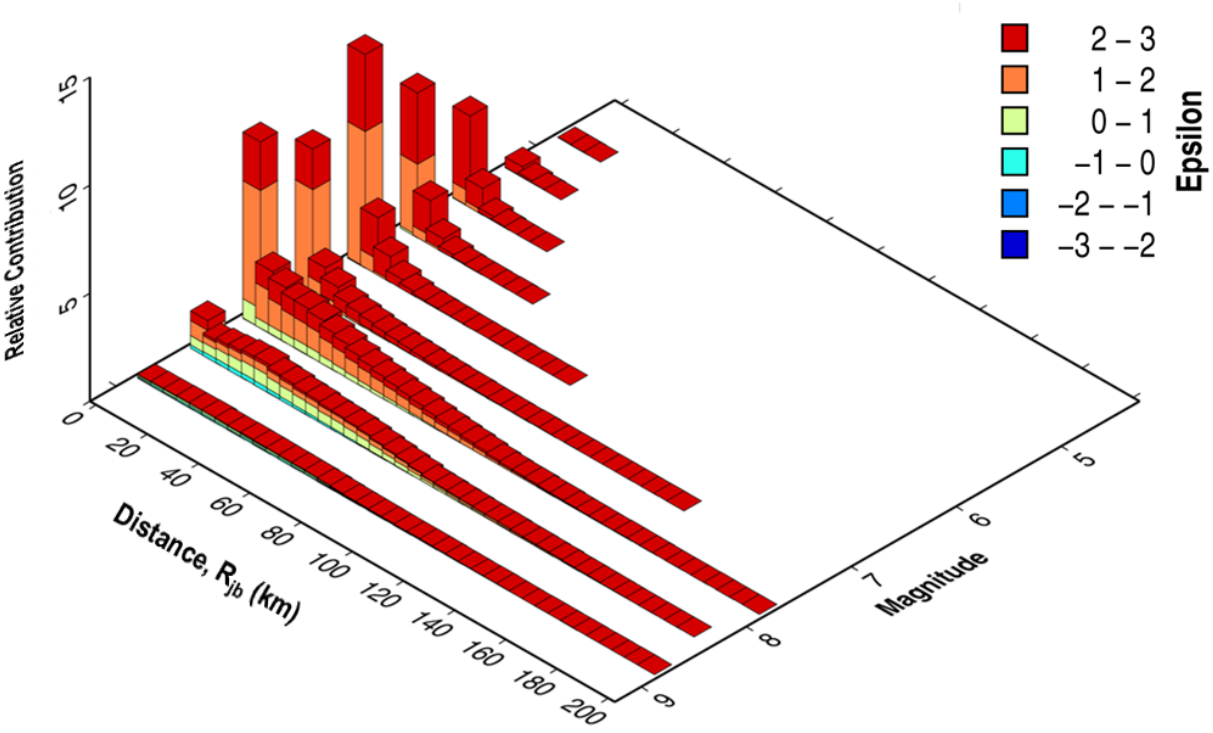

Figure 6.11 M-R_{jb}-ε disaggregation for PSA (0.25s) at dam site.

6.4 Sensitivity Studies

6.4.1 Impact of the Kernel-Smoothed Source Model

In §2.1 the SHARE model was presented. This model contains a Kernel-smoothed source model that is not implemented in this study (the source models used in this study are discussed in §4). We found that for the Farneto del Principe dam site the Kernel-smoothed branch does not significantly affect the hazard computed using the SHARE model. Figure 6.12 shows hazard curves for a range of oscillator periods for the Farneto del Principe dam site using the SHARE model with and without the Kernel-smoothed branches. The differences between the two sets of results are judged to be sufficiently small that the Kernel-smoothed branch can be omitted, although percent differences between the two sets of analyses have not been computed.

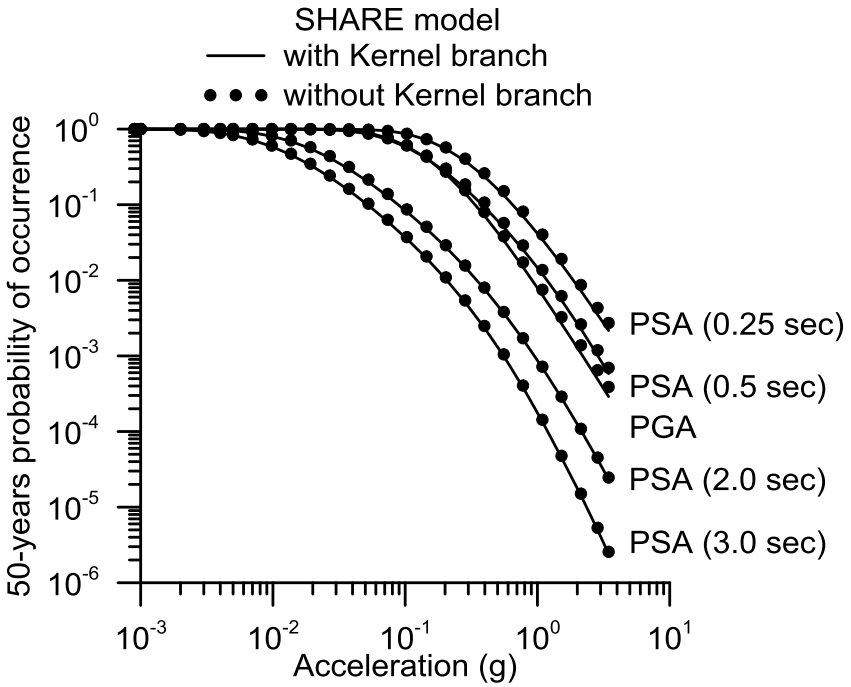

Figure 6.12 **Comparisons of the hazard curves for dam site for Δt = 50 years based on the complete SHARE model and the SHARE model without the kernel-based branch.**

6.4.2 Uncertainty in Maximum Magnitude for Fault Sources

As discussed in §4.2, uncertainty in the maximum magnitude ($\mathbf{M}_{max}$) of fault sources is not included in the main logic tree and hence does not impact the hazard results presented in §6.1-6.3, including the disaggregations. We investigate this source of epistemic uncertainty in this section (for shallow crustal fault sources) and the next (for the subduction interface).

Our approach is based on first order second moment principles (Baker and Cornell 2003; Melchers 1999). We consider mean values of $\mathbf{M}_{max}$ in combination with mean ± √3 times the standard deviation of $\mathbf{M}_{max}$. The weights are assigned as:

- $\mathbf{M}_{max}+\sigma_M\sqrt{3}$; weight: 1/6 (this branch is called $\mathbf{M}_{max}(^{+})$);
- $\mathbf{M}_{max}$; weight: 2/3 (this branch is called $\mathbf{M}_{max}$);
- $\mathbf{M}_{max}$ $-\sigma_M\sqrt{3}$; weight: 1/6 (this branch is called $\mathbf{M}_{max}(^{-})$).

Mean values of $\mathbf{M}_{max}$ are taken from three magnitude-area scaling relationships: Wells and Coppersmith (1994); Hanks and Bakun (2002, 2008), where applicable; Leonard (2010). The standard deviation term σ_M is taken from Wells and Coppersmith (1994).

For faults in which the maximum magnitude $\mathbf{M}_{max}$ is close to 6.4, the branch $\mathbf{M}_{max}(^{-})$, can be lower than 6.4, which per our protocols, would cause the source to be only within the area source branch of source modeling. This issue was managed as follows:

- Model 1: Fault sources + Background zones – the assigned minimum magnitude for fault sources only in the branch $\mathbf{M}_{max}$ $(^{-})$ is 5.5;
- Model 2: Fault sources + Background zones – the assigned minimum magnitude for fault sources in all branches is 5.5;
- Model 3: Fault sources without Background zones – the assigned minimum magnitude for fault sources in all branches is 5.5;
- Model 4: Fault sources without Background zones – the assigned minimum magnitude for fault sources only in the branch $\mathbf{M}_{max}(^{-})$ is 5.5.

In the sensitivity analyses reported in this section, $\mathbf{M}_{max}$ uncertainties are addressed only for the FSBG source model branch of the logic tree shown in Figure 4.1 (area sources are ignored). Hence, the analyses reported here are not meant as a replacement to the general hazard results given in §6.1-6.3. We consider fault sources and background zones for Model 1 and Model 2 and fault sources only for Model 3 and Model 4 (background zones are omitted). Area sources and the subduction interface are omitted in the analyses reported in this section.

Figure 6.13 shows uniform hazard spectra (UHS) computed using a logic tree in which the three branches of $\mathbf{M}_{max}$ given previously are considered. UHS are plotted separately for the four

considered configurations of fault and background sources Model 1-Model 4 along with a case in which $\mathbf{M}_{max}$ is fixed at the mean value. For the case in which $\mathbf{M}_{max}$ is fixed, $\mathbf{M}_{min}$ is taken as 6.4 and background zones are used, which is consist with the implementation in §4.2. The main findings of this analysis are as follows: (1) consideration of M_{max} uncertainties has no appreciable effect on UHS ordinates; (2) the elimination of background sources (Model 3 and Model 4) reduces UHS ordinates by 19-45% approximately at T_R = 475 and 3-20% at T_R = 2475 yr. These results indicate that the analyses reported previously in §6.1-6.3 do not consider an inappropriately low level of epistemic uncertainty as a result of not including logic tree branches with variations in $\mathbf{M}_{max}$. These preliminary results have to be considered preliminary. The conclusions of this analysis should be further verified, by consistently considering an appropriate threshold for $\mathbf{M}_{min}$ in all branches. Furthermore more robust considerations on moment balance are desirable (e.g. G-R *a* values can be recomputed in order to achieve balance between rate of moment build-up and release).

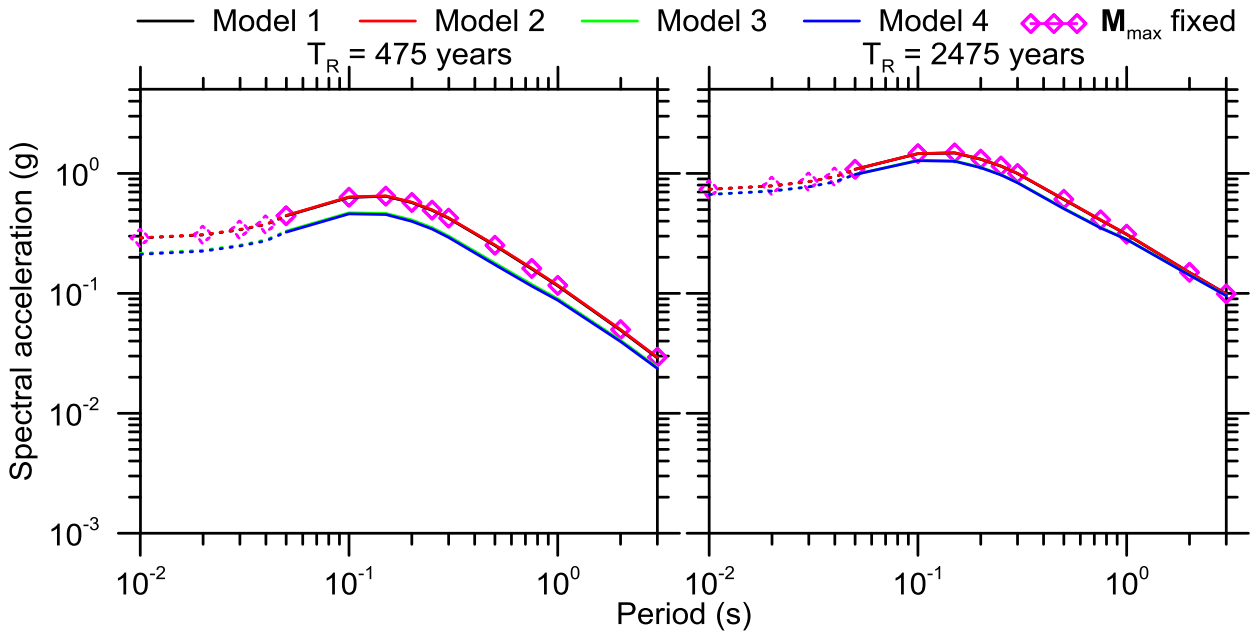

Figure 6.13 **UHS for the Model 1-Model 4 configurations along with a case in which M_{max} is fixed at the mean value. The dotted lines (and symbols) represent the intervals in which the shape was corrected in a deterministic sense (using the GMPEs defined in those intervals) to fill in the missing parts of the spectra.**

Figure 6.14 shows uniform hazard spectra (UHS) for the Model 1 configuration of fault and background sources, for three $\mathbf{M}_{max}$ branches: $\mathbf{M}_{max}(^{+})$, $\mathbf{M}_{max}(^{-})$, $\mathbf{M}_{max}$ fixed at the mean value. The Model 1 configuration includes background zones and uses a minimum magnitude for fault

sources of 5.5. For both return periods, the UHS for $\mathbf{M}_{max}$, $\mathbf{M}_{max}(^{+})$ and $\mathbf{M}_{max}(^{-})$ branches of the logic tree are practically identical. The maximum differences between spectral ordinates in the figure is 1% to 7% for T_R=475 years and 0.5% to 6% for T_R=2475 years. The larger differences come from the larger periods.

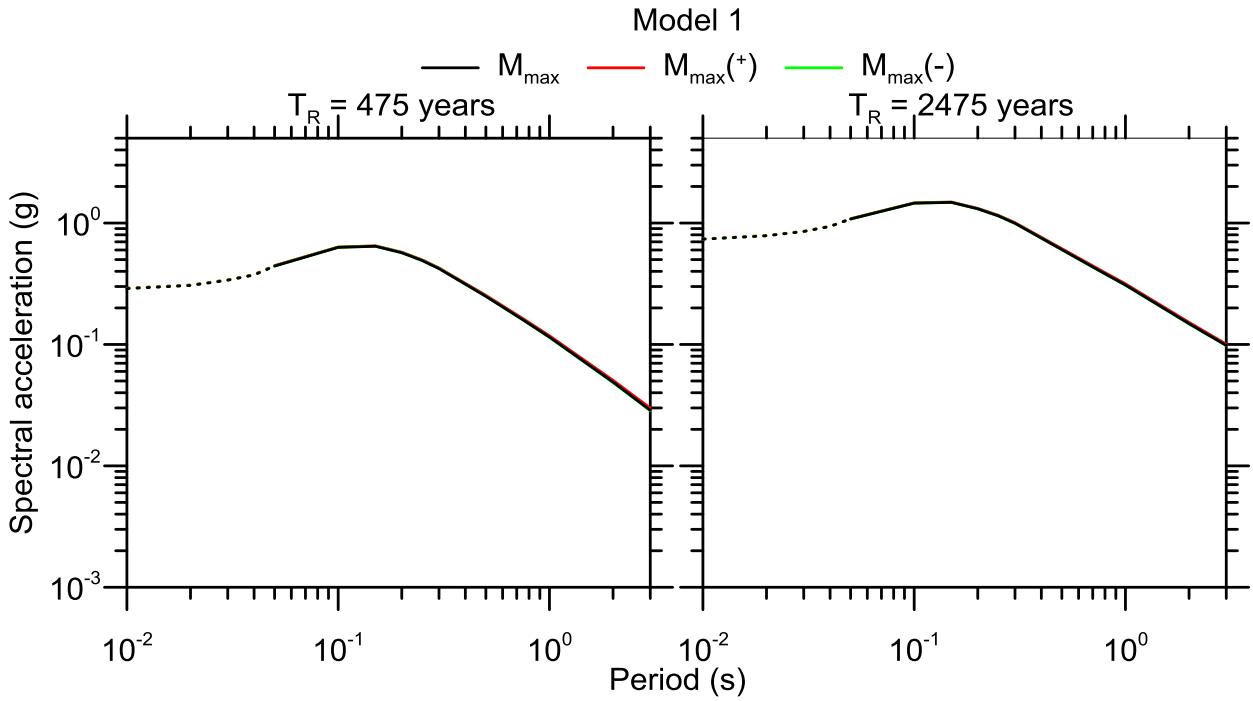

Figure 6.14 **UHS obtained addressing the M_{max} uncertainties for for the Model 1 configuration of fault and background sources, for three M_{max} branches: $M_{max}(^{+})$, $M_{max}(^{-})$, M_{max} fixed at the mean value. The dotted lines (and symbols) represent the intervals in which the shape was corrected in a deterministic sense (using the GMPEs defined in those intervals) to fill in the missing parts of the spectra.**

6.4.3 Uncertainties Related to the Implementation of the Subduction Interface

An important feature introduced in this study is the subduction interface of the Calabrian arc. The main features of the implementation of this source are described in §4.5. The mean value of the maximum magnitude was calculated using the Strasser et al. (2010) magnitude-area and magnitude-length scaling for subduction interface, Equations 6.8 and 6.9:

$$\mathbf{M} = 4.868 + 1.392\log(L) \pm \sigma \quad (6.8)$$

$$\mathbf{M} = 4.441 + 0.846\log(A) \pm \sigma \quad (6.9)$$

where L = 250 km is the rupture length, A = 12500 km^2 is the rupture area, while the associated standard deviations are σ = 0.277 for Eq. (6.8) and σ = 0.286 for Eq. (6.9). The $\mathbf{M}_{max}$ = 8.2 used

for this source is the average of the values obtained by Equations (6.8) and (6.9). The Gutenberg-Richter recurrence relation parameters used (as described in §4.5) are b = 0.9 and a = 3.8 (for the slip rate lower bound, s_{lower}), and b = 0.9 and a = 4.3 (for the slip rate upper bound, s_{upper}).

The $\mathbf{M}_{max}$ uncertainties are treated using the same logic tree approach described in §6.4.2, with the difference that in this case the Area sources (AS model) are included in the analysis. In this case the three branches for the $\mathbf{M}_{max}$ uncertainties are combined with the slip rate lower and the upper bound, resulting in a logic tree made up of six branches:

- $\mathbf{M}_{max}+\sigma\sqrt{3}$; weight: 1/12 ($\mathbf{M}_{max}(^{+})$ + slip rate upper bound (s_{upper}));
- $\mathbf{M}_{max}+\sigma\sqrt{3}$; weight: 1/12 ($\mathbf{M}_{max}(^{+})$ + slip rate lower bound (s_{lower}));
- $\mathbf{M}_{max}$; weight: 1/3 ($\mathbf{M}_{max}$ + slip rate upper bound (s_{upper}));
- $\mathbf{M}_{max}$; weight: 1/3 ($\mathbf{M}_{max}$ + slip rate lower bound (s_{lower}));
- $\mathbf{M}_{max}-\sigma\sqrt{3}$; weight: 1/12 ($\mathbf{M}_{max}(^{-})$+ slip rate upper bound($s_{upper}$));
- $\mathbf{M}_{max}-\sigma\sqrt{3}$; weight: 1/12 ($\mathbf{M}_{max}(^{-})$+ slip rate bound ($s_{lower}$)).

Figure 6.15 shows weighted average uniform hazard spectra (UHS) computed using a logic tree in which the six branches of $\mathbf{M}_{max}$ and slip rate given above are considered. Also shown are results for the case in which the subduction interface is not modeled (marked as 'Without interface') and the case in which $\mathbf{M}_{max}$ was fixed at the mean value (marked as '$\mathbf{M}_{max}$ fixed'). The difference in the UHS for the shorter return period (T_R = 475 years, probability of exceedance equal to 10% in 50 years) is higher than for the longer return period (T_R = 2475 years, probability of exceedance equal to 2% in 50 years). The mean UHS developed by considering uncertainties in maximum magnitude and slip rate is nearly identical to that developed using the mean value of $\mathbf{M}_{max}$. For this reason we used mean values of $\mathbf{M}_{max}$ and slip rate in the final PSHA for the subject site.

Figure 6.16 shows individual UHS for each of the six logic tree branches. The differences in the UHS ordinates are larger for T_R = 475 years than for T_R = 2475 years. The maximum differences between spectral ordinates in the figure is 10% to 34% for T_R=475 years and 5% to 17% for T_R=2475 years. The larger differences come from the larger periods.

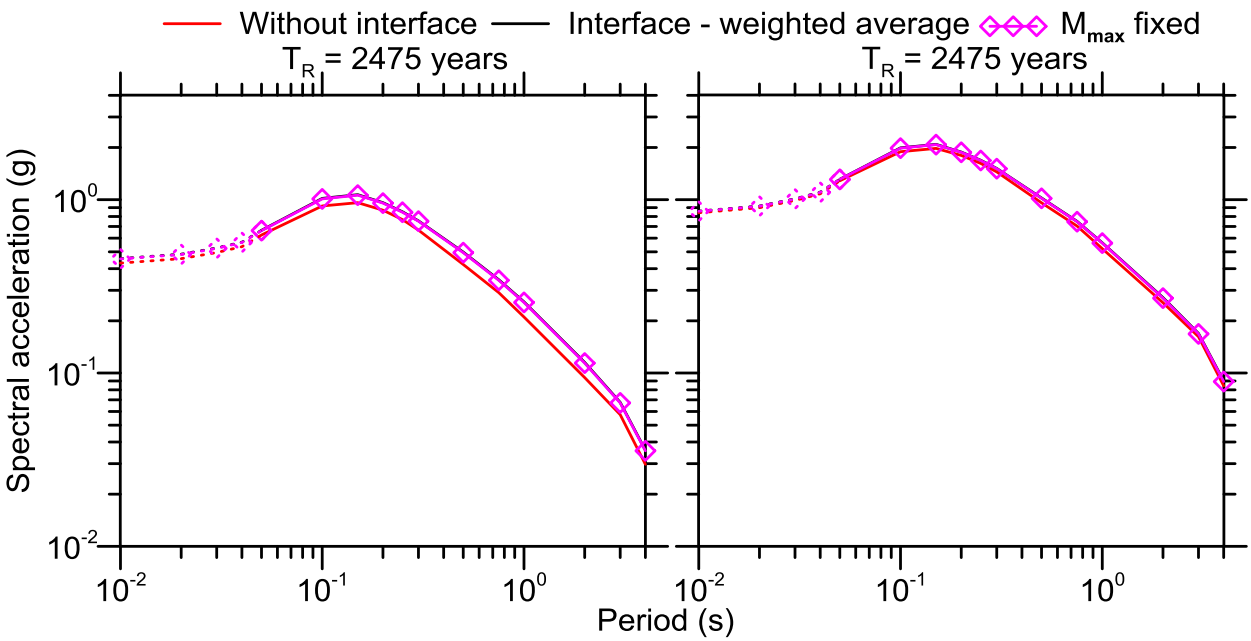

Figure 6.15 **UHS for two cases with the interface: M_{max} fixed at the mean value, weighted average per bulleted list in this section and for the case without the subduction interface, and. The dotted lines represent the intervals in which the shape was corrected in a deterministic sense (using the GMPEs defined in those intervals) to fill in the missing parts of the spectra.**

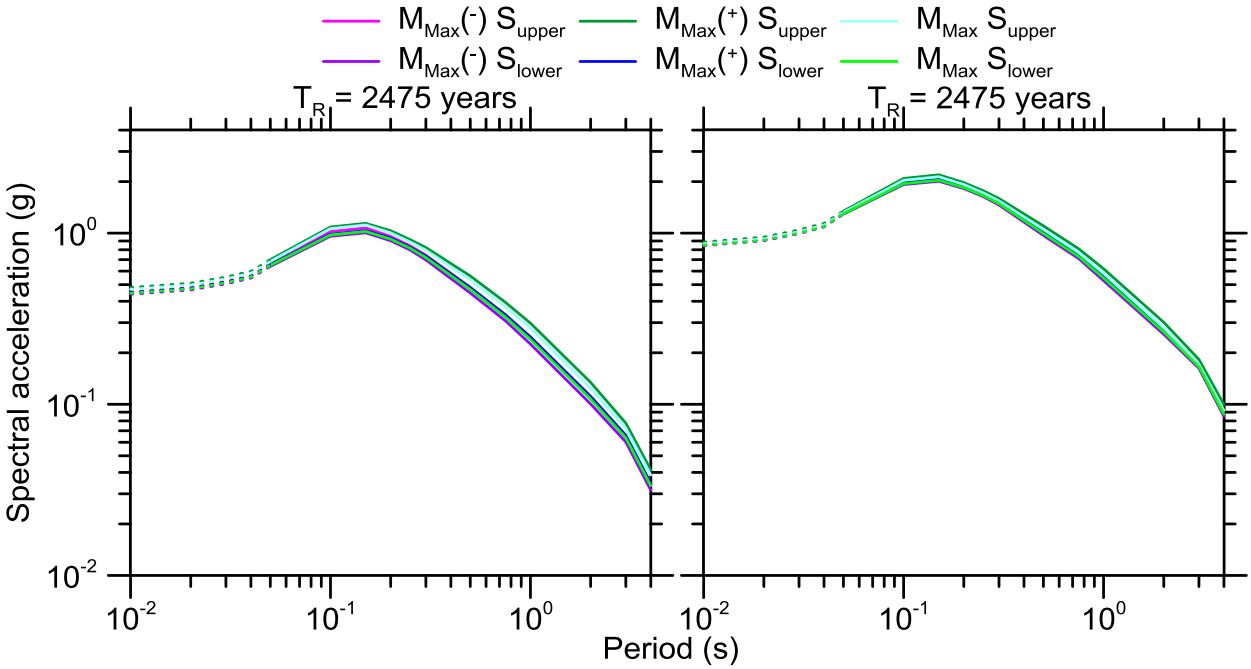

Figure 6.16 **UHS for the six logic tree branches. The dotted lines represent the intervals in which the shape was corrected in a deterministic sense (using the GMPEs defined in those intervals) to fill in the missing parts of the spectra.**

In Figure 6.17, the hazard curves for five different oscillator periods are shown for the cases with and without the interface. The hazard curves were computed for the following oscillator

periods: T = 0 (PGA), 0.25, 0.5, 1 and 2 seconds. In Figure 6.18 the discrepancies between the models with and without the interface, are plotted against spectral ordinate (acceleration). The effect of the subduction interface increase proportionally with increasing oscillator period, until a certain threshold (T = 1s).

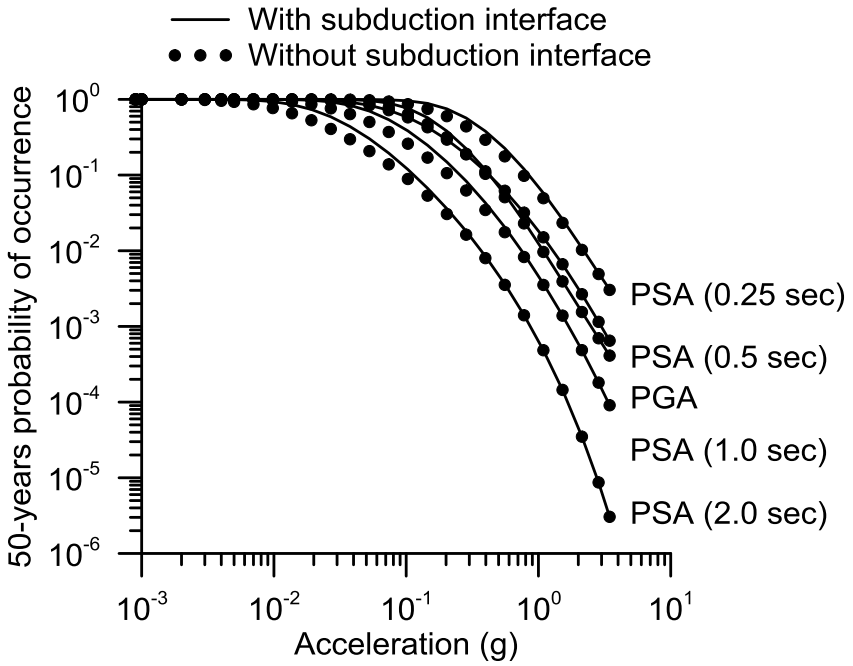

Figure 6.17 Comparison among the hazard curves of the models with and without the subduction (SZ) interface for five structural periods.

6.4.4 Relative Effect of the Different GMPEs

The logic tree for the principle PSHA reported in §6.1-6.3 includes alternate GMPEs as shown in Figure 5.5. In this section, we investigate the sensitivity of mean hazard results to the consideration of different GMPEs. This is done by performing PSHA using each GMPE in isolation with the original source model (as described in §4).

Figure 6.19 compares mean hazard curves for the overall model (originally presented in §6.1) with mean hazard curves using the same source model with a single GMPE for SCRs (the logic tree for SZs was not changed). Five ACR GMPEs were considered for this sensitivity analysis: BSSA14, Bindi et al. (2011), Akkar and Bommer (2010), Faccioli et al. (2010), Zhao et al. (2006).

The results in Figure 6.19 show that the Akkar and Bommer (2010), Zhao et al. (2006) and the BSSA14 models exhibit generally compatible trends. As expected, since these GMPEs were selected to be part of the overall model, their shapes are similar to the curve of the complete (overall) model for all the intensity measures. The Bindi et al. (2011) model tends to give lower accelerations than the overall model for low hazard levels and higher accelerations for high hazard levels. Hazard results predicted by the Faccioli et al. (2010) model often fall below those for the other GMPEs.

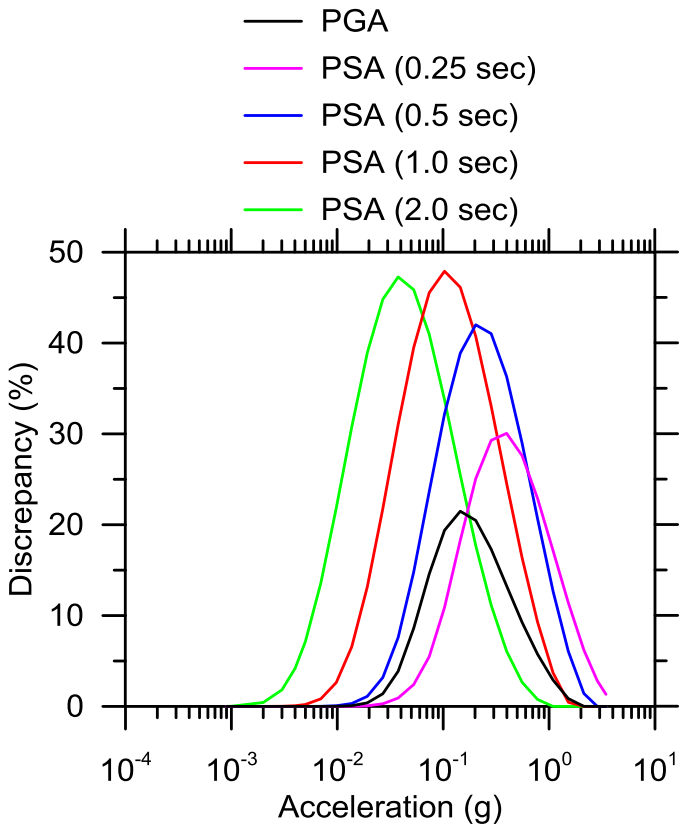

Figure 6.18 Discrepancies between the models with and without the interface, for PGA, PSA (0.25 sec), PSA (0.5 sec), PSA (1.0 sec) and PSA (2.0 sec).

Figure 6.20 compares UHS for the Farneto del Prinicpe dam site between the overall model (this study) and the individual GMPEs. The shape of the spectra from the selected GMPEs are similar; those not selected have some unusual features, especially Faccioli et al. (2010), which has several kinks in the spectrum.

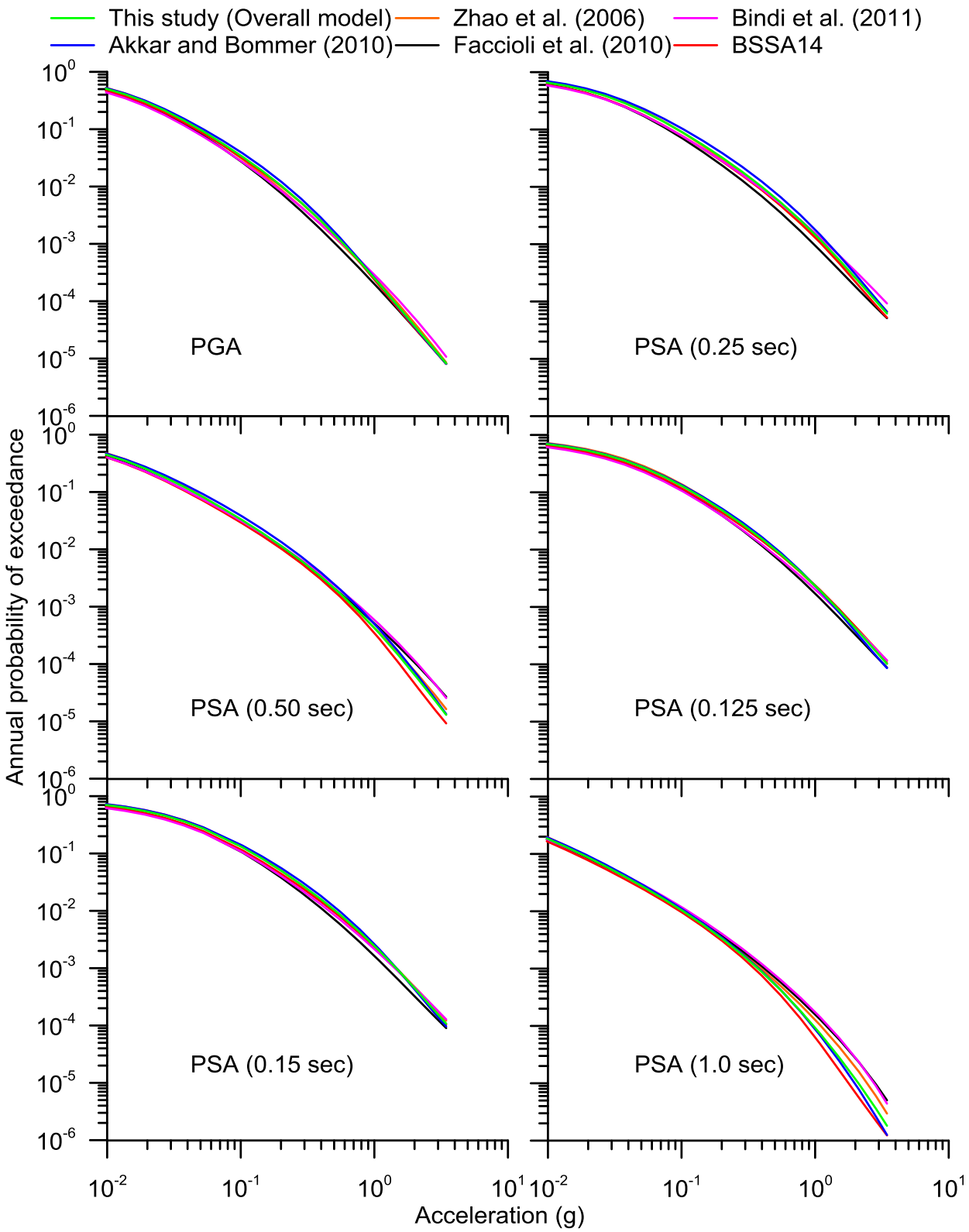

Figure 6.19 **Mean hazard curves for the overall model (this study) and the single GMPEs.**

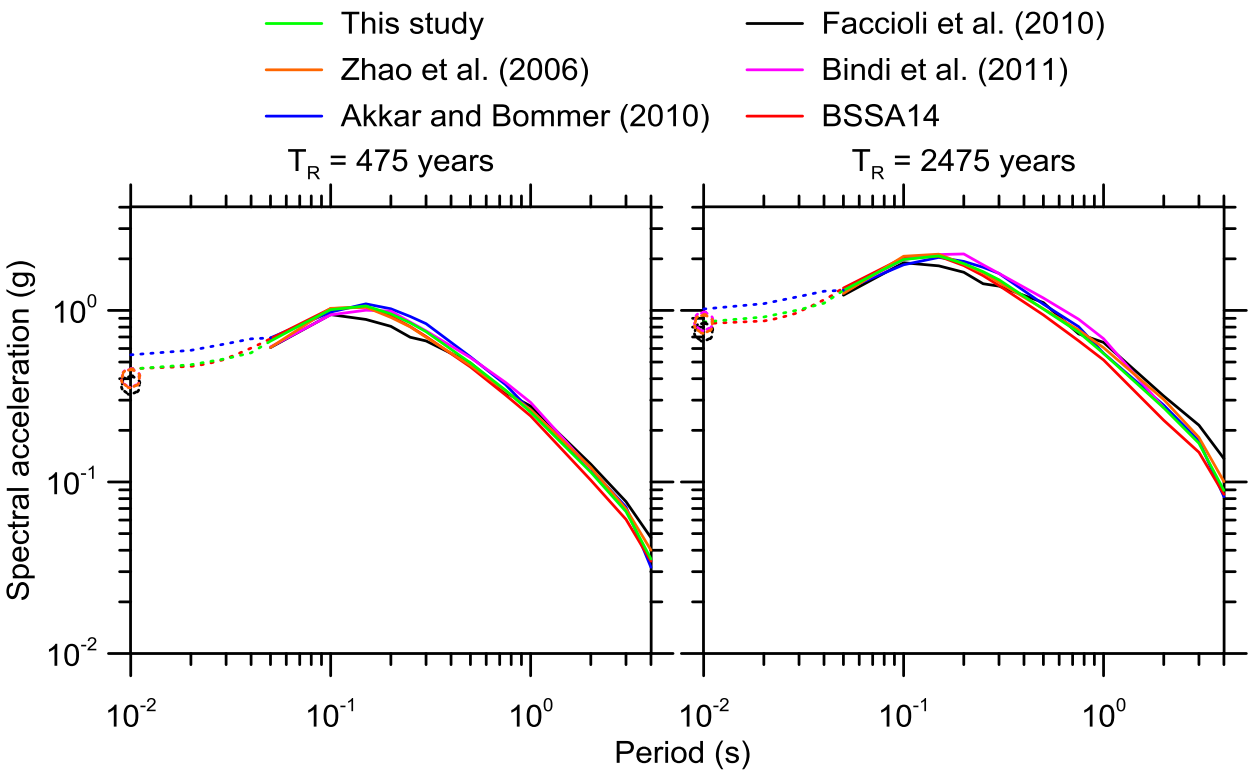

Figure 6.20 **Comparison among the UHS of the complete model (this study) and five different approaches that use one of the pre-selected GMPEs at a time. The dotted lines represent the intervals in which the shape was corrected in a deterministic sense (using the GMPEs defined in those intervals) to fill in the missing parts of the spectra. The open circles represent PGA for those GMPEs that don't have the intermediate spectral ordinates.**

7 Conclusions

We present a site-specific PSHA for a dam site in Calabria that provides a means by which to critically assess seismic hazard analysis procedures generally for the Italian region. We apply SHARE source modeling procedures as given by Woessner et al. (2015) and as implemented for hazard computations in the OpenQuake platform (Pagani et al., 2014a). We identify several concerns, mostly related to the assignment of maximum magnitudes. Specifically, area source maximum magnitudes reflect arbitrary adjustments that significantly affect moment release, without considering moment balance. For fault sources in active crustal regions, we are concerned with: (1) the deliberate biasing above the mean of magnitudes derived from magnitude-area (or similar magnitude-length) scaling relations and (2) the use of source dimensions that are biased below those for the actual fault when the fault aspect ratio (length/width) exceeds three.

We depart from most past practice in Italy in the selection of ground motion prediction equations (GMPEs) for the PSHA. Whereas the PSHA for Italian building code maps and most Italian site-specific studies we have found in the literature utilize regional, national, or even more-localized models, we instead consider models based on much larger data sets. Our rationale for this approach is that regional models tend to be poorly constrained in the range of magnitudes and distances that control seismic hazard for engineering application. Instead we apply a combination of models selected for global application in the Global Earthquake Model and a more recent global model that includes an Italy-specific distance attenuation function. We recognize the arguments made to justify past use of relatively local GMPEs despite their limited data sets, which is that they may better reflect the effects of local conditions affecting source, path, and site effects. This may be true in the parameter space of the database used to develop the models, but we argue it does not apply outside of that space (large magnitude, close distance), which are the conditions that dominate hazard for engineering applications. We suggest that

these local effects are best accounted for using non-ergodic analyses that consider local path and site effects using site-specific recordings, not through the use of local (but still ergodic) GMPEs.

As a result of our changes to the source models and GMPEs, computed ground motions for the subject site at the 2475 year return period (hazard level) exceed those from the SHARE model by amounts ranging from 10-15% at short periods (< 0.5 sec) to ~ 5% at 1.0 sec PSA. Interestingly, changes to the maximum magnitudes used in the fault models negligibly impact the hazard. The modest sensitivity to fault source parameters results from the dominant influence of area source models, which cause the hazard to be dominated by zero-distance (in a Joyner-Boore sense) earthquakes that are not associated with any known source. This outcome, which is common when area source models are applied, raises the practical question of whether such models should be allowed to exert such a dominant influence, especially for regions (such as that for the dam site) with numerous known faults that dominate the observed regional seismicity. While down-weighting of area source models could be considered for such areas, an approach of that sort would comprise a transformational shift from decades of past practice in Italy. We believe such a step would be most effectively considered through a consensus building process among an expert panel, and did not include such analyses for this site.

REFERENCES

Abrahamson N.A., Gregor N., and Addo K. (2015). BC Hydro ground motion prediction equations for subduction earthquakes, *Earthq. Spectra*, In-Press, http://dx.doi.org/10.1193/051712EQS188MR.

Aki K., and Richards P.G. (2002) Quantitative Seismology, 2nd edition, *University Science Books*, Sausalito, CA.

Akinci A., Galadini F., Pantosti D., Petersen M., Malagnini L., and Perkins D. (2009). Effect of time dependence on probabilistic seismic-hazard maps and deaggregation for the central apennines, Italy, *Bull. Seismol. Soc. Am.* 99: 585–610.

Akkar S., and Bommer J.J. (2010) Empirical equations for the prediction of PGA, PGV and spectra accelerations in Europe, the Mediterranean region and the Middle East, *Seismol. Res. Lett.*, 81: 195-206.

Ambraseys N.N., Simpson K.A., and Bommer J.J. (1996) Prediction of horizontal response spectra in Europe, *Earthq. Eng. Struct. Dynam.*, 25: 371–400.

Anderson H.A., and Jackson J.A. (1987) The deep seismicity of the Tyrrhenian Sea, *Geophys. J. R. Astron. Soc.*, 91: 613-637.

Anderson J.G., and Luco J.E. (1983) Consequences of slip rate constraints on earthquake recurrence relations, *Bull. Seismol. Soc. Am.*, 73: 471-496.

Angelica C., Bonforte A., Distefano G., Serpelloni E., and Gresta S. (2013) Seismic potential in Italy from integration and comparison of seismic and geodetic strain rates, *Tectonophysics* 608: 996–1006.

Atkinson G.M., and Boore D.M. (2003) Empirical ground-motion relations for subduction zone earthquakes and their application to Cascadia and other regions, *Bull. Seismol. Soc. Am*, 93: 1703-1729.

Baker J.W., and Cornell C.A. (2003) Uncertainty Specification and Propagation for Loss Estimation Using FOSM Methods, *PEER Report 2003/07*. Pacific Earthquake Engineering Research Center, Berkeley, CA.

Basili R., Kastelic V., Demircioglu M.B., Garcia Moreno D., Nemser E.S., Petricca P., Sboras S. P., Besana-Ostman G.M., Cabral J., Camelbeeck T., Caputo R., Danciu L., Domac H.,

Fonseca J., García-Mayordomo J., Giardini D., Glavatovic B., Gulen L., Ince Y., Pavlides S., Sesetyan K., Tarabusi G., Tiberti M. M., Utkucu M., Valensise G., Vanneste K., Vilanova S., and Wössner J. (2013). The European Database of Seismogenic Faults (EDSF) compiled in the framework of the Project SHARE. http://diss.rm.ingv.it/share-edsf/ (last accessed October 2015).

Basili R., Kastelic V., Valensise G., and DISS Working Group 2009 (2009) DISS3 tutorial series: Guidelines for compiling records of the Database of Individual Seismogenic Sources, version 3. *Rapporti Tecnici INGV*, 108.

Basili R., Valensise G., Vannoli P., Burrato P., Fracassi U., Mariano S., Tiberti M.M., and Boschi E. (2008) The Database of Individual Seismogenic Sources (DISS), version 3: Summarizing 20 years of research on Italy's earthquake geology. *Tectonophysics*, 453: 20–43.

Bazzurro P., and Cornell C.A. (1999) Disaggregation of seismic hazard, *Bull. Seismol. Soc. Am.*, 89: 501-520.

Bindi D., Pacor F., Luzi L., Puglia R., Massa M., Ameri G., and Paolucci R. (2011). Ground motion prediction equations derived from the Italian strong motion database, *Bull. Earthquake Eng.*, 9: 1899-1920.

Bommer J.J, Coppersmith K.J., Coppersmith R.T., Hanson K.L., Mangongolo A., Neveling J., Rathje E.M., Rodriguez-Marek A., Scherbaum F., Shelembe R., Stafford P.J., and Strasser F.O. (2015). A SSHAC Level 3 probabilistic seismic hazard analysis for a new-build nuclear site in South Africa, *Earthq. Spectra*, 31: 661-698.

Bommer J.J., Douglas J., and Strasser F.O. (2003). Style-of-faulting in ground-motion prediction equations, *Bull. Earthquake Eng.*, 1: 171–203.

Boore D.M., Stewart J.P., Seyhan E., and Atkinson G.M. (2014). NGA-West 2 equations for predicting PGA, PGV, and 5%-damped PSA for shallow crustal earthquakes, *Earthq. Spectra*, 30: 1057-1085.

Bozorgnia Y., and other 31 authors (2014). NGA-West2 Research Project, *Earthq. Spectra* 30, 973-987.

Brozzetti F., Cirillo D., Liberi F., Faraca E., and Piluso E. (2012). The Crati Valley Extensional System: field and subsurface evidences, *Rendicont. Online Soc. Geol. Ital.*, 21: 159-161.

Bungum H. (2007). Numerical modelling of fault activities, *Comput. Geosci.*, 33: 808–820.

Butler L., Crowley H., Henshaw P., Monelli D., Nastasi M., Panseri L., Pagani M., Silva V., Simionato M., Viganò D., Weatherill G., and Wiss B. (2014). Openquake engine: users instruction manual V.1.0.0.

Calais E., DeMets C., and Nocquet J.M. (2003). Evidence for a post-3.16 Ma change in Nubia-Eurasia plate motion, *Earth Planet. Sci. Lett.*, 216: 81– 92.

Carobene L., and Damiani A.V. (1985). Tettonica e sedimentazione pleistocenica nella media valle del fiume Crati. Area tra il torrente Pescara ed il fiume Mucone (Calabria), *Boll. Soc. Geol. Ital.*, 104: 115–127. In Italian.

Cauzzi C., and Faccioli E. (2008). Broadband (0:05 to 20 s) prediction of displacement response spectra based on worldwide digital records, *Journal of Seismology*, 12: 453-475.

Chiarabba C., Jovane L., and DiStefano R. (2005). A new view of Italian seismicity using 20 years of instrumental recordings, *Tectonophysics*, 395: 251–268.

Chiou B.S.-J., and Youngs R.R. (2008a). An NGA model for the average horizontal component of peak ground motion and response spectra, *Earthq. Spectra*, 24: 173–216.

Chiou B.S.-J., and Youngs R.R., (2008b). NGA model for the average horizontal component of peak ground motion and response spectra, *PEER Report No. 2008/09*, Pacific Earthquake Engineering Research Center, University of California, Berkeley.

Chiou B.S.-J., Darragh R., Gregor N., and Silva W. (2008). NGA Project Strong-Motion Database, *Earthq. Spectra*, 24: 23-44.

Cornell C.A. (1968) Engineering Seismic Risk Analysis, *Bull. Seismol. Soc. Am.*, 58: 1583-1606.

CPTI Working Group (1999). Catalogo Parametrico dei Terremoti Italiani, versione 1 (CPTI99), *INGV, Milano*. http://emidius.mi.ingv.it/CPTI99/ (last accessed October 2015). In Italian.

CPTI Working Group (2004). Catalogo Parametrico dei Terremoti Italiani, version 2004 (CPTI04), *INGV, Milano*. http://emidius.mi.ingv.it/CPTI04/ (last accessed Octobver 2015). In Italian.

D'Agostino N., and Selvaggi, G. (2004). Crustal motion along the Eurasia– Nubia plate boundary in the Calabrian Arc and Sicily and active extension in the Messina Straits from GPS measurements, *J. Geophys. Res.*, 109: B11402.

D'Agostino N., Avallone A., Cheloni D., D'Anastasio E., Mantenuto S., and Selvaggi G. (2008). Active tectonics of the Adriatic region from GPS and earthquake slip vectors, *J. Geophys. Res.*, 113: B12413.

D'Agostino N., D'Anastasio E., Gervasi A., Guerra I., Nedimovic M.R., Seeber L., and Steckler M. (2011). Forearc extension and slow rollback of the Calabrian Arc from GPS measurements, *Geophys. Res. Lett.*, 38.

Danciu L., Woessner J., Giardini D., and SHARE Consortium (2013). A community-based Probabilistic Seismic Hazard Maps for the Euro-Mediterranean Region, *Proc. of Congress on Recent Advances in Earthquake Engineering and Structural Dynamics*, Vienna, Austria, 28-30 August.

De Natale G., Faccioli E., and Zollo A. (1988) Scaling of peak ground motion from digital recordings of small earthquakes at Campi Flegrei, southern Italy, *Pure Appl. Geophys.*, 128: 37–53.

de Voogd B., Truffert C., Chamot-Rooke N., Huchon P., Lallemant S., and Le Pichon X. (1992). Two-ship deep seismic soundings in the basins of the eastern Mediterranean Sea (Pasiphae cruise), *Geophys. J. Int.*, 109: 536–552.

Decreto Ministeriale, D.M. June 14 (2014). Norme tecniche per la progettazione e la costruzione degli sbarramenti di ritenuta (dighe e traverse). In Italian.

Delavaud E., Cotton F., Akkar S., Scherbaum F., Danciu L., Beauval C., Drouet S., Douglas J., Basili R., Sandikkaya M.A., Segou M., Faccioli E., and Theodoulidis N. (2012). Toward a Ground-Motion Logic Tree for Probabilistic Seismic Hazard Assessment in Europe, Journal of Seismology., 16: 451–473.

Devoti R., Riguzzi F., CuffaroM., and Doglioni C. (2008). New GPS constraints on the kinematics of the Apennines subduction, *Earth Planet. Sci. Lett.*, 273: 163-174.

Douglas J. (2015). Ground motion prediction equations 1964–2014, Website http://www.gmpe.org.uk. (last accessed August 2015).

Faccenna C., Funiciello F., Giardini D., and Lucente P. (2001). Episodic back-arc extension during restricted mantle convection in the central Mediterranean, *Earth Planet. Sci. Lett.*, 187: 105–116.

Faccenna C., Piromallo C. Crespo-Blanc A. Jolivet L., and Rossetti F. (2004) Lateral slab deformation and the origin of the western Mediterranean arcs, *Tectonics*, 23: TC1012.

Faccioli E., and Villani M. (2009). Seismic hazard mapping for Italy in terms of broadband displacement response spectra, *Earthq. Spectra* 25: 515–539.

Faccioli E., Bianchini A., and Villani M. (2010). New ground motion prediction equations for T > 1 s and their influence on seismic hazard assessment, *Proc. of the University of Tokyo Symposium on Long-Period Ground Motion and Urban Disaster Mitigation*, Tokyo, Japan, 17-18 March.

Faccioli E., Paolucci R., and Vanini M. (2015). Evaluation of probabilistic site-specific seismic-hazard methods and associated uncertainties, with applications in the Po Plain, northern Italy. *Bull. Seismol. Soc. Am.*, 105: 2787-2807.

Field E., and other 19 authors (2014). Uniform California Earthquake Rupture Forecast, version 3 (UCERF3) - The time-independent model. *Bull. Seismol. Soc. Am.* 104: 1122-1180.

Field E.H., Jordan T.H., and Cornell C.A. (2003). OpenSHA - A developing Community-Modeling Environment for Seismic Hazard Analysis, *Seismol. Res. Lett.*, 74: 406–419.

Galli P., and Bosi V. (2003). Catastrophic 1638 earthquakes in Calabria (southern Italy). New insight from paleoseismological investigation. *J. Geophys. Res.*, 108: ETG 1-1–ETG 1-20.

Galli P., Scionti V., and Spina V. (2004). New paleoseismic data from the Lakes and Serre faults (Calabria), *Proc. of the 23rd Convegno Nazionale gruppo nazionale di geofisica della terra solida*, Rome, Italy, 14-16 December.

Galli P., Scionti V., and Spina V. (2007). New paleoseismic data from the Lakes and Serre faults: seismotectonic implications for Calabria (Southern Italy), *Boll. Soc. Geol. It.*, 126(2): 347-364.

Gasperini P., Camassi R., Mirto C., Stucchi M., Azzaro R., Bernardini F., Chiarabba F., Ercolani E., Leschiutta I., Meletti C., and Selvaggi G. (2004). Catalogo dei terremoti CPTI2. *App.1, Rapporto conclusivo della redazione della mappa di pericolosità sismica prevista dall'Ordinanza PCM 3274 del 20 marzo 2003*. http://zonesismiche.mi.ingv.it (last accessed October 2015). In Italian.

GeoPentech (2015). Southwestern United States ground motion characterization SSHAC level 3 – *Technical report Rev.2*.

Giardini D., and Velona` M. (1991). Deep siesmicity of the Tyrrhenian Sea, *Terra Nova*, 3: 57–64.

Giardini D., Woessner J., Danciu L., Crowley H., Cotton F., Grünthal G., Pinho R., Valensise G., Akkar S., Arvidsson R., Basili R., Cameelbeeck T., Campos-Costa A., Douglas J., Demircioglu M.B., Erdik M., Fonseca J., Glavatovic B., Lindholm C., Makropoulos K.,

Meletti C., Musson R., Pitilakis K., Sesetyan K., Stromeyer D., Stucchi M., and Rovida A. (2013). Seismic Hazard Harmonization in Europe (SHARE): Online Data Resource. www.efehr.org (last accessed October 2015).

Goulet C.A., and J.P. Stewart (2009). Pitfalls of deterministic application of nonlinear site factors in probabilistic assessment of ground motions *Earthq. Spectra* 25: 541–555.

Grünthal G., Wahlström R., and Stromeyer D. (2013). The SHARE European Earthquake Catalogue (SHEEC) for the time period 1900–2006 and its comparison to the European-Mediterranean Earthquake Catalogue (EMEC). *Journal of Seismology*, 17(4): 1339-1344

Gutscher M., Roger J., Baptista M., Miranda J., and Tinti S. (2006). Source of the 1693 Catania earthquake and tsunami (southern Italy): new evidence from tsunami modeling of a locked subduction fault plane, *Geophys. Res. Lett.*, 33.

Gvirtzman Z., and Nur A. (2001). Residual topography, lithospheric thickness, and sunken slabs in the central Mediterranean, *Earth Planet. Sci. Lett.*, 187: 117-130.

Hanks T.C., and Kanamori H. (1979). A moment magnitude scale, *J. Geophys. Res.*, 84: 2348-2350.

Hanks, T.C., and Bakun W.H. (2008). M - log A Observations for recent large earthquakes, *Bull. Seismol. Soc. Am.*, 98: 490–494.

Hanks, T.C., and Bakun W.H. (2002). A bilinear source-scaling model for M - log A observations of continental earthquakes, *Bull. Seismol. Soc. Am.*, 92: 1841–1846.

Hiemer S., Jackson D., Qi Wang, Kagan Y.Y., Woessner J., Zechar J., and Wiemer S. (2013). A stochastic forecast of California earthquakes based on fault slip and smoothed seismicity, *Bull. Seismol. Soc. Am.*, 103: 799–810.

Hiemer S., Woessner J., Basili R., Danciu L., Giardini D., and Wiemer S. (2014). A smoothed stochastic earthquake rate model considering seismicity and fault moment release for Europe, *Geophys. J. Int.*, 198: 1159–1172.

Joyner W.B., and Boore D.M. (1981). Peak horizontal acceleration and velocity from strong motion records including records from the 1979 Imperial Valley, California, earthquake, *Bull. Seism. Soc. Am.*, 71: 2011-2038.

Kagan Y.Y. (2002). Aftershock zone scaling, *Bull. Seismol. Soc. Am.*, 92: 641–655.

Leonard (2010) Earthquake Fault Scaling: Self-Consistent Relating of Rupture Length, Width, Average Displacement, and Moment Release, *Bull. Seismol. Soc. Am.*, 100(5A): 1971–1988.

Kaklamanos, J., Baise L.G., and Boore D.M. (2011). Estimating unknown input parameters when implementing the NGA ground-motion prediction equations in engineering practice, *Earthq. Spectra*, 27: 1219–1235.

Lin P.S., Chiou B.S.-J., Abrahamson N.A., Walling M., Lee C.T., and Cheng C.T. (2011). Repeatable source, site, and path effects on the standard deviation for ground-motion prediction, *Bull. Seismol. Soc. Am.*, 101: 2281–2295.

Lolli B., Gasperini P., and Vannucci G. (2014). Empirical conversion between teleseismic magnitudes (m_b and M_s) and moment magnitude (M_w) at the Global, Euro-Mediterranean and Italian scale, *Geophys. J. Int.*, 199: 805-828

Mai P.M., Spudich P., and Boatwright J. (2005). Hypocenter locations in finite-source rupture models, *Bull. Seismol. Soc. Am.*, 95: 965–980.

Malagnini L., Akinci A., Herrmann R.B., Pino N.A., and Scognamiglio L. (2002). Characteristics of the ground motion in northeastern Italy, *Bull. Seismol. Soc. Am.*, 92: 2186–2204.

Malagnini L., Herrmann R.B., and Di Bona M. (2000). Ground motion scaling in the Apennines (Italy), *Bull. Seismol. Soc. Am.*, 90: 1062–1081.

Mastrolembo Ventura B. (2012). Kinematics of the Sicily and Calabria subduction system from elastic block modeling of GPS data, *Ph.D. Thesis*, Università di Bologna.

Mattei M., Cifelli F., and D'Agostino N. (2007). The evolution of the Calabrian Arc: Evidence from paleomagnetic and GPS observations, *Earth Planet. Sci. Lett.*, 263: 259–274.

McGuire A.K., Cornell C.A., and Toro G. (2005). The Case for Using Mean Seismic Hazard, *Earthq. Spectra*, 21: 879-886.

McGuire R.K. (2004). Seismic Hazard and Risk Analysis, *Earthquake Engineering Research Institute (EERI)*, Oakland, California.

Melchers R.E. (1999). Structural Reliability Analysis and Prediction, *John Wiley and Sons*, Chichester. U.K.

Meletti C, Galadini F, Valensise G, Stucchi M, Basili R, Barba G, Vannucci G, and Boschi E (2008). A seismic source model for the seismic hazard assessment of the Italian territory, *Tectonophysics*, 450:85–108.

Meletti C., and Valensise G. (2004). Zonazione sismogenetica ZS9 – App.2 al Rapporto Conclusivo. Gruppo di Lavoro MPS (2004). Redazione della mappa di pericolosità sismica

prevista dall'Ordinanza PCM 3274 del 20 marzo 2003, *Rapporto Conclusivo per il Dipartimento della Protezione Civile, INGV, Milano-Roma.* In Italian.

Minelli L., and C. Faccenna (2010). Evolution of the Calabrian accretionary wedge (central Mediterranean), *Tectonics*, 29.

Molin P., Pazzaglia F., and Dramis F. (2004). Geomorphic expression of active tectonics in a rapidly-deforming arc, Sila Massif, Calabria, southern Italy, *Am. J. Sci.*, 304: 559–589.

Monaco C., and Tortorici L. (2000). Active faulting in the Calabrian Arc and eastern Sicily, *J. Geodyn.*, 29: 407–424.

Montaldo V., Faccioli E., Zonno G., Akinci A., and Malagnini L. (2005). Treatment of ground-motion predictive relationships for the reference seismic hazard map of Italy, *Journal of Seismology*, 9: 295–316.

Morasca, P., Malagnini L., Akinci A., Spallarossa D., and Herrmann R.B. (2006). Ground motion scaling in the western Alps, *Journal of Seismology*, 10: 315-333.

MPS working group (2004). Redazione della mappa di pericolosità sismica prevista dall'Ordinanza PCM del 20 marzo 2003 n. 3274, *All. 1. Rapporto conclusivo per il Dipartimento della Protezione Civile, Istituto Nazionale di Geofisica e Vulcanologia (INGV), Milano-Roma, Italy*, http://zonesismiche.mi.ingv.it/ (last accessed October 2015). In Italian.

Musson R.M.W. (2000). The use of Monte Carlo simulations for seismic hazard assessment in the U.K., *Annals of Geophys.*, 43: 1–9.

NTC (2008). Norme Tecniche per le Costruzioni. DM 14 gennaio 2008. *Gazzetta Ufficiale della Repubblica Italiana*, 29. In Italian.

Pace B., Peruzza L., Lavecchia G., and Boncio P. (2006). Layered seismogenic source model and probabilistic seismic hazard analyses in Central Italy, *Bull. Seismol. Soc. Am.* 96: 107–132.

Pagani, M., Monelli, D., Weatherill G.A., Danciu L., Crowley H., Silva V., Henshaw P., Butler L., Nastasi M., Panzeri L., Simionato M., and Viganò D. (2014a). OpenQuake engine: an pen hazard (and risk) software for the global earthquake model, *Seismol. Res. Lett.*, 85: 692-702.

Pagani, M., Monelli, D., Weatherill, G.A., and Garcia, J. (2014b).The OpenQuake-engine book: hazard, *Technical Report 2014-08*, Global Earthquake Model (GEM).

Patanè D., Ferrucci F., and Gresta S. (1994). Spectral features of microearthquakes in volcanic areas: Attenuation in the crust and amplitude response of the site at Mt. Etna (Italy), *Bull. Seismol. Soc. Am.*, 84: 1842–1860.

Patanè D., Ferrucci F., Giampiccolo E., and Scaramuzzino L. (1997). Source scaling of microearthquakes at Mt. Etna volcano and in the Calabrian Arc (southern Italy), *Geoph. Res. Lett.*, 24: 1879–1882.

Pepe F., Sulli A., Bertotti G., and Cella F. (2010). Architecture and Neogene to recent evolution of the western Calabrian continental margin: an upper plate perspective to the Ionian subduction system, central Mediterranean, *Tectonics*, 29*:* TC3007.

Petersen,M. D., and other 16 authors (2014). Documentation for the 2014 update of the United States national seismic hazard maps, U.S.G.S. Open-File Report 2014–1091.

Rebez A., Sandron D., Santulin M., Peruzza L., Tamaro A., Eusebio M., Mucciarelli M., and Slejko D. (2014). Input accelerograms and expected accelerations for some dam sites in Southern Italy, *Proc. of the 33rd Conference of the gruppo nazionale di geofisica della terra solida (GNGTS)*, Bologna, Italy, November 25-27.

Reilinger R., and other 24 authors (2006). GPS constraints on continental deformation in the Africa-Arabia-Eurasia continental collision zone and implications for the dynamics of plate interactions, *J. Geophys. Res.*, 111: B05411.

Sabetta F., and Pugliese A. (1987). Attenuation of peak horizontal acceleration and velocity from Italian strong-motion records, *Bull. Seismol. Soc. Am.*, 77: 1491-1513.

Sabetta F., and Pugliese A. (1996). Estimation of response spectra and simulation of nonstationary earthquake ground motions, *Bull. Seismol. Soc. Am.*, 86: 337–352.

Sabetta F., Lucantoni A., Bungum H., and Bommer J.J. (2005). Sensitivity of PSHA results to ground motion prediction relations and logic-tree weights, *Soil Dynam. Earthq. Eng.* 25: 317-329.

Scasserra G., Stewart J.P., Bazzurro P., Lanzo G., and Mollaioli F. (2009). A comparison of NGA ground-motion prediction equations to Italian data, *Bull. Seismol. Soc. Am.*, 99: 2961–2978.

Scherbaum F., Schmedes J., and Cotton F. (2004). On the conversion of source-to-site distance measures for extended earthquake source models, *Bull. Seismol. Soc. Am.*, 94: 1053–1069.

Schwartz D.P., and Coppersmith K.J. (1984). Fault behaviour and characteristic earthquakes: examples from Wasatch and San Andreas faults, *J. Geophys. Res.*, 89: 5681–5698.

Selvaggi G., and Chiarabba C., (1995). Seismicity and P-wave velocity image of the southern Tyrrhenian subduction zone, *Geophys. J. Int.*, 121: 818–826.

Serpelloni E., Vannucci G., Pondrelli S., Argnani A., Casula G., Anzidei M., Baldi P., and Gasperini P. (2007). Kinematics of the Western Africa–Eurasia plate boundary from focal mechanisms and GPS data, *Geophys. J. Int.*, 169: 1180–1200.

Silva V., Crowley H., Pagani M., Monelli D., and Pinho R. (2014). Development of the OpenQuake engine, the global earthquake model's open-source software for seismic risk assessment, *Nat. Hazards*, 72: 1409-1427.

Slejko D., Caporali A., Stirling M., and Barba S. (2010). Occurrence probability of moderate to large earthquakes in Italy based on new geophysical methods, *Journal of Seismology*, 14: 27–51.

Spina V., Galli P., Tondi E., Critelli S., and Cello G. (2006). Kinematics and structural properties of active fault segments in the Sila Massif, northern Calabria, Italy, *Geophys. Res. Abstr.*, 8: 03547.

Spina V., Galli P., Tondi E., Critelli S., and Cello G. (2007). Kinematics and structural properties of active fault segments in the Sila Massif (Northern Calabria, Italy), *Boll. Soc. Geol. It.*, 126: 427-438.

Spina V., Tondi E., and Mazzoli S. (2011). Complex basin development in a wrench-dominated back-arc area: Tectonic evolution of the Crati Basin, Calabria, Italy, *J. Geodyn.*, 51: 90–109.

Spina V., Tondi E., Galli P., and Cello G. (2004). Morphostructural analysis of an active fault in the Sila massif (Calabria, southern Italy): implication for the seismic hazard and recent evolution of the area, *Proc. of the 23rd Convegno Nazionale gruppo nazionale di geofisica della terra solida*, Rome, Italy, 14-16 December.

Spina V., Tondi E., Galli P., and Mazzoli S. (2009). Fault propagation in a seismic gap area (northern Calabria, Italy):implication for seismic hazard, *Tectonophysics*, 476: 357–369.

Stewart J.P., Douglas J., Javanbarg M., Bozorgnia Y., Abrahamson N.A., Boore D.M., Campbell K.W., Delavaud E., Erdik M., and Stafford P.J. (2015). Selection of Ground Motion Prediction Equations for the Global Earthquake Model, *Earthq. Spectra*, 31: 19-45.

Strasser F.O., Arango M.C., and Bommer J.J. (2010). scaling of the source dimensions of interface and intraslab subduction-zone earthquakes with Moment Magnitude, *Seismol. Res. Lett.*, 81: 941-950.

Stucchi M., Meletti C., Montaldo V., Crowley H., Calvi G.M., and Boschi E. (2011). Seismic hazard assessment (2003–2009) for the Italian building code, *Bull. Seismol. Soc. Am.*, 101: 1885–1911.

Stucchi M., Rovida A., Gomez Capera A.A., Alexandre P., Camelbeeck T., Demircioglu M.B., Gasperini P., Kouskouna V., Musson R.M.W., Radulian M., Sesetyan K., Vilanova S., Baumont D., Bungum H., Fäh D., Lenhardt W., Makropoulos K., Martinez Solares J.M., Scotti O., Živčić M., Albini P., Battlo J., Papaioannou C., Tatevossian R., Locati M., Meletti C., Viganò D., and Giardini D. (2012). The SHARE European earthquake catalogue (SHEEC), *J. Seismol.*, 17: 523-544.

Tansi C., Muto F., Critelli S., and Iovine G. (2007). Neogene-Quaternary strike-slip tectonics in the central Calabrian Arc (southern Italy), *J. Geodyn.*, 43: 393–414.

Tansi C., Tallarico A., Iovine G., Folino Gallo, M., and Falcone, G. (2005). Interpretation of radon anomalies in seismotectonic and tectonic-gravitational settings: the south-eastern Crati graben (Northern Calabria, Italy), *Tectonophysics*, 396: 181–193.

Thomas P., Wong I., and Abrahamson N. A. (2010). Verification of probabilistic seismic hazard analysis computer programs, *PEER report 2010/106*, Pacific Earthquake Engineering Research Center, University of California, Berkeley.

Van Dijk J.P., Bello M., Brancaleoni G.P., Cantarella G., Costa V., Frixa A., Golfetto F., Merlini S., Riva M., Torricelli S., Toscano C., and Zerilli A. (2000). A regional structural model for the northern sector of the Calabrian Arc (southern Italy), *Tectonophysics*, 324: 267–320.

Ward S.N., (2007). Methods for evaluating earthquake potential and likelihood in and around California, *Seismol. Res. Lett.*, 78: 121-133.

Wells D.L., and Coppersmith K.J. (1994). New empirical relationships among magnitude, rupture length, rupture width, rupture area, and surface displacement, *Bull. Seismol. Soc. Am.* 84: 974–1002.

Woessner J., Danciu L., Giardini D., Crowley H., Cotton F., Grünthal G., Valensise G., Arvidsson R., Basili R., Demircioglu M. B., Hiemer S., Meletti C., Musson R. W., Rovida A. N., Sesetyan K., Stucchi M., the SHARE Consortium (2015). The 2013 European Seismic Hazard Model: key components and results, *Bull. Earthq. Eng*, in press. DOI 10.1007/s10518-015-9795-1

Woessner J., Giardini D., and Danciu L. (2012). SHARE deliverable D5.5 – Final seismic hazard assessment including de-aggregation, available at: http://www.share-eu.org/sites/default/files/D5.5_SHARE.pdf (last accessed October, 2015).

Woessner J., Giardini D., and the SHARE consortium (2012). Seismic Hazard Estimates for the Euro-Mediterranean Region: A community-based probabilistic seismic hazard assessment, *Proc. of the 15th World Conference of Earthquake Engineering*, Lisbon, Portugal, 24-28 September.

Zhao J.X., Zhang J., Asano A., Ohno Y., Oouchi T., Takahashi T., Ogawa H., Irikura K., Thio H.K., Somerville P.G., Fukushima Yo., and Fukushima Ya. (2006). Attenuation relations of strong ground motion in Japan using site classification based on predominant period, *Bull. Seismol. Soc. Am.*, 96: 898-913.